THE UNIVERSITY *of* EDINBURGH

Resolved Stellar Populations of NGC 6822 with JWST

Conor Nally

Doctor of Philosophy
The University of Edinburgh
15th September 2025

Abstract

Infrared observations of stellar populations trace the evolutionary cycle of dust and baryonic matter in their host galaxy. Understanding this cycle is key to building a picture of galaxy formation and evolution, star formation, and chemical enrichment in the Universe. Local Group galaxies offer a unique opportunity to characterise the chemical evolution under conditions analogous to those in higher redshift systems. The previous generation of great infrared observatories, *Herschel* and *Spitzer*, were capable of mapping galaxies in our immediate neighbourhood to ~1 Mpc. This space includes galaxies such as the Large and Small Magellanic Clouds (50 and 60 kpc respectively), which, with their low metallicities (0.5 and 0.2 $Z_{\odot}$) and active star-formation, serve as ideal test-beds for theories on how dust forms, evolves, and is destroyed on both small and large scales. The launch of *JWST* vastly expands this observation window to an order of magnitude greater distances, and encompasses a vast array of parameter spaces to search where, for the first time, we can conduct high-resolution imaging and spectroscopy. This provides the depth and spatial scales previously only obtainable in our Galaxy.

With unprecedented depth and high-resolution data provided by *JWST*, come new challenges in data processing. The second chapter of this thesis outlines the development of STARBUGII, a PSF photometric suite tuned to detect and recover photometry from deeply embedded objects in complex and crowded fields. This open source software has been applied to a number of local galaxies, enabling the first resolved stellar population studies from *JWST* to be conducted.

One such galaxy, and the focus of the remainder of this thesis, is NGC 6822. This is a nearby (490 kpc) irregular dwarf. Its tidal isolation, low metallicity (Z~0.3 $Z_{\odot}$), and ongoing star formation make it similar to galaxies during the epoch of peak star formation. NGC 6822 underwent a rapid increase in star formation approximately 3 Gyrs ago, and it remains unclear what triggered the

event. In chapter three, using STARBUGII, I produce a deep stellar catalogue of the central bar of NGC 6822, the photometry reaching ~7 magnitudes deeper than previous JHK_s surveys of the area. This deep NIRCam catalogue reveals stellar populations ~3 magnitudes below the Red Clump for the first time. With MIRI, I detect sources ~2 magnitudes below the Tip of the Red Giant Branch. This near- to mid-infrared combined catalogue contains ~$900,000$ point sources, allowing a comprehensive survey of the central bar, revealing features from various populations that have never been seen in NGC 6822 in the infrared.

Asymptotic Giant Branch (AGB) stars evolve from low- to intermediate mass (0.8-8 $M_\odot$) progenitors in their final stages of nuclear burning. Due to their high infrared luminosity, stellar winds, and mass loss, they are some of the most influential stars in their systems. Dust-driven wind in the final stages of an AGB stars evolution will, at its peak, inject $10^{-4}M_\odot yr^{-1}$ produced gas and dust into the interstellar medium (ISM) to form the natal material for the next generation of star formation. However, their dust production mechanisms and how this affects the subsequent rounds of evolution are not well understood, especially in low-metallicity environments. The large number of AGB stars in NGC 6822 offers an excellent vantage point from which to study these processes.

In the fourth chapter, I produce an H-R diagram of the NGC 6822 bar, derived from blackbody modelling of the photospheres of stars to a photometric depth of the Red Clump. I identify the AGB stars within my *JWST* NGC 6822 catalogue through a series of CMD colour-cuts, measure dust production through SEDs fitting with the GRAMS grid of AGB models and determine their chemical subtypes. The models enable the robust separation of oxygen- and carbon-rich AGB types, which is crucial for disentangling the effects of age, mass, and metallicity within the population. I determine the quantity of dust produced in the central stellar bar of NGC 6822 to be 5.6×10^{-7} $M_\odot yr^{-1}$, with ~60% of this being produced by oxygen-rich AGB stars. This contradicts the recent paradigm that carbon stars are the primary source of dust production in metal-poor galaxies. The separated AGB species allows me to analyse the carbon-star luminosity functions, as well as map the spatial distribution of metallicity across the field and develop observational proxies for measuring dust production rates.

Lay Summary

When a star like our Sun gets to the end of its life, it will expand so large as to engulf the Earth. This red *giant* becomes a thousand times brighter and very unstable. We call it an "*Asymptotic Giant Branch*" (AGB) star. These dying stars are important because they produce a lot of dust, and as the saying goes, "*everything is made of star dust*". AGB stars, therefore, play a crucial role in the production of natal materials from which all planets and stars are formed.

With the new space telescope, *JWST*, we can observe these AGB stars in more detail than ever before. By studying them in a diverse range of galaxies, we can begin to build a picture of the origin and continued recycling of dust in the Universe. One such galaxy is NGC 6822. Although it is one of our closest galactic neighbours (~1.5 million light years away), it has a similar composition to galaxies in the more distant Universe.

In this thesis, I develop the tools to detect nearly a million stars in infrared *JWST* images of the central region of NGC 6822. I identify a wide range of "species", locating a small subset that are the AGB stars. By matching the shapes of their spectra to a library of theoretical models, I measure properties such as temperature, luminosity, chemical composition and the rate at which they produce dust. I demonstrate that the majority of the dust originates from a small number of particularly extreme individuals, and estimate the total quantity produced throughout the entire galaxy. By isolating the primary chemistry of the stars, I find that NGC 6822 exhibits a far higher proportion of oxygen-rich dust than expected. Finally, I develop a system of measuring AGB dust production rate from a set of observable properties, allowing for this research to be conducted at a greater scale in the future.

Declaration

I declare that this thesis was composed by myself, that the work contained herein is my own except where explicitly stated otherwise in the text, and that this work has not been submitted for any other degree or professional qualification except as specified.

Parts of this work have been published in (Nally, 2023).

Parts of this work have been published in (Nally et al., 2024).

YSO SED fitting in Section 4.3.5 performed by Laura Lenkić.

(*Conor Nally, 15th September 2025*)

Supporting Publications

- **JWST/NIRCam detections of dusty subsolar-mass young stellar objects in the Small Magellanic Cloud**
  Jones, **Nally**, Habel, Lenkić, Fahrion et al. 2023, Nature Astronomy 7, 694

- **JWST Mid-infrared Spectroscopy Resolves Gas, Dust, and Ice in Young Stellar Objects in the Large Magellanic Cloud**
  Nayak, Hirschauer, Kavanagh, Meixner, Chu **et al.** 2024, ApJ 963, 145

- **JWST MIRI and NIRCam unveil previously unseen infrared stellar populations in NGC 6822**
  Nally, Jones, Lenkić, Habel, Hirschauer et al. 2024, MNRAS 531, 183

- **A JWST/MIRI and NIRCam Analysis of the Young Stellar Object Population in the Spitzer I region of NGC 6822**
  Lenkić, **Nally**, Jones, Boyer, Kavanagh et al. 2024, ApJ 967, 110

- **Imaging of I Zw 18 by JWST: I. Strategy and First Results of Dusty Stellar Populations**
  Hirschauer, Crouzet, Habel, Lenkić, **Nally** et al. 2024, AJ 168, 183

- **Young Stellar Objects in NGC 346: A JWST NIRCam/MIRI Imaging Survey**
  Habel, **Nally**, Lenkić, Meixner, De Marchi et al. 2024, AAS 971, 146

- **Imaging of I Zw 18 by JWST: II. Spatially resolved star formation history**
  Bortolini, Östlin, Habel, Hirschauer, Jones, **et al.** 2024, A&A 689, 146

- **Embedded Young Stellar Objects near H72.97-69.39, a forming Super Star Cluster in N79**
  Nayak, **Nally**, Hirschauer, Jones, Jaspers et al. 2024, AAS 975, 262

- **Protoplanetary Disks around Sun-like Stars Appear to Live Longer When the Metallicity is Low**
  De Marchi, Giardino, Biazzo, Panagia, Sabbi, **et al.** 2024, ApJ 977, 214

- **Euclid. I. Overview of the Euclid mission**
  Euclid Collaboration **et al.** 2025, A&A 697, A1

- **Euclid: Early Release Observations – Programme overview and pipeline for compact- and diffuse-emission photometry**
  Cuillandre, Bertin, Bolzonella, Bouy, Gwyn **et al.** 2025, A&A 697, A6

- **Euclid: Early Release Observations – Deep anatomy of nearby galaxies**
  Hunt, Annibali, Cuillandre, Ferguson, Jablonka **et al.** 2025, A&A 697, 9H

- **Investigating the metallicity dependence of the mass-loss rate relation of red supergiants**
  Antoniadis, Zapartas, Bonanos, Maravelias, **et al.** 2025, A&A 702, 178

- **A Mid-infrared Spectroscopic Study of Young Stellar Objects in the SMC Region NGC 346: JWST Detects Dust, Accretion, Ices, and Outflows**
  Habel, Nayak, Kavanagh, Jones, **et al.** 2025, ApJ 995, 22

Acknowledgements

Producing this thesis was an undertaking as rewarding as it was challenging, and one that would not have been possible without the continued support from everyone around me.

First and foremost, I would like to thank my supervisor, Libby. Thank you for bringing me along on this wonderful journey. For riding the highs with me and picking me up in the lows. Who seems to know everything, but for whom no question is too daft. I will not miss your red pen though.

Annette, who has patiently guided me in the right direction for the past ten years and always cared for my well-being, I am enormously grateful.

I would like to thank everyone on the WINGS team for their unwavering support as we explored the most amazing areas of space together. A special thank you to Margaret for welcoming me so warmly into her group and for giving me free rein on cutting-edge data. Thank you, Alec, for too many things to name, without whom I would not have reached the finish line. To Laura and Nolan for their data processing solidarity and for giving me the best time ever in the States. Finally, thank you Isha and Patrick, for all your invaluable input over the past years.

To all those in the Higgs Centre, thank you for creating an atmosphere of relentless positivity over the last four years. For lunchtime runs, after-school climbing, word games, coffee in the sun, quietly checking in, and genuine enthusiasm in seeing me approach completion. I especially want to thank Jess for keeping me positive with our hours of chatting, Léa for walking me through every complicated system the uni has, and Linus, Ottavia and Giulia for making me feel welcome.

Thank you to Mum for feeling proud, Dad for being my hero, and Joe for a lifetime of competition - you may be taller, but now I have written a book. A huge thank you to Amanda for "booping the coffee machine" and being the driving force behind all our adventures.

Without the miles of footpaths around Blackford Hill, I probably would have lost my mind, and the draw of the Hebridean Sea kept me focused at the end. Finally, I would like to extend a heartfelt thank you to the countless people in my life who offered warm words of support when I really needed it.

Contents

List of Figures

List of Tables

1 Introduction

I is sometimes hearing faraway music
coming from the stars in the sky.

— The BFG

When a star dies, the material it has spent its life enriching through internal nucleosynthesis is ejected back out into its local environment. The gas and dust renew the interstellar medium (ISM), forming the natal material for the subsequent rounds of star formation. The next generation of stars are born from increasingly heavier elements, leading to continued enrichment of their host galaxy.

ISM replenishment occurs through the dusty winds of Asymptotic Giant Branch (AGB) stars or Supernovae, and is destroyed in the cloud collapse of a Young Stellar Object (YSO). Understanding this cycle of dust formation and destruction requires an intricate analysis of each key stage. Infrared observations of nearby galaxies provide a diverse range of environments in which we can study individual stars, as well as the entire populations to which they belong. By disentangling the stellar populations of these galaxies and constraining the effect of metallicity on their dust production and its chemistry, we can build a picture of the dust life-cycle across the Universe.

With the recent arrival of *JWST*, the observable volume of populations has drastically increased. This work focuses on disentangling the infrared stellar populations of the Local Group dwarf galaxy NGC 6822 with this new observatory and quantifying the dust production rates and chemical properties of the subset of AGB stars within this population.

1.1 Low- to Intermediate-mass Stars

1.1.1 Pre-AGB Stellar Evolution

Stars within an initial mass range ~0.8 – 8 $M_\odot$ will, towards the end of their nuclear-burning life, move onto the AGB. This Section gives an overview of the evolution of a sun-like star (Z~0.02[1]) from its entry onto the "*Main Sequence*" (MS) to the base of the AGB. When appropriate, divergence from this evolutionary path due to differing initial stellar properties will be commented on.

A low-to-intermediate-mass star enters the MS at the onset of hydrogen nuclear burning in its core. The initial mass of the star at this start-point (*zero-age main sequence*; M_{ZAMS}) is key in determining the evolutionary sequence it takes. The hydrogen-burning, through the p-p chain for low-mass stars ($M_{ZAMS} \lesssim 1.8\ M_\odot$) and the CNO-cycle for intermediate-mass stars ($M_{ZAMS} \gtrsim 1.8\ M_\odot$), accumulates inert helium in the core. This long-lived, hydrostatically stable stage of evolution comprises the majority of the star's lifetime, approximately 10 Gyrs of a total 12 Gyrs lifespan for a 1 $M_\odot$ star and 0.3 Gyrs of 0.4 Gyr for an 8 $M_\odot$ star (Iben, 1967; Karakas & Lattanzio, 2014). Once the finite supply of hydrogen in the core is finally exhausted, the star moves off the MS. Figure 1.1 shows a sketch of the evolution of a 1 $M_\odot$ sun-like star on a Hertzsprung-Russell diagram (H-R) from this point on.

After hydrogen exhaustion, the core contracts and heats up, triggering hydrogen-burning in a surrounding shell. The energy output from shell burning causes the outer envelope to expand significantly. As the star crosses the Hertzsprung Gap, the envelope becomes convective as the material cools and becomes more opaque. Once convection reaches deep into the centre, the star begins its stable evolution on the "*Red Giant Branch*" (RGB) (Iben, 1967; Salaris & Cassisi, 2005). As the convection extends deeper into the star, it will contact the hydrogen-burning shell, an event known as the "*first dredge-up*". Since this region of the star has not previously been affected by surface mixing mechanisms, the first dredge-up transports processed material (primarily ^{14}N and ^{13}C) to the surface, resulting in a measurable enrichment (Karakas, 2017a).

[1]The approximate chemical composition by mass of the sun is ~ 70% H, ~ 28% ^{4}He and therefore, ~ 2% is made up of other materials. Metallicity (Z) is given by the proportion of the total mass contributed by all other materials heavier than helium.

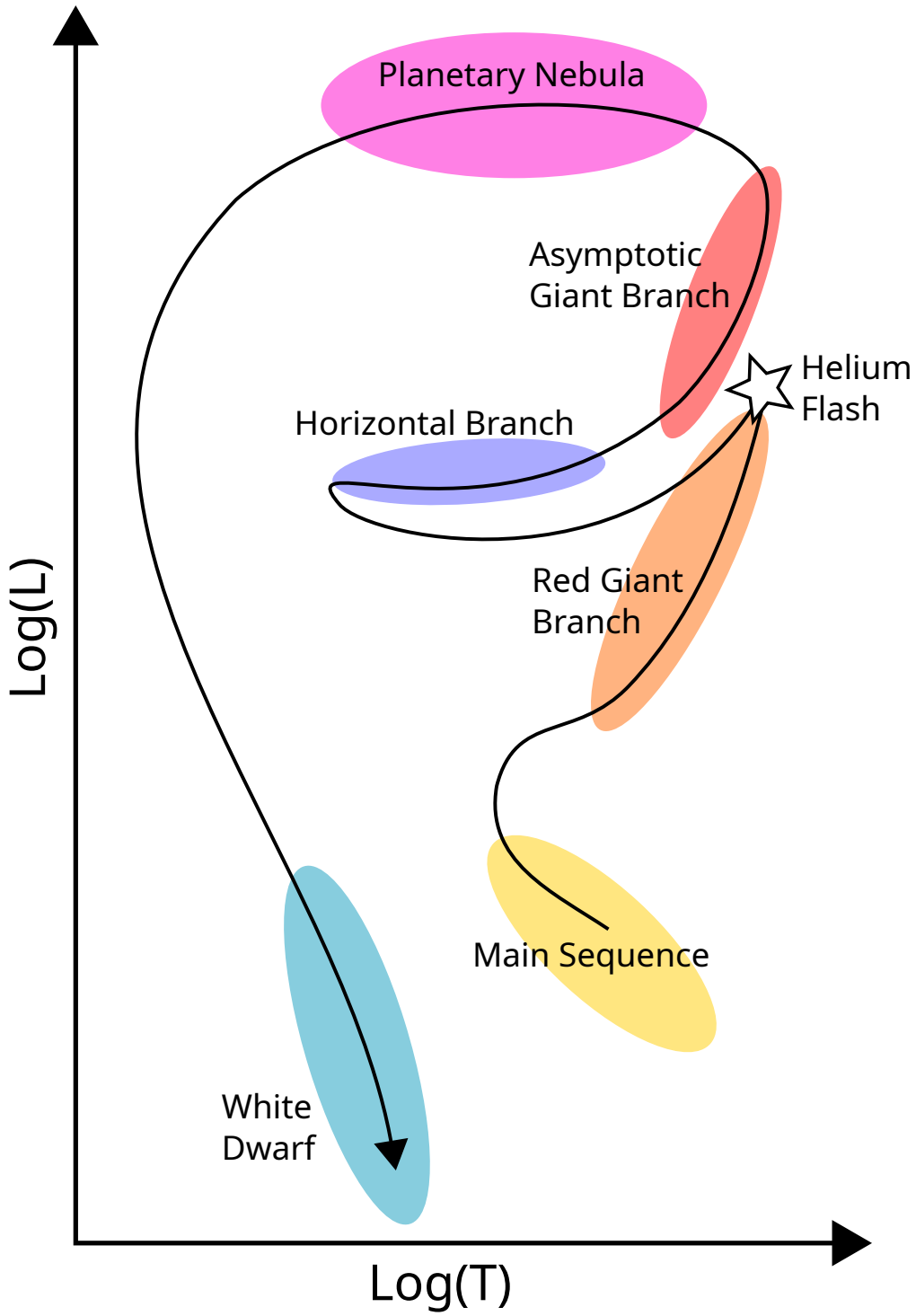

Figure 1.1 H-R diagram sketch for a solar mass star. Key evolutionary stages are labelled, starting from the Main Sequence, and ending in a White Dwarf.

The star's evolution continues up the RGB. For low-mass stars (<1.8 $M_\odot$), the He core contracts until it is supported by electron degeneracy pressure. However, the core mass and temperature continue to grow with the accumulation of "ash" from hydrogen shell burning. Core temperature reaches ~10^8 K, igniting the degenerate He and triggering He to C nuclear-burning via the 3α-process. In a thermonuclear runaway, the reaction emits large amounts of energy $\gtrsim 10^{10} L_\odot$ in a very short period (a matter of days; Härm & Schwarzschild, 1961; Mocák et al., 2009), in an event known as a "*helium-flash*". The increased energy output works to expand the core, reducing pressure on the helium-burning shell, and as a result, the observable luminosity decreases. The star moves off the RGB and enters the next stage of stable core helium-burning (Lattanzio & Wood, 2004). The new position on Figure 1.1 is contingent on the metallicity and envelope mass of the star (Herwig, 2005); low-mass metal-poor stars move to the *Horizontal Branch* (HB), while the remainder are positioned in a cooler point known as the *Red Clump* (RC). Stable core helium-burning will occur here until the eventual exhaustion of available helium. The core is once again rendered inert, supported by electron degeneracy pressure and consisting of carbon and oxygen. The stars' primary energy source moves to a helium shell around the core, and a hydrogen shell around that, once again increasing luminosity and ascending the giant branch in Figure 1.1, to begin the AGB phase (Lattanzio & Wood, 2004).

The helium cores of intermediate-mass stars (>1.8 $M_\odot$) do not become degenerate after leaving the MS. Instead, two competing energy sources develop: a non-degenerate helium-burning core and a hydrogen-burning shell surrounding this. Their evolution on Figure 1.1 is similar, but they appear hotter and may undergo a "*blue-loop*", the extent of which is determined by the interplay between these two energy sources (Kippenhahn et al., 2012). Once helium is depleted, the inert C-O core contracts and heats up. Helium fusion ignites in a shell surrounding the core, with hydrogen shell burning active above it. This dual-shell burning structure marks the onset of the AGB phase as the star reascends the giant branch (Karakas & Lattanzio, 2014).

1.1.2 The AGB phase

The AGB evolutionary phase is characterised by helium-burning in a shell around an electron-degenerate C-O core. Above this lies a hydrogen-burning shell, the products of which accumulate in an intervening helium-rich "intershell" region.

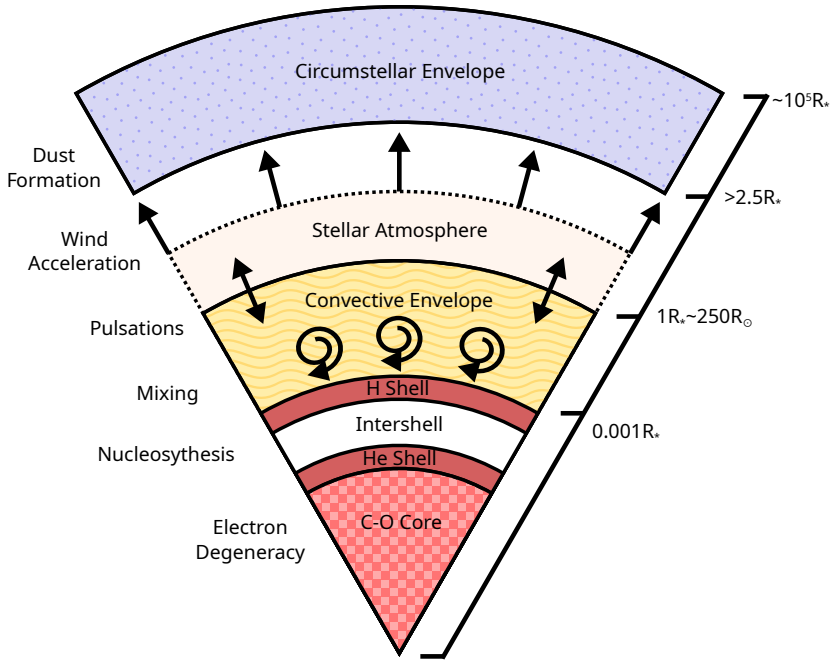

Figure 1.2 The internal structure of a thermally-pulsing AGB star. Figure adapted from Lattanzio & Wood (2004) and Höfner & Olofsson (2018).

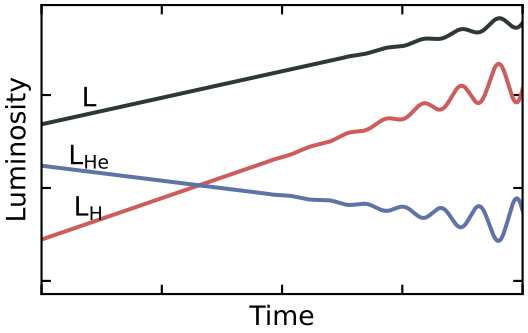

Figure 1.3 A sketch of combined energy output from the interplay between hydrogen- and helium-shell burning in early-AGB stars, plotted against time. This figure has been adapted from Lattanzio & Wood (2004).

Above this double shell structure is a cool convective stellar envelope. Figure 1.2 shows a schematic of the internal structure of an AGB. While sufficient fuel in the helium shell remains, the star maintains this stable configuration, known as the "*Early-AGB*" phase. The "*second dredge-up*" is initiated in stars above a critical mass (~4$M_\odot$ Kippenhahn et al., 2012) as the convective envelope deepens and extends through the hydrogen-shell (Iben & Renzini, 1983).

Figure 1.3 shows a sketch of the early-AGB star surface luminosity and the output energy from the two shells against time. Initially, the helium-burning shell provides the primary source of energy. Over time (10^5–10^6 yr; Lattanzio & Wood, 2004), it depletes its fuel, the intershell region thins, and hydrogen-shell burning becomes increasingly significant. As the helium shell becomes thermally unstable, it begins to undergo periodic oscillations. These helium shell instabilities suppress hydrogen burning during each pulse cycle. The onset of this alternating shell activity marks the star's transition into the "*thermally pulsing AGB*" (TP-AGB) phase (Karakas, 2017a).

1.1.3 Thermally-Pulsing AGB

Thermal pulses arise from the coupled interaction between helium- and hydrogen-burning shells. A buildup of helium-burning fuel in the intershell region eventually triggers a brief but intense helium shell flash, with luminosities reaching up to ~$10^8 L_\odot$ (Habing & Olofsson, 2004). The energy output does not directly reach the surface of the star; instead, it causes substantial expansion of the internal

structures. This energy release drives convection in the intershell region and lifts and cools the surrounding layers (Habing, 1996), temporarily quenching hydrogen shell burning. The pulse-driven convection mixes the nucleosynthesised products in the intershell region. The helium-burning phase is short-lived ($\sim 10^2$ yrs), after which the star settles into a phase of quiescent hydrogen burning - the "*interpulse*" period. During this time, helium ash from the hydrogen shell accumulates, gradually increasing the mass and temperature of the intershell region until the next helium flash occurs, repeating the thermal-pulse cycle on a period of $\sim 10^4$ yrs (Karakas, 2017a).

During a thermal pulse, the convective stellar envelope deepens, mixing the products of nucleosynthesis from the two shells into the envelope. This period of mixing is known as the "*third dredge-up*" (TDU). The dredged-up material typically includes freshly synthesised ^{12}C. Repeated dredge-up events gradually increase the carbon abundance in the envelope, potentially resulting in a "*carbon star*" (Iben, 1975).

Depending on the chemical abundance ratio C/O, AGB stars can be separated into two chemical classes. When the C/O>1, they are classified as carbon-rich (CAGB) and <1 oxygen-rich (OAGB). This is because the free carbon and oxygen are bound together as highly stable CO molecules in the stellar envelope, exhausting the availability of whichever atom is less abundant. As stars typically begin with a greater fraction of oxygen (Delgado Mena et al., 2010), the TDU is therefore a key mechanism linking the nucleosynthesis to the surface composition (Wallerstein & Knapp, 1998).

In higher mass ($M_{ZAMS} \gtrsim 4$ M$_\odot$) AGB stars, the base of the convective envelope is hot enough ($> 5\times10^7$ K; Boothroyd & Sackmann, 1992) to initiate proton-capture reactions. This is called "*Hot Bottom Burning*" (HBB), and acts to convert synthesised ^{12}C to ^{14}N through the CN-cycle. Thus, HBB limits the availability of carbon and prevents these stars from ever developing into carbon stars (Boothroyd et al., 1993; García-Hernández et al., 2013). The mass-dependent interplay between TDU and HBB effects leads to the bimodal distribution of observed AGBs (at a fixed metallicity), where OAGBs are favoured in the lower and higher mass cases, while CAGBs are favoured in the intermediate range ($\sim 1.5 - 3 M_\odot$) (Boothroyd et al., 1995; Marigo & Girardi, 2007; Girardi & Marigo, 2007; Ventura et al., 2012).

Metallicity plays a further crucial role in the distribution of AGB C/O ratios.

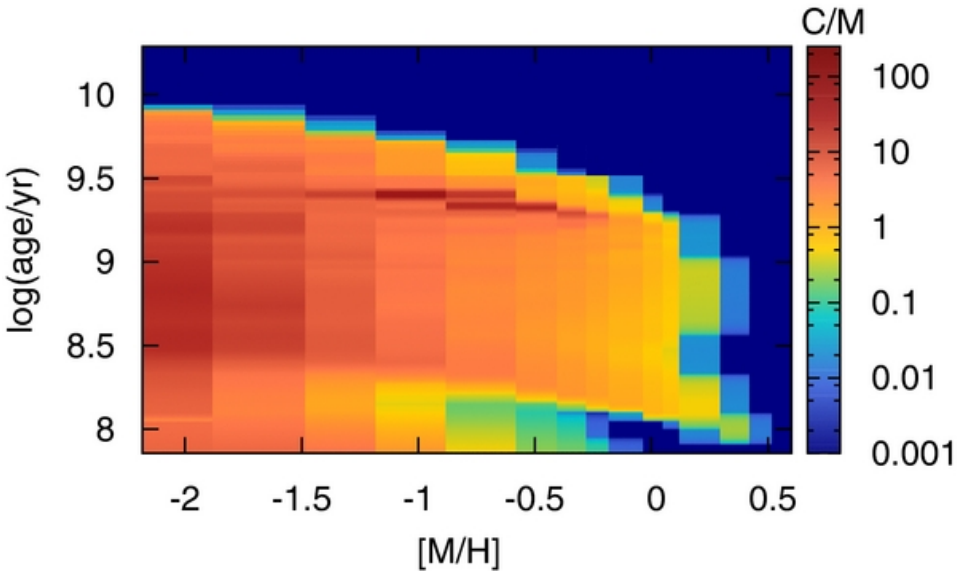

Figure 1.4 Maximum C/O ratio attained by AGB stars at a given metallicity and age. Blue denotes C/O<1, and red shows increasing C/O>1. Figure taken from Boyer et al. (2013) based on stellar isochrone models from Marigo et al. (2013).

The nucleosynthesis of carbon via the 3α-process in the AGB does not require existing metals to occur and therefore, is not hindered in low-metallicity environments (Marigo et al., 1999). Furthermore, in a low metallicity star, the number of TDU events required to surpass C/O is lower, simply because there is less free oxygen to be bound into CO (McDonald et al., 2012). Whereas the C, N, and O ingredients for the CNO-cycle are more scarce in low metallicity stars, so the efficiency of HBB is vastly reduced (Karakas & Lattanzio, 2014). These effects combine such that CAGB formation is efficient in low metallicity environments. This has been seen across galaxies in the Magellanic Clouds (Cioni & Habing, 2003; Cioni et al., 2006a), with Figure 1.4 from Boyer et al. (2013) showing the highest attained C/O within AGB stars across a range of metallicities. The figure demonstrates that at low metallicity, the mass range within which a CAGB can form becomes much larger.

1.1.4 Variability and Mass-loss in TP-AGB Stars

Brief and intense thermal pulses caused by the sudden ignition of helium characterise the TP-AGB evolutionary phase by inducing strong structural instabilities. While these thermal pulses cause cyclical changes in the star's interior, the pulsations of the envelope (observed as periodic brightness variations)

are primarily driven by the κ-mechanism[2] acting in partial ionisation zones of hydrogen and helium (Ahmad et al., 2023). These pulsations propagate through the entire convective envelope and are amplified in the extended atmosphere, producing large-amplitude radial oscillations on the timescale ~100 – 1000 days (Lattanzio & Wood, 2004).

In the 17^{th} century, Dutch astronomer Phocylides Holwarda documented the star Omicron Ceti, which exhibited remarkable periodic brightening and fading - initially interpreted as disappearance and reappearance - earning it the name "*Stellar Mira*," meaning miraculous. We now understand that this behaviour is due to the long-period variability characteristic of stars in the TP-AGB phase (Habing & Olofsson, 2004). Miras fall under the bracket of stars known as "*Long Period Variables*" that exhibit a well-constrained period-luminosity (Feast et al., 1989; Wood et al., 1999; Whitelock et al., 2008), making them key tools for determining distances to extragalactic objects.

The combination of high luminosities (~10^3–10^4 $L_\odot$), low effective temperatures (~2000-4000 K), and the substantial expansion of the convective envelope causes TP-AGB stars to reach radii on the order of ~10^2 $R_\odot$. This results in a stellar atmosphere that is only weakly gravitationally bound; surface gravities can be 4–5 orders of magnitude lower than those of main-sequence stars like the Sun. As a result, TP-AGB stars experience substantial mass loss. However, radiation pressure on molecular gas alone is insufficient to drive a wind, as its opacity is too low (Liljegren et al., 2017). Shock waves caused by pulses dynamically lift the molecular gas free of the photosphere and into the atmosphere. The gas cools through expansion as it moves further from the star, allowing it to cool and condense into dust. With spectral energy distributions peaking in the near-IR, the photons emitted by TP-AGB stars are efficiently absorbed and scattered by the condensed dust. This interaction exerts an intense radiation pressure on the dust grains, imparting momentum to them (Höfner & Dorfi, 1997). Although only making up a small percentage of the atmosphere (~1%), dust grains then transfer momentum to the surrounding gas through collisions, thus dragging the material from the star, this is known as a "*dust-driven wind*" (Bowen & Willson, 1991; Höfner & Dorfi, 1997). The continued action of radiation pressure accelerates the material outward, forming an outflow wind that reaches a velocity of approximately 10 kms^{-1} (Höfner & Olofsson, 2018). Over time, new layers are

[2]The heating of partially-ionised regions causes an increase in opacity, thus "storing" incident energy allowing for a delayed thermal response, leading to structural instabilities.

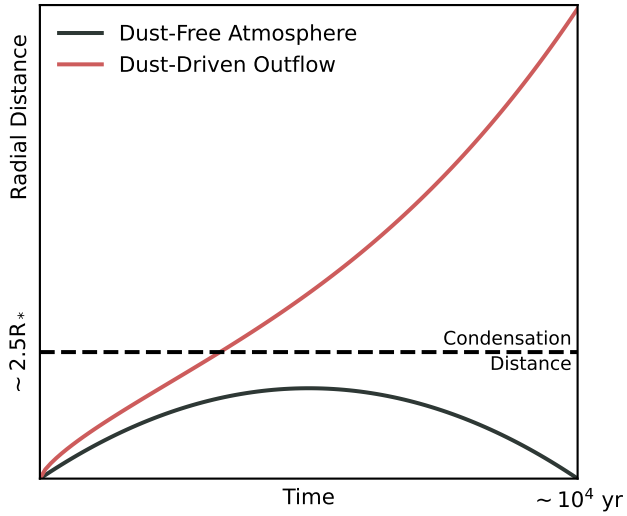

Figure 1.5 An illustration of pulsation enhanced dust-drive outflow. The black line represents the trajectory of a mass layer in a dust-free atmosphere, subject to expansion following a thermal pulse. The red line indicates an outflow that has been lifted past the dust condensation distance, which is accelerated by the wind. Figure adapted from Höfner & Olofsson (2018).

added, and the buildup of molecular gas and dust forms a dense circumstellar shell. Figure 1.5 illustrates the trajectories of material lifted by pulsations past the condensation radius and being accelerated by radiation pressure.

As TP-AGB stars evolve, their decreasing temperature leads to more efficient dust formation, and their increased radiation pressure enhances effective mass loss, setting the stage for the onset of the "*superwind*" (Vassiliadis & Wood, 1993; Höfner & Dorfi, 1997). Mass loss rates peak at 10^{-4} $M_{\odot}yr^{-1}$ (van Loon et al., 1999, 2005), leading to the deep enshrouding of the TP-AGB in its circumstellar shell, and self absorption of the photospheric light (Kraemer et al., 2002). Over the short-lived superwind phase, lasting only $10^2 - 10^3$ years (Höfner & Olofsson, 2018), the accumulation of mass loss can expel 50–70% of the star's initial mass (Weidemann, 2000). In this way, the intensity of the mass loss is so catastrophic that it dictates the duration of the TP-AGB phase itself, rather than the availability of nuclear burning fuel.

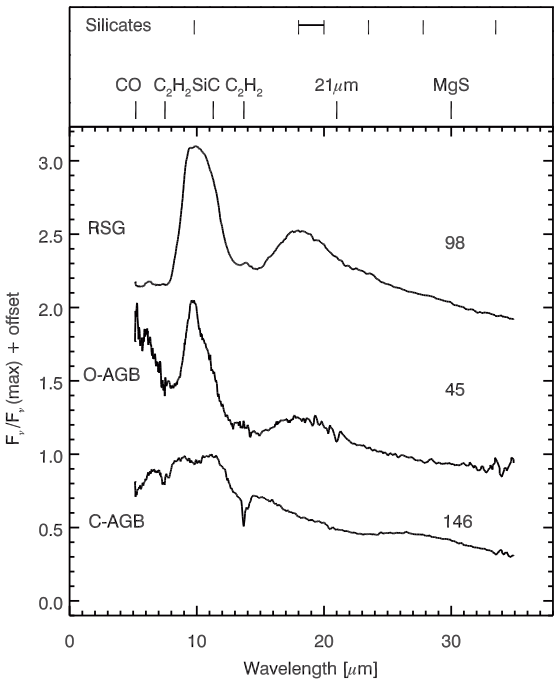

Figure 1.6 Example spectra of CAGB, OAGB and RSG with relevant dust and molecular features. Figure taken from Jones et al. (2017a).

1.1.5 AGB Dust Production

Dust formation in the atmospheres of AGB stars is essential for driving stellar winds. Pulsations lift molecular gas from the stellar surface into the atmosphere, where it expands and cools as it moves outward. If the gas reaches a critical distance (typically around ~2.5 R_*), the temperature falls below the condensation threshold (~1500 K), allowing dust grains to form and survive. Closer to the star, dust cannot condense stably, as radiative heating would cause newly formed grains to evaporate (Bladh & Höfner, 2012; Höfner & Olofsson, 2018). Radiation pressure on dust grains drives the stellar wind, propelling circumstellar material out to parsec-scale distances (Olofsson, 1996; Olofsson et al., 2010). The composition of the wind is governed by both the star's surface chemistry and the available elemental abundances. Figure 1.6 shows example spectra of two AGBs and a *Red Supergiant* star (RSG), showing how they differ based on chemical abundances. Relevant molecular and dust features are labelled.

In CAGBs, where surface C/O>1, the stellar atmosphere becomes abundant in carbon-rich molecules such as C_2 and CN. This carbon excess promotes the formation of several dust species, most notably amorphous carbon (amC), silicon carbide (SiC), and magnesium sulfide (MgS). Among these, amC is the

most abundant and optically thick, providing efficient momentum transfer from stellar radiation and shielding incident radiation on the shell, which encourages continued grain growth and wind acceleration. SiC produces a broad emission feature at 11.3 μm. It typically condenses early in the dust formation sequence, acting as a seed for further grain condensation (Zijlstra et al., 2006; van Loon et al., 2008; Speck et al., 2009). In the cooler, outer regions of the circumstellar envelope, MgS may form and is associated with a broad but weak 30 μm feature. However, the presence of MgS is strongly metallicity-dependent, as neither component is synthesised in significant quantities by the AGB star itself. Consequently, MgS becomes increasingly scarce in metal-poor environments (Zijlstra et al., 2006).

In OAGBs, the abundant oxygen enables the formation of silicates and metal oxides. Amorphous silicates are the primary contributors to the mid-infrared excess seen in OAGBs, characterised by broad emission features near 9.7μm and 18μm. In more evolved OAGBs with high mass loss rates, crystalline silicates may also be present, typically exhibiting narrower features at longer wavelengths (e.g., 23, 33, and 69 μm Waters et al., 1996; Molster et al., 2002). Metal oxides, such as alumina (Al_2O_3), typically contribute less to the total dust mass than silicates, though they play a crucial role in early nucleation, providing seed particles for later silicate condensation (Jones et al., 2014). Since the heavier elements required for forming these species (such as Si and Al) are not produced in the AGB star itself, the efficiency of oxygen-rich dust formation is strongly dependent on the star's initial metallicity (Sloan et al., 2008).

1.1.6 Post-AGB evolution

As the TP-AGB star expels the majority of its envelope through intense mass loss, the pressure supporting nuclear fusion diminishes. This leaves behind a bare degenerate C–O core surrounded by a thin, residual envelope. As the remaining material disperses in the wind, the star contracts and heats, causing its effective temperature to rise. Ultraviolet photons emitted by the hot core illuminate and ionise the circumstellar shell, giving rise to a "*planetary nebula*" (see Figure 1.7). Eventually, nucleosynthesis ceases entirely, and the remnant core cools into a "*white dwarf*" (Paczyński, 1971). The planetary nebula then fades and dissipates into the ISM, forming the natal material for the next round of star formation.

Figure 1.7 The remnant of an AGB star, planetary nebula NGC 3132. Image credit: NASA, ESA, CSA, STScI, and the Webb ERO Production Team.

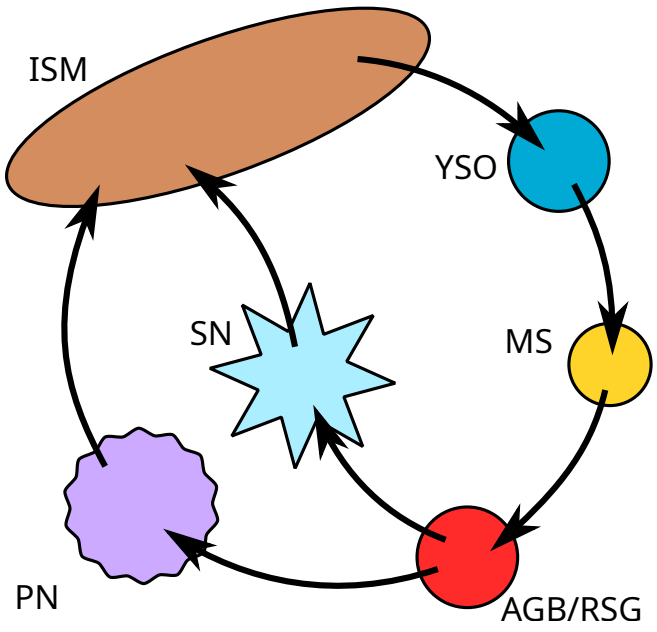

Figure 1.8 Illustration of the internal life cycle of dust in a galaxy.

1.2 AGB Stars in Resolved Populations

The chemical evolution of a galaxy is fundamentally linked to the ISM, which serves as the reservoir of material from which new stars form. Figure 1.8 illustrates the dust life cycle within a galaxy, showing how ISM gas and dust are both destroyed and incorporated into protostars during the collapse and formation of young stellar objects (YSO; Lebreuilly et al., 2020). As discussed previously, chemical enrichment occurs via nucleosynthesis in the cores of Main Sequence and evolved stars, with dust ultimately returned to the ISM through the intense, dust-driven winds of AGB stars. For higher-mass stars ($M_{ZAMS} \gtrsim 8\ M_{\odot}$), core-collapse supernovae (SN) represent the primary channel for dust production and injection into the ISM. This continual cycling and enrichment of baryonic matter gradually increases the metallicity of the galaxy.[3]

Observations of high redshift galaxies ($z \gtrsim 8$) reveal substantial dust masses (Laporte et al., 2017; Tamura et al., 2019; Inami et al., 2022; Algera et al., 2023) formed

[3]It is important to emphasise that this description simplifies the dust life cycle. Dust may also be introduced through processes such as galaxy mergers (Xilouris et al., 2004), Wolf-Rayet (WR) star winds (Cherchneff et al., 2000), and tidal stripping of material from satellite galaxies (Walter et al., 2011). Conversely, dust is removed or destroyed by mechanisms including shocks (Jones et al., 1996), ultraviolet radiation (Draine, 2011), and galactic winds (Hopkins et al., 2012). However, these additional sources and sinks lie outside the scope of this thesis.

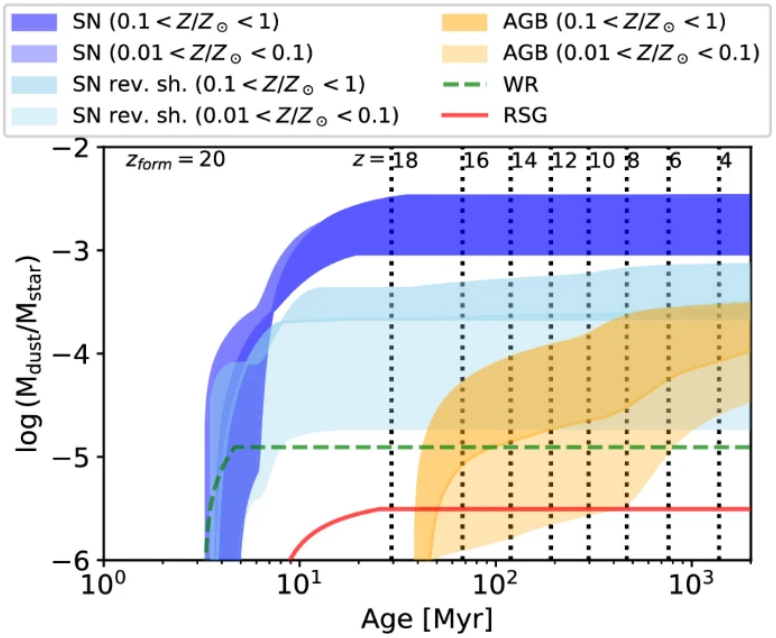

Figure 1.9 Dust enrichment timescales and relative contributions from super novae (SN), AGBs, RSGs and Wolf-Rayet stars. Figure taken from Schneider & Maiolino (2024a).

within the first ~1.5 Gyr after the Big Bang. Figure 1.9 shows the relative enrichment timescales of the key sources of dust in these galaxies. Core collapse SN can produce enormous quantities of dust (Gehrz, 1989), very quickly after star formation (Bressan et al., 2012). Although, the relative rate of the survival of this dust from the reverse shocks is a topic of controversy (Dunne et al., 2003; Krause et al., 2004; Sugerman et al., 2006; Matsuura et al., 2011; Schneider & Maiolino, 2024a). AGB stars, on the other hand, are reliable sources of dust (McDonald et al., 2010; Temim et al., 2015; Whitelock et al., 2018; Jones et al., 2018). Yet, our understanding of this complex evolutionary phase is still limited by a lack of quantitive information. By turning to Local Group galaxies, as analogues of high-redshift, low-metallicity counterparts, we can build a picture of how these stars evolve within a range of environments.

1.2.1 Observing AGB stars

The photospheric emissions and circumstellar dust features from oxygen- and carbon-rich AGB stars are affected by the differing chemistry. This can be characterised in detail through spectroscopy; however, this approach is observationally expensive and impractical for wide-field surveys. Due to the width of the molecular and dust features, broad-band imaging can be used

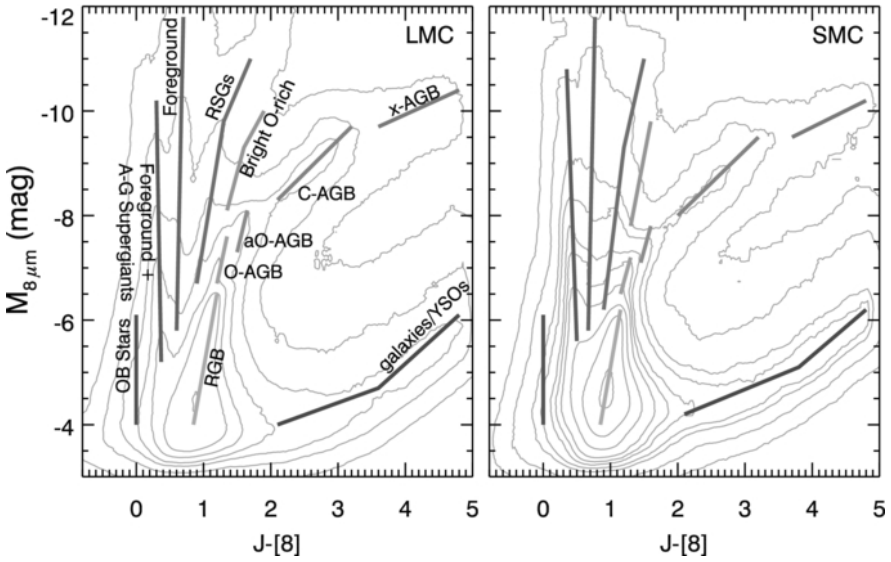

Figure 1.10 Colour-Magnitude Diagram from (Boyer et al., 2011) of the LMC and SMC in combined 2MASS and *Spitzer* photometry. Major evolutionary phases have been overlaid and labelled.

to characterise AGB stars and their spectral classes are differentiable in a colour-magnitude (CMD) or a colour-colour diagram (CCD). In particular, the amorphous carbon in CAGBs is an efficient absorber across a broad wavelength range, especially in the near-IR, which results in substantial reddening of the star's spectral energy distribution (SED) (Groenewegen, 2006; Sloan et al., 2006).

In observational studies, near- and mid-infrared broad-band photometry is often used in AGB identification (Cioni & Habing, 2003; Blum et al., 2006; Sibbons et al., 2012; Hirschauer et al., 2020). Figure 1.10 shows an example CMD from Boyer et al. (2011), combining J photometry from 2MASS (Skrutskie et al., 2006) and 8μm *Spitzer* data in SAGE-SMC (Gordon et al., 2011). The evolutionary phases are overlaid, showing a clear bifurcation of the AGB stars into two branches: the blue OAGB (O-AGB, aO-AGB, and Bright O-rich, as labelled on the figure) and the red CAGB, which splits to the right. The most *extreme* AGBs, exhibiting high mass loss rates, often appear to exceed certain red colour excesses $J-3.6\mu m$ (Meixner et al., 2006; Blum et al., 2006), due to the high level of self absorption within the thick circumstellar shell (Boyer et al., 2011).

1.2.2 C/M Ratio and Its Use as a Metallicity Indicator

Unlike their oxygen-rich counterparts, CAGBs produce carbon internally through nucleosynthesis and dredge it up to the surface during thermal pulsations.

This process leads to a continual enrichment of the stellar atmosphere with carbon, making CAGBs relatively insensitive to the initial metallicity of the galaxy. As a result, CAGB formation is favoured in metal-poor environments, where less oxygen must be overcome for the surface C/O ratio to exceed unity (Karakas et al., 2002; Sloan et al., 2008). Consequently, the number ratio of carbon-rich to oxygen-rich AGB stars (the C/M ratio) serves as a valuable proxy for the metallicity of a galaxy (Iben & Renzini, 1983; Battinelli & Demers, 2005). Global C/M ratios have been compared with spectroscopically derived metallicities in nearby galaxies, revealing a well-defined empirical relation, Equation 1.1 (Battinelli & Demers, 2005; Cioni, 2009):

$$[Fe/H] = -0.47\ log(C/M) - 1.39\,. \tag{1.1}$$

This has been applied to a wide range of galaxies in the Local Group (Sibbons et al., 2015; Ren et al., 2022), confirming it as a reliable metric for measuring metallicity. When mapped spatially across a galaxy, the C/M ratio can reveal metallicity gradients and environmental trends, providing valuable insight into a galaxy's chemical evolution (Hirschauer et al., 2020; Tantalo et al., 2025).

1.2.3 Effect of Metallicity on Dust Production

The metallicity of the environment highly influences the efficiency of dust production in the winds of AGB stars. As mentioned above, the self-production of carbon in AGBs is not reliant on the availability of metals in their cores; therefore, the synthesis of material for carbonaceous dust is not dependent on metallicity. In comparison, the condensation of metal oxides and silicate dust in the winds of OAGBs is highly reliant on the abundance of metals in the ISM when the star first formed. Observations in the low-metallicity Magellanic Clouds; with the SAGE (*Surveying the Agents of a Galaxy's Evolution*; Meixner et al., 2006; Gordon et al., 2011) and HERITAGE (*Herschel Inventory of the Agents of Galaxy Evolution*; Meixner et al., 2013) surveys have shown that indeed carbon-rich dust is more abundant in these low-metallicity environments (Blum et al., 2006; Riebel et al., 2012; Jones et al., 2015a).

The DUSTINGS survey (*Dust in Nearby Galaxies with Spitzer*; Boyer et al.,

2015a) was designed to extend the study of dusty evolved stars to all Local Group galaxies in which individual stars could be resolved by *Spitzer*. The survey observed 50 galaxies out to a distance of ∼1.5 Mpc, spanning a wide range of metallicities ($-2.7 \lesssim$ [Fe/H] $\lesssim -1.0$), and identified over 500 dust-producing AGB stars-including many *extreme* stars in analogues of early-Universe galaxies with [Fe/H] < –2.0. Notably, Boyer et al. (2017) identified 26 dust-producing OAGB stars in the DUSTINGS sample. A further subset of these has since been spectroscopically confirmed as extreme, dust-rich OAGB stars (Boyer et al., 2025 ApJ submitted). These HBB stars, with initial masses M $\gtrsim$ 4 $M_\odot$, are capable of producing significant amounts of dust as early as 30–50 Myr after formation. This finding highlights the significance of evolved stars as efficient dust producers at relatively young stellar ages, reinforcing the notion that AGB stars play a crucial role in forming the substantial dust reservoirs observed in high-redshift galaxies.

1.2.4 Contribution to Dust Budget

In many galaxies, a small number of extreme AGB stars produce the overwhelming majority of the total dust input into the ISM by the evolved stars. These stars, in the late stages of AGB evolution exhibit very high dust production rates ($\sim 10^{-6} - 10^{-4} M_\odot yr^{-1}$) and are heavily obscured. The near-total absorption of the emitted optical light rereadiated at longer wavelengths, makes them bright in the mid-IR. This was a key finding of SAGE (Meixner et al., 2006), which showed that the top 75% of mass-loss in the LMC originated from 4% of the most evolved and dust enshrouded AGBs (Riebel et al., 2012). Although few in number, these individuals produce more dust than the combined contributions of the more numerous low-mass-loss AGBs. These findings have since been extended to Local Group galaxies spanning a range of metallicities, distances and stellar populations, including Sagitarius dIG, Fornax (Lagadec et al., 2007; Boyer et al., 2015b), M33 (Javadi et al., 2013), Sextans A, Leo A (Jones et al., 2018; Dell'Agli et al., 2019) IC 1613 (Dell'Agli et al., 2016) and the SMC (Srinivasan et al., 2016). Across these environments, a small number of AGB stars consistently emerge as the primary dust producers, reinforcing their importance in galaxy-wide dust budgets.

Several studies have estimated that AGB stars contribute the majority of the total stellar dust input in the LMC. Srinivasan et al. (2009), Matsuura et al. (2009) and Riebel et al. (2012) all calculate a total AGB dust injection rate of 6×10^{-3} –

2×10^{-2} $M_{\odot}yr^{-1}$, significantly outweighing the contribution from core-collapse supernovae. Modelling the dust yield Schneider et al. (2014) found that AGB stars account for ~70% of the stellar dust budget in the LMC. Similarly, chemical evolution models by Zhukovska & Henning (2013) support the observations that carbonaceous dust from AGBs is the predominant form of dust returned to the ISM. These results underscore the importance of individual evolved stars with high mass-loss rates in governing the dust life cycle of galaxies. AGB stars are not only efficient dust producers but also significant contributors to the overall dust budget, particularly in the metal-poor environments of the Local Group.

1.3 Resolved Stellar Studies with *JWST*

While studies such as SAGE (Meixner et al., 2006; Gordon et al., 2011), HERITAGE (Meixner et al., 2013) and DUSTINGS (Boyer et al., 2015a) have made significant progress towards understanding dust production mechanisms at low metallicity, the available diversity of environments observable was limited by the sensitivity of *Spitzer* and *Herschel*. Stellar evolution models are reliant on a wide parameter range in observations to provide quantitative feedback; however, our limited existing observations of local stars cover only a small fraction of the ranges of important stellar masses and metallicities (Schneider et al., 2014). Particularly, high-mass stars at low metallicity, which are vital as efficient early Universe dust producers, are scarce due to their rarity (Boyer et al., 2015b). Owing to its unparalleled sensitivity and resolving power, the extent of resolved infrared stellar population studies has expanded dramatically with *JWST*, including our nearest neighbours within the Local Group (~1.5 Mpc; Boyer et al., 2015a) and extending out to more distant systems an order of magnitude further (Hirschauer et al., 2024). In doing so, *JWST* has unveiled thousands of galaxies (Robotham et al., 2011), with diverse and unique stellar populations, star formation and kinematic histories. Figure 1.11 shows a map of some of the galaxy groups and clusters within the range of *JWST*. The inner circle marks the Local Group within 1.5 Mpc, while the outer circle extends to roughly 6 Mpc, illustrating the dramatically widened observational horizon.

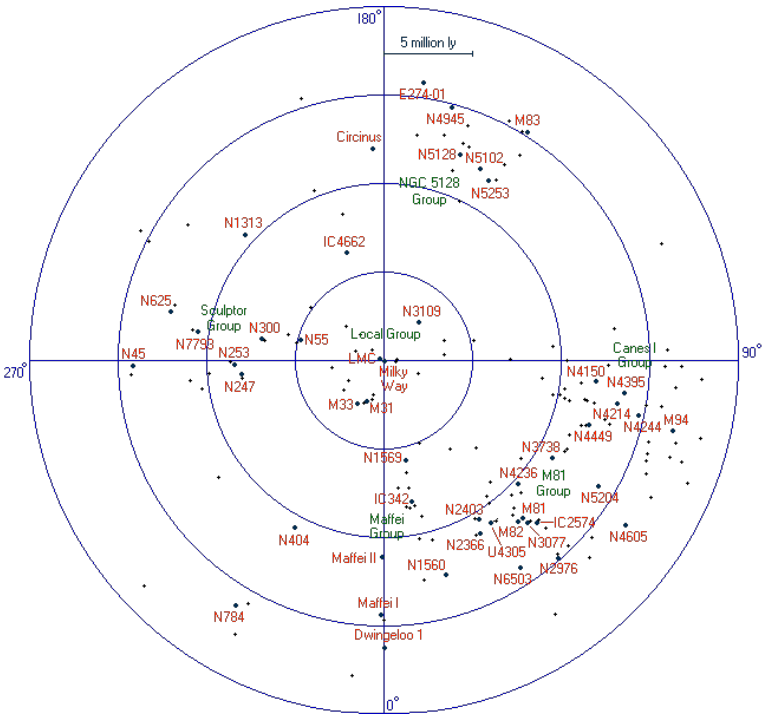

Figure 1.11 Map of the Local Group of galaxies out to 6 Mpc. Image credit: Tom Theuns `https://www.icc.dur.ac.uk/~tt/Lectures/Galaxies/LocalGroup/Back/index.html`

1.3.1 Onboard *JWST*

The two key instruments onboard *JWST* for this work are the Near-Infrared Camera (NIRCam; Rieke et al., 2005, 2023) and the Mid-Infrared Instrument (Rieke et al., 2015; Wright et al., 2023).

NIRCam is the primary imager of *JWST*, covering a wavelength range from 0.6-5μm and two 2.2″×2.2″ fields-of-view (FoV). This baseline spans from the optical red into the mid-infrared. The instrument is split into two modules, "*short*" covers the range 0.6-2.3μm and "*long*" from 2.4-5μm. NIRCam supports a wide range of photometric filters, including sets of narrow, medium, wide and extra-wide bands. Figure 1.12 shows the wavelength coverage of *JWST* (yellow hexagons) with representative filters from the *standard* set, *Spitzer* and *HST*, to demonstrate the width of the NIRCam baseline. Of particular interest are the wide-bands F115W and F200W, which are the closest equivalent to standard Johnson J and K_s. These powerful filters can reach a photometric depth ~28-29 (AB-mag), at a pixel scale 0.031″ per pixel, allowing for deep imaging to identify stars in early evolutionary stages (Jones et al., 2023a; Habel et al., 2024) or to great distances (Hirschauer et al., 2024). Similarly, the F356W and F444W filters on

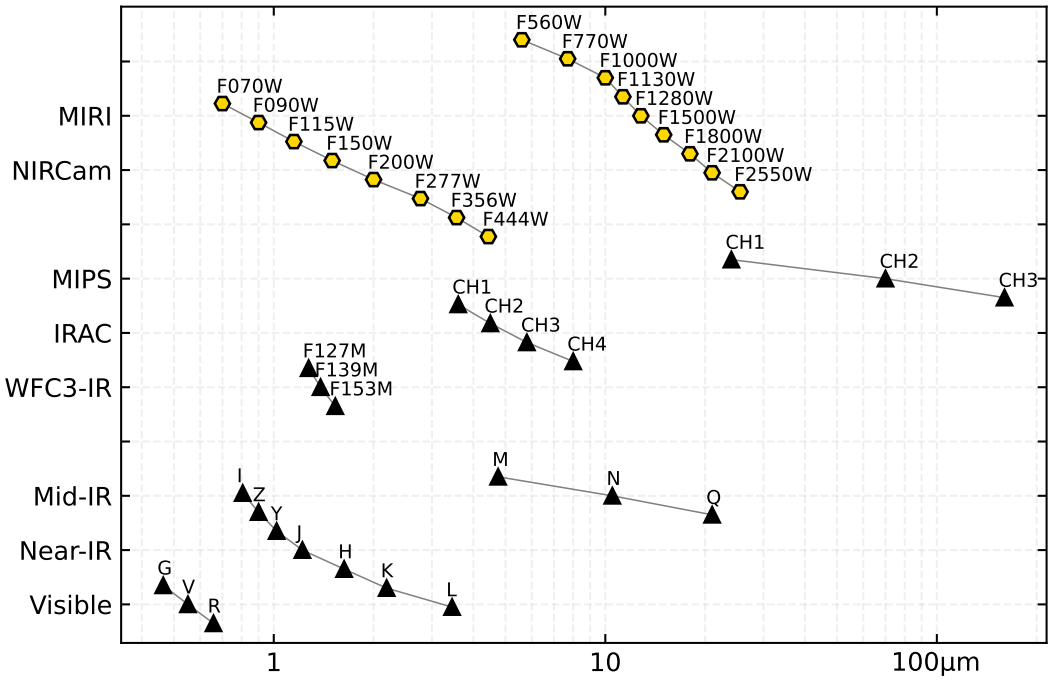

Figure 1.12 Relative wavelength coverage of "standard" photometric bands, covering the visible, near- and mid-IR. Additionally, *HST* WFC3-IR Medium bands, *Spitzer* IRAC and MIPS, and *JWST* NIRCam and MIRI are also shown. Vertical position on the plot is for illustrative purposes only.

the *long* module are excellent *Spitzer* 3.6μm and 4.5μm analogues. With a pixel scale of 0.063″ per pixel resolution, these filters allow for direct comparisons with previous evolved star *Spitzer* studies within the Local Group.

MIRI has modes for imaging and spectroscopy, but the latter is not used in this work. The imaging unit covers the mid-infrared wavelength baseline from 4.9-28.8μm at a pixel scale 0.11″ per pixel. The nine wide-band photometric filters, seen in Figure 1.12, are key for tracing dust emission from the ISM and evolved stars. Noteworthy filters include F770W, which traces polycyclic aromatic hydrocarbon (PAH) molecules, and F1000W, which traces silicates in the circumstellar shells of AGB stars.

1.3.2 NGC 6822

Initially discovered in 1884 with a six-inch refracting telescope, NGC 6822 was described as a "*diffuse-nebula*" that was "*very difficult to see*" by Barnard (1884).

Forty years later, Edwin Hubble found it was host to numerous Cepheid variable stars. By applying the period-luminosity relation to estimate the distance, Hubble (1925) provided evidence that it lay well outside the boundary of the Milky Way. This discovery not only confirmed the existence of other galaxies but fundamentally expanded our understanding of the Universe's structure and scale. We now know that NGC 6822 is an irregular dwarf galaxy and one of our closest neighbours ($d \sim 490 \pm 40$ kpc; Mateo, 1998) in the Local Group.

As a target of numerous stellar population studies, NGC 6822 has been extensively surveyed in both the optical and infrared regimes. An old (~11 Gyr) stellar component within the galaxy was inferred with the first discovery of RR-Lyrae stars (Clementini et al., 2003; Baldacci et al., 2003). After a long period of low star-formation, NGC 6822 began a burst of star formation ~3 Gyr ago (Tolstoy et al., 2001) and has continued to increase over the last $100 - 200$ Myr (Gallart et al., 1996c). It is famously home to some of the largest and brightest star-forming regions in the local universe (Kennicutt, 1979; Hodge et al., 1989; O'Dell et al., 1999; Jones et al., 2019), with active star formation in several localised bright H II regions throughout its disk and central bar (Cannon et al., 2006; Kinson et al., 2021). Its low metallicity ([Fe/H] ≈ -1.2; ~30% $Z_{\odot}$; Skillman et al., 1989; Lee et al., 2006), elevated star formation rate, and rich young populations make it a nearby analogue of galaxies at the universal epoch of peak star formation ($z \sim 1.5 - 2$; Madau & Dickinson, 2014), when the majority of the universe's star formation and chemical enrichment is expected to have taken place.

Optical surveys with the *Hubble Space Telescope* (HST; Wyder, 2001) and *Subaru* (Tantalo et al., 2022) detect old and intermediate-age RC and RGB stars in NGC 6822. The AGB stars within the galaxy trace intermediate age stellar populations and have been extensively studied in the near-IR (see e.g., Cioni & Habing, 2005; Sibbons et al., 2012; Hirschauer et al., 2020; Tantalo et al., 2022) where they can dominate the IR integrated light of a stellar population (Maraston, 2005).

The galaxy has an irregular morphology, with a dense central stellar bar oriented north-south (Hodge, 1977), seen in Figure 1.13. A complex underlying HI distribution extends in two tails more than 0.5° from the centre, with a large $14' \times 10'$ cavity to the east (de Blok & Walter, 2000). The young ($\lesssim 180$ Myr) stellar population has been shown to follow this distribution very closely (Komiyama et al., 2003; de Blok & Walter, 2006). In contrast, the intermediate-old ($\gtrsim$ 2Gyr) population extends far beyond and even possibly exhibits an elongated elliptical shape, almost perpendicular, and likely decoupled from the HI (de Blok &

Walter, 2006; Zhang et al., 2021). Despite the complex nature of the structure of NGC 6822, it is widely believed to be tidally isolated (Battinelli et al., 2006; McConnachie et al., 2021). However, there is an argument that the galaxy just dipped within the virial radius of the Milky Way around ~3−4 Gyrs ago (Teyssier et al., 2012; Zhang et al., 2021; Bennet et al., 2024). The decoupling of the young and old stellar components supports the argument that gravitational interaction warped the HI disk and triggered star formation in NGC 6822 (de Blok & Walter, 2003).

1.4 Overview

As part of the broader effort to understand the life cycle of dust on galactic scales, this study examines the contribution of evolved stars to the dust budget of NGC 6822. This is accomplished by analysing *JWST* imaging data in the near and mid-IR, across the dense central stellar bar of the galaxy.

In Chapter 2, I document the development of a bespoke PSF photometry tool STARBUGII, designed to measure accurate flux values from point sources deeply embedded in crowded dusty environments in which the life cycle of dust takes place. Using STARBUGII on *JWST* NIRCam and MIRI images of NGC 6822, in Chapter 3, I conduct photometry and construct a deep band-matched catalogue of sources. Analysis using luminosity functions and colour-magnitude diagrams reveals a diverse range of stellar populations across the near-IR to mid-IR. In Chapter 4, I improve upon the mid-IR photometry and produce an H-R diagram of the sources in NGC 6822 to a photometric depth below the RC. I identify a subset of these stars as AGBs and RSGs and measure their dust production by fitting model spectral energy distributions. Finally, in Chapter 5 I summarise the findings and outline avenues of potential future work.

Figure 1.13 NGC 6822 seen by MPG/ESO and ALMA. Image credit: ESO, ALMA (ESO/NAOJ/NRAO)/A. Schruba, VLA (NRAO)/Y. Bagetakos/Little THINGS

2 | *JWST* PSF Photometry in Complex Crowded Fields

The thing is, I learned how to fly in Starbug 2.
I'm not used to the controls on Starbug 1.

— Kryten 2X4B 523P

This chapter outlines the development of routines included in the photometry tool StarbugII. It forms the basis of several publications, for which I earned the second author position due to the large quantity of photometric processing involved.

2.1 StarbugII

Extragalactic infrared resolved stellar population surveys have all conducted point source photometry in challenging environments. With *Spitzer*, the SAGE (Meixner et al., 2006; Gordon et al., 2011) surveys used a modified version of the Fortran code DAOPHOT (Stetson, 1987). This code was also applied on the Galactic centre with the *Spitzer* GLIMPSE (Benjamin et al., 2003) legacy survey, but is no longer available. With Herschel, the HERITAGE survey (Meixner et al., 2013) utilised Starfinder (Diolaiti et al., 2000), which is written in the proprietary IDL language. With *HST*, the PHAT (Dalcanton et al., 2012) survey, which reaches to 1.6 microns in the near-IR, used the tried and tested *HST* tool Dolphot (Dolphin, 2000).

In the lead up to *JWST* it was clear that the data would be transformative, however, along with the new age of deep, high-resolution infrared imaging, a specific photometric tool needed to be developed to be capable of detecting

stars over a very wide dynamic range of luminosity and suitable for both field stars and dense stellar clusters with complex backgrounds. *JWST* would bring with it a broad range of programs covering wide wavelength baselines (0.7 - 25 microns) across large mosaics. The point sources will be crowded due to the depth sensitivity, and the regions will be compact. Similarly, due to the population traceable by *JWST*'s observable wavelengths, the areas of interest are likely highly dusty (particularly star-forming galaxies and clusters). This premise was confirmed immediately with the very first images released from the telescope. The calibration teams would work on some of the most accurately characterised PSFs, allowing for high-quality photometry to be possible. As the data come in from the telescope, the international stellar populations community would need to adapt to many unique Early Release Observations (EROs) and Guaranteed Time Observations (GTOs) programs. For instance, the WINGS GTO team, which I am a member of, planned to image super star clusters in the Nearby Magellanic clouds at a distance of 50 kpc to the extremely metal-poor dwarf galaxy 1Zw18 at ~18 Mpc.

To prepare for the influx of data, I developed STARBUGII, a PYTHON photometry tool, before the initial data release from the telescope, with the express intention of tackling the problems of data complexity, program diversity, adaptability and ease of use. STARBUGII is now a fully-realised suite of photometric tools, open source and has been adopted by both collaborations which I am a member of (Jones et al., 2023a; Nally et al., 2024; Lenkić et al., 2024; Hirschauer et al., 2024; Habel et al., 2024; Nayak et al., 2024b) as well as the broader community with which I have no connection (Li et al., 2024; Zeidler et al., 2024; Antoniadis et al., 2025).

Section 2.2 describes the challenges of detecting sources in complex regions, Section 2.3 discusses characterising dusty diffuse backgrounds, and Section 2.4 covers flux measurements via PSF photometry. Routines for catalogue matching are discussed in Section 2.5 and artificial star testing in Section 2.6. In Section 2.7, I detail some of the programs that have applied STARBUGII to conduct all photometric processing. Finally, in Appendix A, I outline a typical run through of STARBUGII from raw data to a final band-matched point source catalogue.

2.2 Source Detection

Figure 2.1 shows an example complex dusty star-forming region NGC 602 in the SMC from Zeidler et al. (2024), which contains many very deeply embedded young sources. It is immediately clear in this region that the faintest point sources are less bright than the most brightly illuminated formations in the dust structures. This poses one of the key problems in conducting photometry on images like this: 'How do you detect objects fainter than a highly variable background?' To address this issue, I developed the source detection routine of STARBUGII, which uses a three-fold ensemble of detection methods, each manipulating the image in some manner to target a different "type" of point source, (a) the bright, (b) the faint and (c) the deeply embedded. In doing so, the source detection creates three separate catalogues for the image, in which there will be some overlap in membership, but the bulk of these sources will be unique to each catalogue. These three catalogues get merged using the matching routine described in Section 2.5 to form a master source list for the image.

2.2.1 PLAIN Detection Method

The first subroutine, "PLAIN", targets the brightest, cleanest and least crowded sources in the image. The routine models the background with a simple masked median of the whole image. While bright complex backgrounds will not be well characterised with this technique, it serves as a versatile baseline method to detect high-quality sources in a large variety of images, keeping STARBUGII a generalised and powerful tool for other telescopes. The median subtracted array is passed to the core detection code within STARBUGII, an augmented version of PHOTUTILS DAOStarFinder (Bradley et al., 2022). This base is an implementation of DAOFIND (Stetson, 1987), which convolves the raw pixel array with a 2-dimensional Gaussian, whose width is taken from the FWHM of the image PSF. The routine scans the convolved array for local maxima above a threshold. The threshold is a user-defined factor SIGSRC, measured as the number of standard deviations (σ) above the array median. In general, a high-quality source detection is said to be above a 5σ threshold, but this may be lowered as far as 3σ if a greater depth is required.

STARBUGII augments this process slightly by clipping faint pixels from the array

Figure 2.1 An example dusty star forming region with bright, faint and deeply embedded sources. STARBUGII has been used in this data set by Zeidler et al. (2024) to detect the extragalactic brown dwarves. Image credited ESA/Webb, NASA & CSA, P. Zeidler, E. Sabbi, A. Nota, M. Zamani (ESA/Webb) with *JWST* NIRCam F115W+F140M+F150W (blue), F210M (cyan), F277W (green), F335M (yellow), F356W (orange), and F480M+MIRI-F1000W (red).

to reduce the number of faint spurious detections found in the noise. This is done by iteratively measuring the median of the image array, and masking out pixels that fall below SIGSKYσ until the process converges. A high SIGSKY threshold will eliminate a large amount of variable background features like dust columns, but may also remove faint stars in the process. Finding the balance between missing faint sources and including many low-quality, noisy detections requires user iteration to optimise for the science goals necessary.

Figure 2.2 shows how varying the SIGSRC and SIGSKY thresholds can affect the detection rate. The three columns illustrate how altering SIGSRC eliminates sources that are not significantly brighter than the local environment in which they reside, where SIGSKY reduces the overall brightness limit, allowing detections to occur. Reducing SIGSKY is very effective at allowing these faint and embedded sources, but can open the door to a large number of spurious detections. Using it in conjunction with SIGSRC acts as a first pass of quality control in the routine.

2.2.2 BGD2D Detection Method

The second subroutine is designed to locate the faintest sources in the input image. The routine "BGD2D" aims to model the complex dusty backgrounds in a low-resolution two-dimensional form. BGD2D makes use of the function PHOTUTILS Background2D to construct a spatial flux estimation of the image.

The Background2D function passes a box kernel across the whole image, and models the kernel position in the image with a sigma-clipped median. The resulting array is a blurred array representative of the broad-scale features of the image. This effect is similar to defocusing the image, thereby losing the fine detail of individual point sources and instead highlighting the underlying structure of the background. Selecting the kernel size, or BOX_SIZE in the STARBUGII parameters, will alter the blurring effect. A large BOX_SIZE will create a globally more representative background estimate, less affected by bright sources in the image, but may lose some of the important small-scale bright details in the background that are masking the sources. Conversely, choosing a small value for the BOX_SIZE will create a highly accurate representation of the image but will be more affected by noise and bright pixels.

STARBUGII takes this blurred array and subtracts it from the original raw data array, which amplifies sharp edges in the image, resulting in an "unsharp mask".

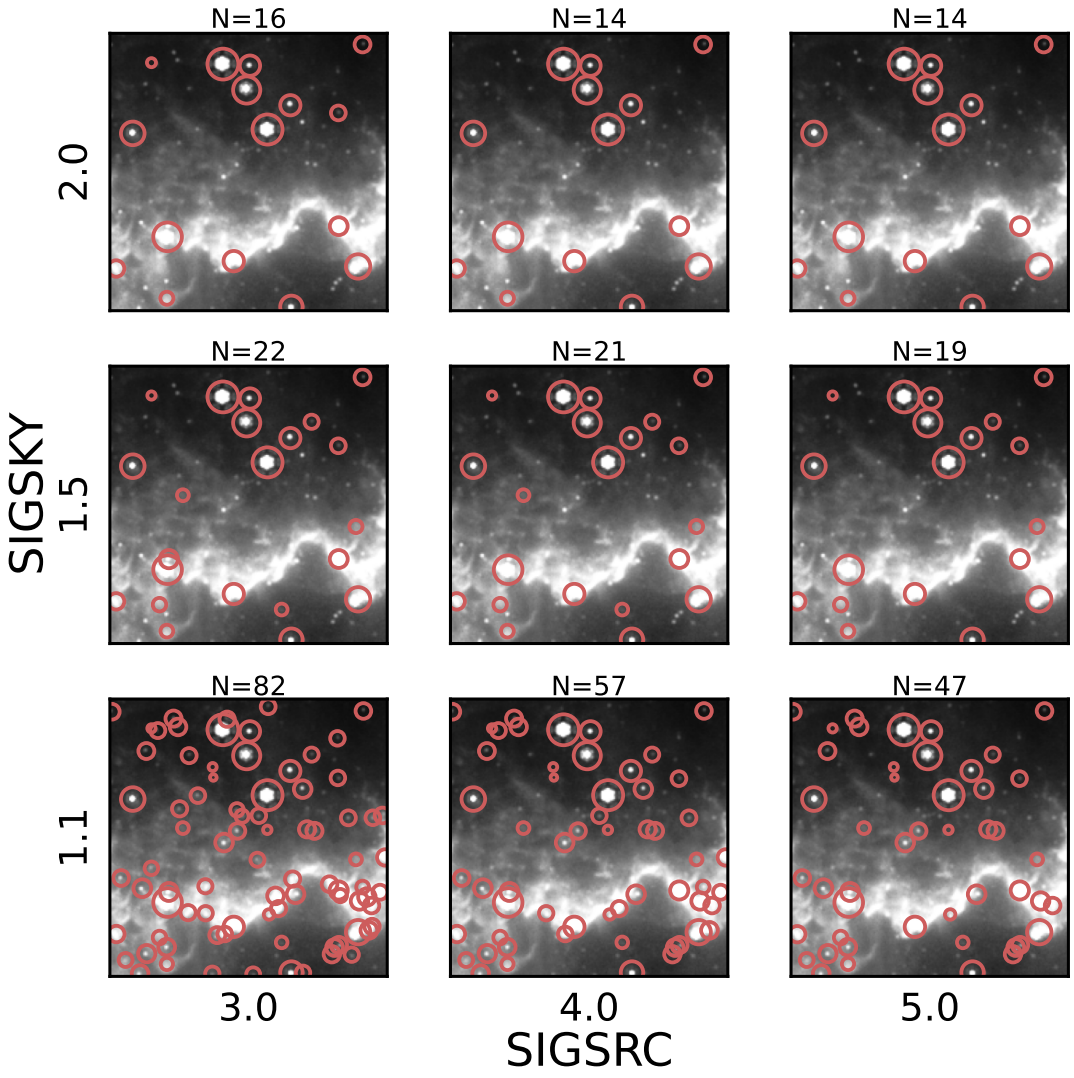

Figure 2.2 The effect of altering SIGSRC and SIGSKY on the level of source detection. Columns represent the effect of setting SIGSRC to a value from the set (3.0,4.0,5.0). Rows represent the effect of setting SIGSKY from the set (1.1,1.5,2.0). The number of source detections is indicated at the top of each panel.

These edges are mostly the peaks of the point sources, as can be seen in the lower left panel of Figure 2.3, where the resulting background subtracted array on which STARBUGII will detect is seen in the right-hand panel. This process effectively increases the brightness of a star relative to its local environment, thus increasing the detection rate of faint sources without needing to drop the detection threshold.

The unsharp mask subtracted image is passed back to the PLAIN core detection method to locate point sources.

2.2.3 CONVL Detection Method

One method of edge detection is called *Laplacian of Gaussian* (*LoG*). The Laplacian is the second-order derivative operator, which can be written in a multi-variant form with Equation 2.1. When this is applied spatially to the image array, edges represent sharp rates of change that result in high amplitudes in the Laplacian. However, noise in the raw image array also produces sharp gradients in the Laplacian, which act to confuse the source detection rather than enhance it. For this reason, a Gaussian filter can be applied to smooth the image beforehand. The combination of these two operations can be written in general with Equation 2.2

$$\Delta^2 f(x,y) = \frac{\delta^2 f}{\delta x^2} + \frac{\delta^2 f}{\delta y^2}\,, \tag{2.1}$$

$$LoG(x,y) = \nabla^2 G(x,y,\sigma) * f(x,y)\,. \tag{2.2}$$

The Ricker Wavelet (ψ) is defined as the negative second-order differential of a Gaussian Function (Equation 2.3)

$$\psi(x,y) = (1 - \frac{x^2+y^2}{\sigma^2}) e^{-\frac{x^2+y^2}{2R^2}}\,, \tag{2.3}$$

where (x, y) are the pixel coordinates and $\exp(-\frac{x^2+y+2}{2R^2})$ is the Gaussian kernel with width R. The third subroutine is the "convolutional" CONVL method and involves convolving the image array with a Ricker Wavelet. The concept is that the convolved image will have high points in the areas where a point source sits, but will not react strongly to the broader gradients from the dust structures underneath. This makes it perfect for detecting sources that are deeply embedded in said dust filaments, which are prevalent in star-forming regions and galaxies.

The lower right panel of Figure 2.3 shows the effect that the convolution has on the raw data array. It can be seen that the entire dust structure underpinning the image has been nullified by the routine, and only a series of relatively uniformly bright peaks remain. Running a peak detector on this residual image can result in a very large number of detections of some highly embedded sources.

The radius of the Ricker Wavelet kernel determines the point source scale to which the routine is sensitive. Setting it small (RICKER_R=1) is very effective at finding sources in NIRCam due to the small PSF FWHM. However, if this is used in longer wavelength MIRI images, it becomes less sensitive to the broader PSF and begins to falsely detect noise in the background. I find that slowly increasing the value of RICKER_R in integer steps is necessary to balance complete catalogues with over-detecting.

2.2.4 Finalising the Source List

The three detection subroutines described above will each produce their source list. By setting their relevant parameters and thresholds, each routine will perform slightly differently and can build a unique list of sources, containing many that the other routines may not have detected. STARBUGII combines these three source lists into a single master detection list, using a nearest neighbours matching routine described later in Section 2.5.1. With this master source list, STARBUGII assesses the morphology of each source to determine its likelihood of being a quality point source or a contaminating poor detection. To do so, the original, unmodified image array is assessed at the central position of each source and values of SHARPNESS, SMOOTHNESS, ROUNDNESS1 and ROUNDNESS2 are determined. Finally, an initial flux estimate for each source is automatically measured using aperture photometry, as discussed in Section 2.2.5.

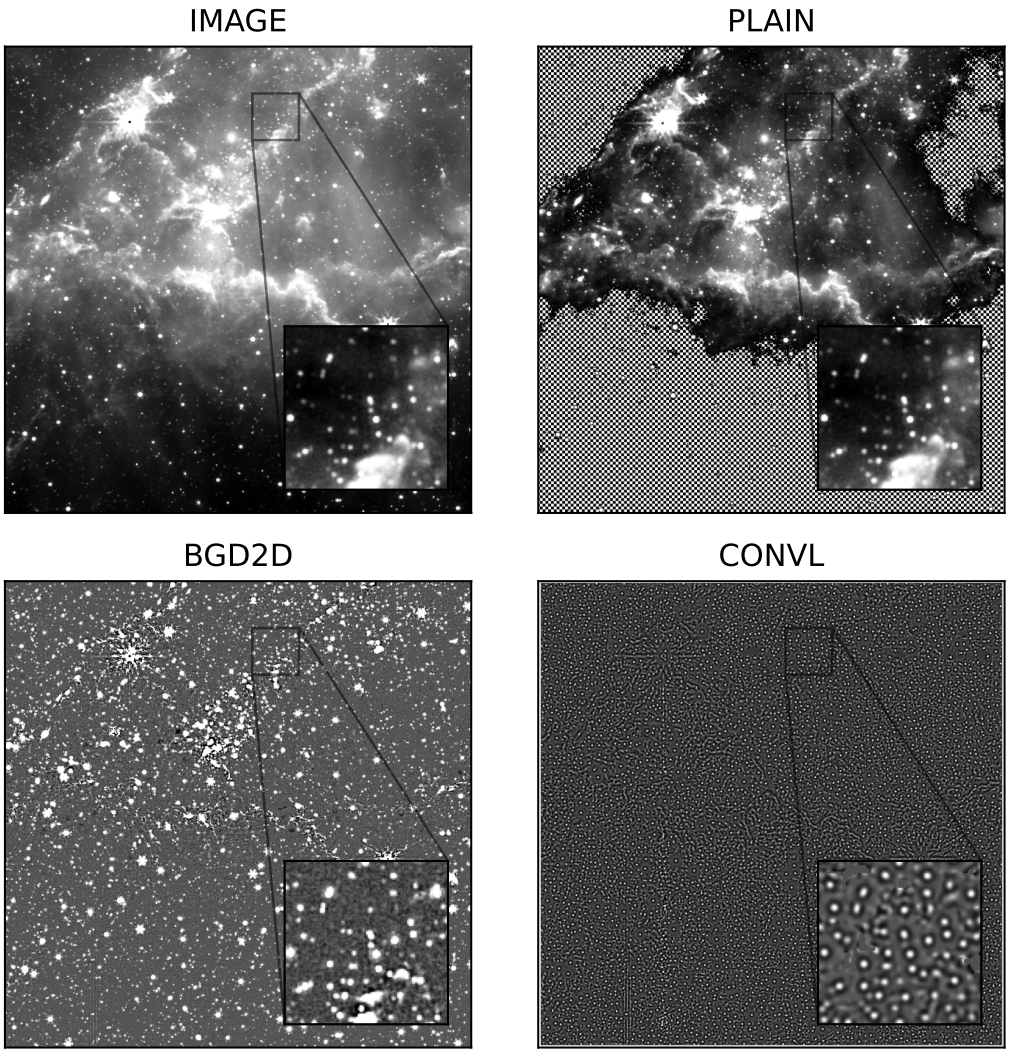

Figure 2.3 A comparison with the raw image array (upper left) with the modified array, on which each detection subroutine detects. The PLAIN sigma-clipping method is shown in the upper right, BGD2D lower left and CONVL lower right. The inset regions shown are zoomed-in views of the arrays (each covering the same region on the sky), showing how each routine affects the array.

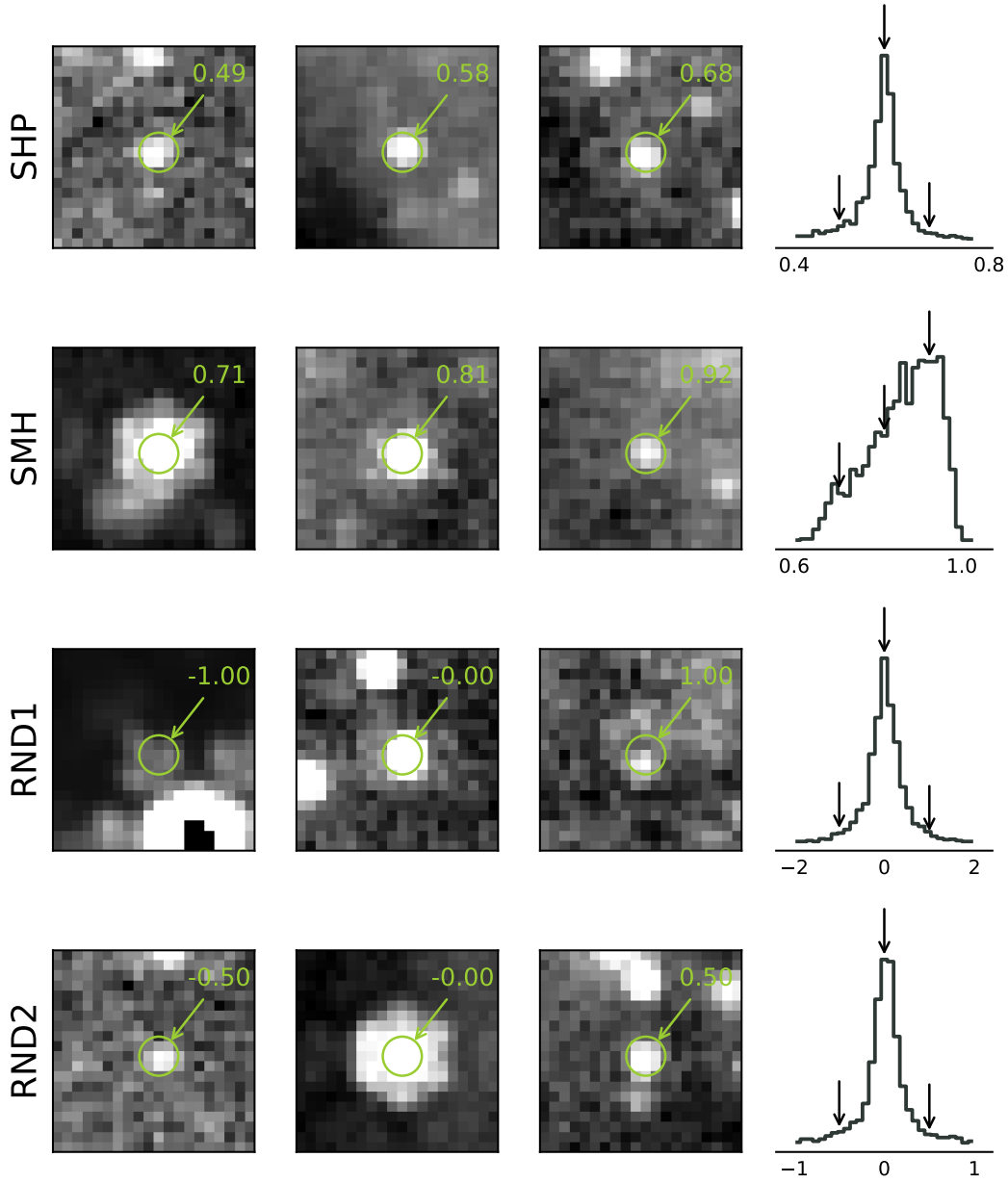

Figure 2.4 Geometric properties of point sources in an image. From top to bottom, rows show SHARPNESS, SMOOTHNESS, ROUNDNESS1, ROUNDNESS2. Each row shows an example of a source in the lower, middle and upper bounds of the parameter distribution. The final column shows the overall distribution of the geometric parameter in the example image, Figure 2.3.

Sharpness

The first morphological parameter is a measure of SHARPNESS, i.e. is the source particularly narrow for its intensity, or height in the image array. SHARPNESS (SHP) is calculated on the raw image as the ratio of the difference between the peak pixel of the source and the mean pixel value of the source (excluding the peak), to the maximum value of a spatial gaussian fit to that source. This is described by Equation 2.4, where I_i is a pixel in the raw image associated with the source, I_0 is the source peak, G_0 is the gaussian peak, and n is the number of pixels

$$SHP = \frac{I_o - \sum_{i=1}^{n} I_i/n}{G_0} \,. \tag{2.4}$$

For the majority of point sources in the image, the values of I_0 and G_0 are comparable; therefore, the function is responsive to the values of the other pixels within the aperture of the source. To interpret Equation 2.4, take the case of an archetypal cosmic ray in the image, a single (or a small number of) hot pixel(s). The peak I_0 overpowers the numerator, and SHP is large. Conversely, in the case where a bright point in the background dust structure has been detected, the mean source pixel value is more comparable with I_0, resulting in a small value of SHP. Finally, in cases of completely spurious detections that occur occasionally, I_0 and G_0 are incomparable, and the value for SHP can become greater than 1 or less than 0; this indicates a poor detection. The top row in Figure 2.4 shows the morphology of sources in the raw image across the distribution of SHARPNESS values.

By inspecting the SHARPNESS distribution, as it relates to the raw image, it is possible to select an upper and lower boundary for these to discard likely bad detections. In STARBUGII this is supplied with the SHARP_HI and SHARP_LO parameters. The SHARPNESS distribution is completely dependent on the PSF of the telescope, as the median SHARPNESS of a "good quality" source might vary. Similarly, the level of conservativeness required to remove contaminations without removing obscured point sources may be affected by the level of Poisson noise in the image, which is affected by the process of mosaicing multiple individual exposures. As such, the bounds of SHARPNESS need to be individually chosen to reflect the nature of the particular image to which it is being applied.

Smoothness

Introduced in STARBUGII is the concept of source SMOOTHNESS, this is analogous to SHARPNESS but viewed from the opposite direction. A smooth source has a more gentle gradient from the immediate surrounding area to its peak. SMOOTHNESS (SMH) is defined as the ratio of the mean pixel value between a large and small aperture around the star. This is described in Equation 2.5

$$SMH = \frac{\sum_i^m I_i/m}{\sum_i^n I_i/n}, \tag{2.5}$$

where m and n are the number of pixels in the large and small apertures, respectively. The large aperture is 1.5 times the size of the small one.

The interpretation of Equation 2.5 is that the gradient of a "good quality" point source should have a decreasing mean pixel value as fainter pixels further from the centre get added to the calculation. However, if the source is particularly broad, as in the case of a clumpy dust structure or background galaxy, the wider aperture will not be so faint in comparison to the inner aperture; as such, the value of SMOOTHNESS approaches unity. Conversely, in a more pointed source like a cosmic ray, the denominator of Equation 2.5 will overpower the numerator, and the value approaches zero. The second row of Figure 2.4 shows the distribution of source SMOOTHNESS of the image array.

One caveat with this morphological parameter is that the choice of base aperture radius will affect the result, especially in crowded fields. If the apertures are too large, the risk of flux contamination with neighbouring sources increases. In the case that a nearby source is brighter than the source of interest, the outer aperture may have an artificially high mean, which can make the source appear more "smooth". The default choice of aperture is the same as that selected for the aperture photometry routine (see Section 2.2.5) conducted by STARBUGII; here, the user has considered what an appropriate radius to use concerning the stellar density in the image.

Roundness

If SHARPNESS and SMOOTHNESS look at the intensity profile of a point source, with respect to its surroundings, we need a measure of how uniform the shape of the source is. ROUNDNESS, first introduced by DAOPHOT (Stetson, 1987),

comes in two forms; ROUNDNESS1 and ROUNDNESS2.

ROUNDNESS1 investigates the circular symmetry of the source. It is measured as the two-fold (bilateral) symmetry between the x and y axes. In practice, this is done by first collapsing the source independently onto the x- and y-axis, and fitting one-dimensional gaussian profiles to each. By summing the residual between the collapsed source and the fitted gaussian, and inputting this into Equation 2.6, ROUNDNESS1 is calculated. In this equation, $R_{x,y}$ is the sum of residual values in either direction

$$RND_1 = \frac{R_x - R_y}{R_x + R_y}\,. \tag{2.6}$$

The numerator describes the two-fold symmetry, where differences between the x and y profiles will result in this being non-zero. The denominator normalises any difference, making it more meaningful across the whole array of sources detected.

ROUNDNESS2 looks at how elongated a source is on the image. ROUNDNESS2 is defined as the ratio between the difference of the fitted one-dimensional gaussian profile heights ($h_{x,y}$) and the sum of the heights

$$RND_2 = 2\frac{h_x - h_y}{h_x + h_y}\,. \tag{2.7}$$

The ROUNDNESS2 distribution is symmetric about zero. A source that has the same x profile as y will have an $RND_2 = 0$, whereas, in the case of a source elongated along the y-axis, the numerator becomes positive and the value of RND_2 will be greater than zero. A negative value is just the same, but along the other axis instead.

The lower rows of Figure 2.4 show sources drawn from the distributions of ROUNDNESS1 and ROUNDNESS2. In the centre panel, a perfectly ROUND source ($RND_1 = RND_2 = 0$), and the adjacent panels show sources elongated in the horizontal (left) and vertical (right) directions. The ROUNDNESS2 distribution is often tightly peaked at $RND_2 = 0$ and trails off with two wings; the elongated sources presented here are examples of objects that lie just outside of the central peak and are therefore potential contaminants. However, as with every

morphological parameter, the level of conservativeness of the selected boundaries depends largely on the scientific goal in mind. Pushing the limits of detection to recover the very faintest or embedded objects will always result in low signal-to-noise objects with peculiar morphologies. The user always weighs the balance between purity and contamination.

The two ROUNDNESS parameters measure similar but intricately different aspects of source geometry. As with SHARPNESS and SMOOTHNESS, they reflect the shape of the PSF and the level of noise in the image so the quality bounds need to be specified for the image that is being analysed and it cannot be guaranteed that a chosen value for one image is appropriate for another. In the case of *JWST*, the PSFs exhibit a long fringing, which is symmetric but is not circular; as such, the ROUNDNESS1 distribution is almost always wider than the ROUNDNESS2 distribution, and the limits of one do not necessarily apply to the other. In STARBUGII these boundaries are selected by the user through the ROUND1_HI and ROUND2_HI parameters.

2.2.5 Aperture Photometry

Initial photometric measurements of the detected point sources are conducted using aperture photometry. This method is computationally cheap but comes at the cost of accuracy in crowded environments or areas with complex backgrounds. This trade-off makes it suitable for an initial measure of point source fluxes.

Aperture photometry operates in two stages: summing the total flux in a circular aperture and then subtracting the contribution to that flux from the background, as measured in a "sky annulus" surrounding the source. The cumulative source flux is scaled to correct for the modelled quantity of flux that lies outside the aperture, called the aperture correction.

The selection of circular aperture size is crucial to obtaining accurate photometry; if this is too large, contamination from nearby objects can affect the value. However, a small aperture will measure a smaller number of pixels and a smaller fraction of the sources' encircled energy, leading to an over-reliance on the aperture correction to scale the final value. While a well-modelled aperture correction is essential for accurate photometry, using it to correct photometry can lead to larger variance from noise in the image. Complicating the problem further is that the full-width half maximum (FWHM) of the source PSF depends

on wavelength; therefore, a value of aperture radius used in one image may not be appropriate for another. To counter this issue, STARBUGII provides the functionality to scale the aperture size to encapsulate an equal fraction of the encircled energy, calculated using model PSFs (this is discussed in Section 2.4.2).

Sky Subtraction

While simply averaging the pixel values in the background annulus is sometimes appropriate, in complex and crowded environments like Figure 2.1, we need to select the pixels more carefully. In STARBUGII, the pixels inside the sky annulus are sigma-clipped, removing nearby stars that might overlap the annulus. The median is calculated to negate the high influence of remaining bright pixels in the annulus. As with aperture radius, the chosen values of the inner and outer sky annulus radius are important and highly customised to the image being analysed. In the complex environments being discussed, a large sky annulus, with large inner and outer radii, will not cover a representative area in the background, and the subtraction could introduce unnecessary uncertainty. Similarly, if the annulus is too small, it may be contaminated by the PSF fringes of the star, leading to over-subtraction. Wide annuli, with a small inner radius and large outer radius, will encapsulate a large number of pixels, resulting in a well-measured value of the sky, but are more likely to be contaminated by nearby stars, whereas narrow annuli will not collect enough pixels to measure the sky accurately. STARBUGII allows the user to set these values through the SKY_RIN and SKY_OUT parameters.

Photometric Uncertainties

Measuring flux uncertainties in aperture photometry requires combining as many measurable sources of error as possible. A combined error would typically look something like

$$\sigma_{\text{total}} = \sqrt{\sigma^2_{\text{src}} + \sigma^2_{\text{sky}} + \sigma^2_{\overline{\text{sky}}} + \sigma^2_{\text{readout}} + \sigma^2_{\text{flat}} + \sigma^2_{\text{dark}}}\,. \tag{2.8}$$

The constituent components of this function can be broken down with Equations 2.9. The primary component is σ_{src}, which, due to the Poisson nature of photons hitting a detector, is simply the square root of the cumulative flux in the aperture divided by the detector GAIN. The uncertainty in the sky measurement is broken down into the root mean square (rms) noise in the sky (σ_{sky}) and the

error on the averaged background value ($\sigma_{\overline{\text{sky}}}$). These rely on calculating the standard deviation of the sky annulus (σ_{annulus}), and the relative pixel areas of the aperture and sky annulus ($A_{\text{aperture,annulus}}$). The readout noise ($\sigma_{\text{readout}}$) is measured with the noise factor R across the array, flat field uncertainty (σ_{flat}) uses the flat-field fraction f_{flat} and dark current uncertainty (σ_{dark}) uses the poisson nature of the dark array. The separate components of uncertainty are given in Equation 2.9:

$$
\begin{aligned}
\sigma_{\text{src}} &= \sqrt{F_{\text{src}}}\,, \\
\sigma_{\text{sky}} &= A_{\text{aperture}} \cdot \sigma^2_{\text{annulus}}\,, \\
\sigma_{\overline{\text{sky}}} &= \frac{A^2_{\text{aperture}} \cdot \sigma^2_{\text{annulus}}}{A_{\text{annulus}}}\,, \\
\sigma_{\text{readout}} &= R\sqrt{F_{\text{src}}}\,, \\
\sigma_{\text{flat}} &= f_{\text{flat}} \cdot F_{\text{src}}\,, \\
\sigma_{\text{dark}} &= \sqrt{F_{\text{dark}}}\,.
\end{aligned}
\tag{2.9}
$$

The *JWST* reduction pipeline (Bushouse et al., 2022) provides an error (ERR) array as one of the FITS extensions of the final image products. This is a two-dimensional array combining all the instrument-based components of the uncertainty calculation (σ_{src}, σ_{flat}, σ_{dark}). As such, when operating on *JWST* images, STARBUGII simplifies Equation 2.8 into Equation 2.10

$$
\sigma_{\text{total}} = \sqrt{\sigma^2_{\text{ERR}} + \sigma^2_{\text{sky}} + \sigma^2_{\overline{\text{sky}}}}\,. \tag{2.10}
$$

Every source in the detection list will have flux measurements with aperture photometry and an estimated error, as calculated using the above function. These fluxes and uncertainties are in the base image unit, which in the case for *JWST* are converted to Jy as discussed later in Section 2.4.4.

Aperture Corrections

The PSF of a point source theoretically reaches to infinity with an ever-decreasing intensity. By measuring flux within an aperture, a fraction of the source flux gets neglected from the measurement. To counter this effect, an "aperture correction" is applied. This is a dimensionless value which is multiplied by the measured flux to counteract the aperture effect.

The aperture correction is modelled by measuring the total flux inside a series of concentric apertures, and the profile of flux growth is either parametrised or inserted into a lookup table. When using STARBUGII on *JWST* data, the aperture corrections have been calibrated accurately using WEBBPSF and are available through the CRDS calibration files Bushouse et al. (2022). However, this has been provided as a lookup table with base increments of fraction encircled energy and aperture radius corresponding to this. While this provides a readable, intuitive understanding of the magnitude of the correction effect, we often conduct aperture photometry in the units of pixels rather than fractions of encircled energy. In STARBUGII both are possible, but interpolation is required to convert between them. To determine an appropriate measure of the aperture correction for a given aperture radius, the table's "aperture correction" versus "radius" curve is interpolated to the relevant aperture radius. Figure 2.5 shows a series of aperture correction curves for MIRI filters and two examples in green of a conversion between the three measures.

Figure 2.5 demonstrates the importance of the choice of aperture radius. The curves are very steep at small radii, and as such, the uncertainty introduced by the interpolation is amplified. The aperture corrections apply large multiples to the flux measurements (between 1.5 and 5), and as such, slight differences in the aperture correction interpolation may significantly affect the photometry.

2.2.6 Results

The comprehensive collection of source detection subroutines enables the recovery of point sources in highly challenging environments. One result of this in action can be seen in Figure 2.6, a plot taken from (Habel et al., 2024), showing embedded candidate YSOs detected in blue, magenta and red (with increasing respective confidence) within the dusty filaments in the star-forming region of NGC 346. These objects closely trace the dusty regions where they form and

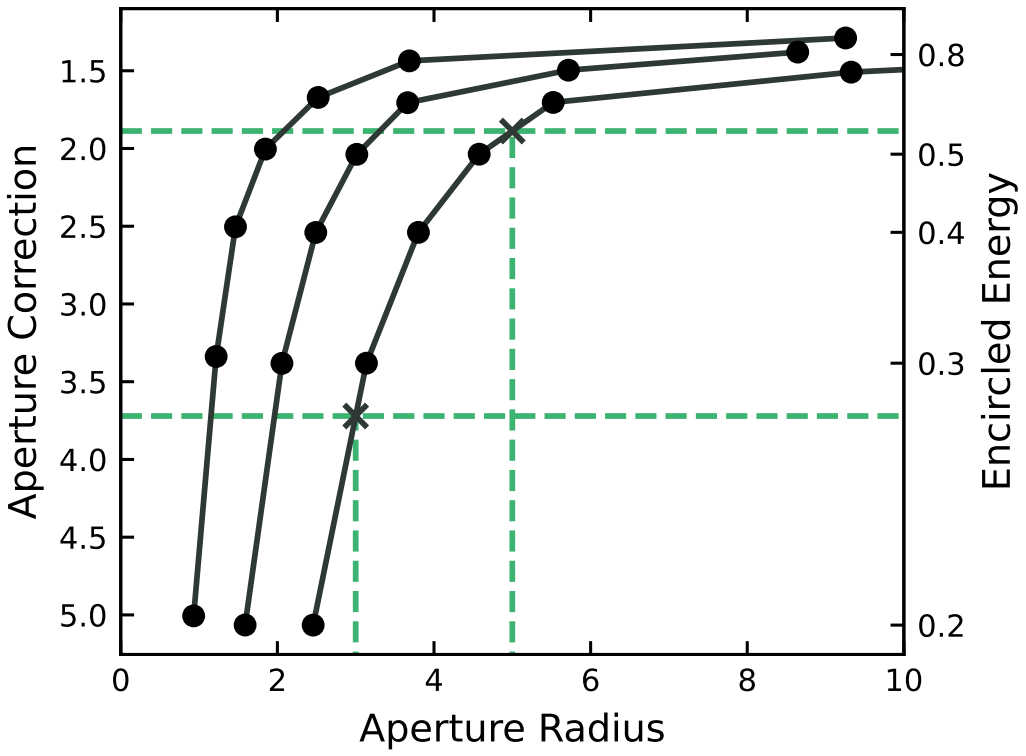

Figure 2.5 Aperture correction scale factor versus aperture radius curves for three MIRI filters. The right axis shows the corresponding fraction of encircled energy for a given aperture correction. The green dashed lines show interpolated values to convert between the three distinct measurements.

could, therefore, only be detected with the specific routines outlined.

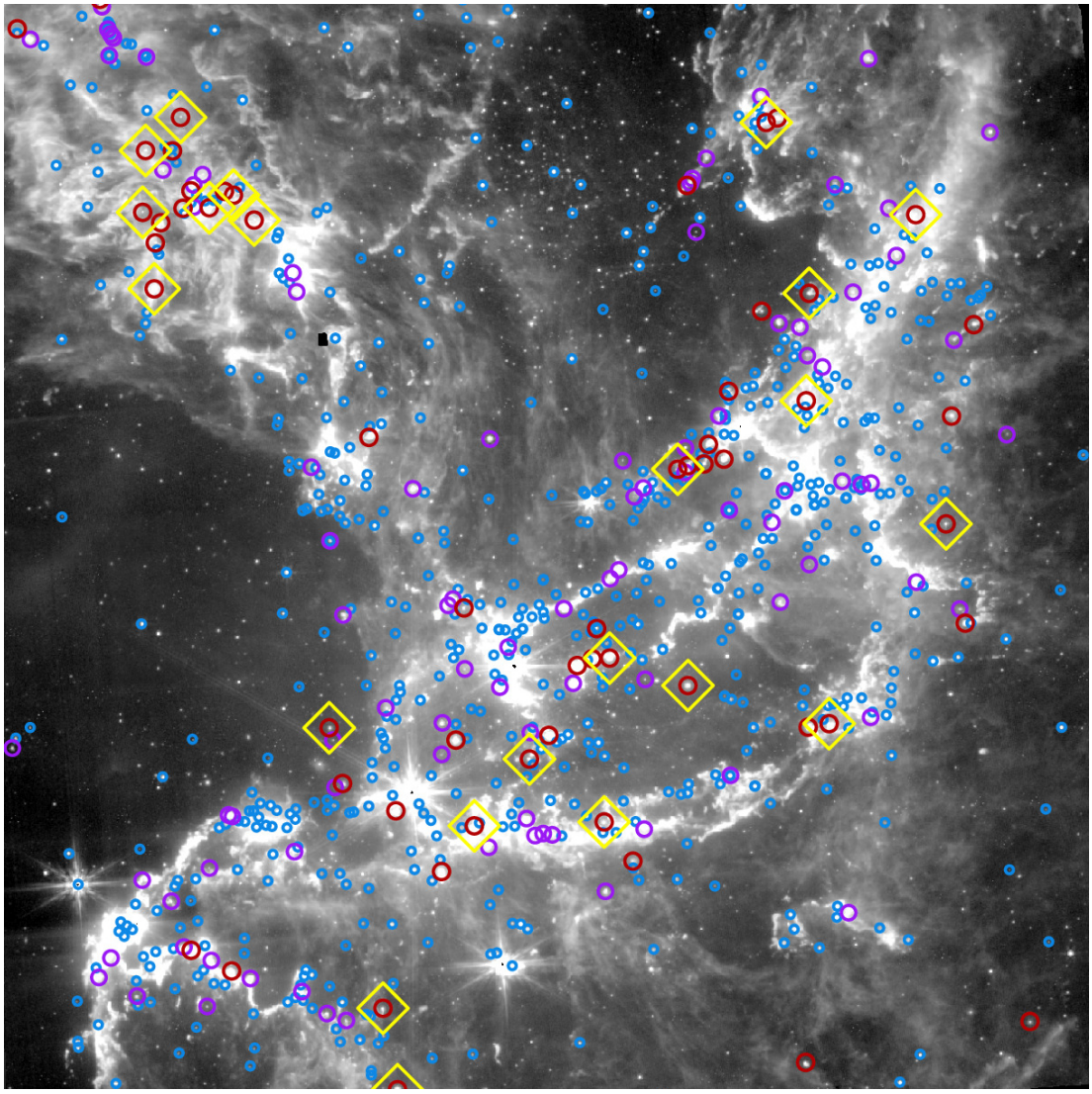

Figure 2.6 Spatial figure showing the detection of embedded YSOs on the dusty background of NGC 346. Figure taken (and cropped) from (Habel et al., 2024) to demonstrate the effectiveness of STARBUGII's source detection routine on real data. Colours represent different confidence levels of YSO classifications, ranging from yellow (highest) to blue (lowest).

In comparison with the source detection routine provided by the *JWST* reduction pipeline, Figure 2.7 shows the relative detection rate between *JWST* (green) and STARBUGII (grey). This figure illustrates this concept through a luminosity function, which shows the relative number of detections at different magnitude scales. The upper panel shows a MIRI field in NGC 6822, and the lower shows a NIRCam field. In both cases, default detection parameters are used for STARBUGII and *JWST*. It can clearly be seen that STARBUGII recovers an order of magnitude

greater number of point sources. In the upper panel, this allows a large number of objects below the *Tip of the RGB* (TRGB) to be detected, which were otherwise invisible. Similarly, in the lower panel, hundreds of thousands of sub-RC stars are detected, which could, for example, facilitate the creation of precise RGB population maps to trace tidal interactions in the galactic outskirts.

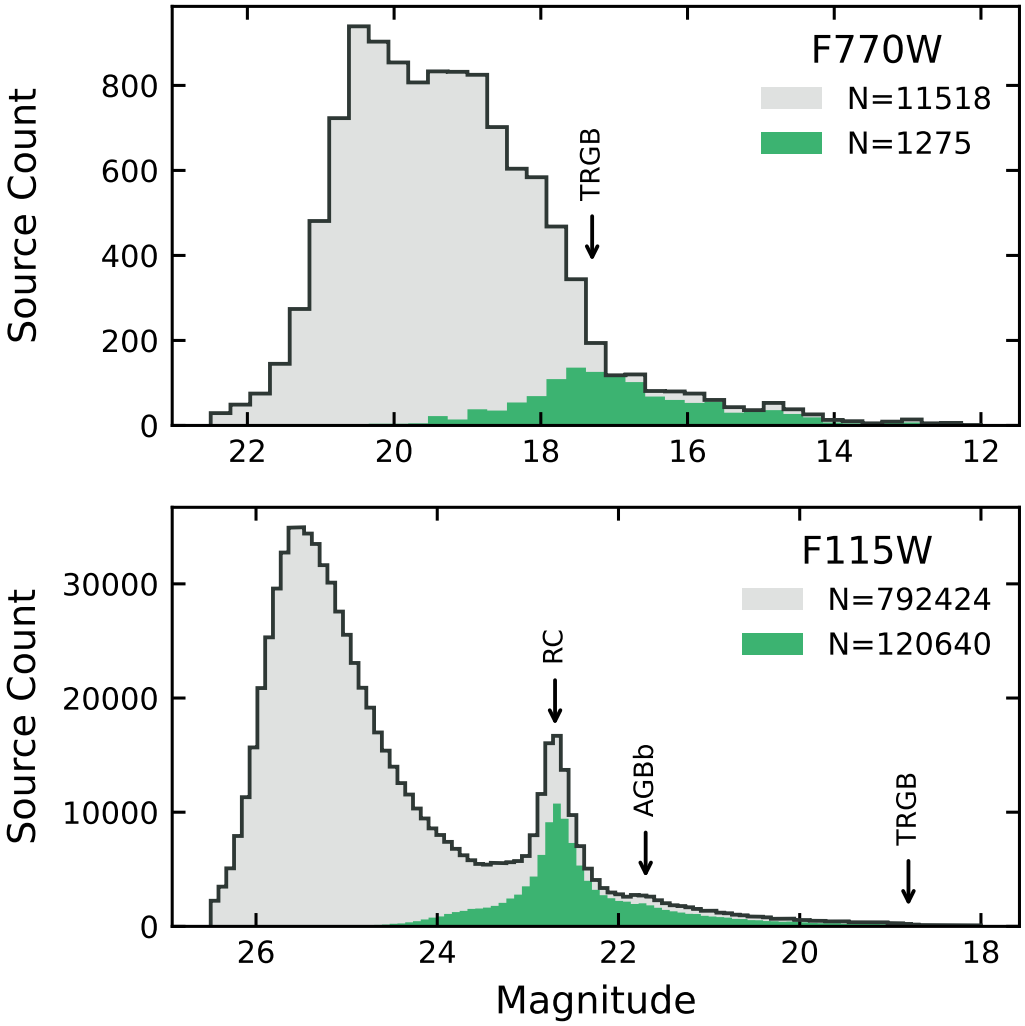

Figure 2.7 A comparison of source detection rate between the *JWST* data reduction pipeline (green) and the STARBUGII detection routine (grey) for a field in NGC 6822. The upper panel shows the routines applied to a MIRI F770W image, and the lower panel shows a NIRCam F115W image. Three evolutionary stages are marked where appropriate (RC, TRGB and AGBb). These are typically seen in deep high-quality images and discussed in Section 3.4.2.

2.3 Diffuse Emission Estimation

To obtain accurate photometry of a star, it is imperative to decouple the contribution from the dusty diffuse emission and the starlight to the total measured flux. The sky subtraction conducted in the aperture photometry routine provides an initial estimate for this by measuring the sky near the source. This technique is suitable for relatively flat backgrounds or those that vary smoothly across the entire image. However, in complex star-forming regions, the flux from the background dust has a high spatial variability and can be overpoweringly bright in the infrared, so a new method must be developed.

The background estimation routine in STARBUGII has two sequential steps: aperture masking (Section 2.3.1) and blending (Section 2.3.2) to effectively remove dust from an image. Figure 2.8 shows an example product of this routine, with the upper panel showing the raw image array and the lower panel showing the routine product, an estimation of the underlying dusty diffuse emission with all starlight contributed flux removed from the image.

2.3.1 Aperture Masking

The first stage of the background estimation routine is aperture masking. To remove the starlight from the image, this STARBUGII routine requires a list of point sources to mask. The completeness of this list is important, as stars that are excluded or undetected will be considered part of the diffuse emission.

The routine requires an initial estimate for source flux, which is conducted by the aperture photometry routine discussed in Section 2.2.5. Namely, a measurement for the rough ratio of source flux to local sky flux is (F_{src}/F_{sky}) for each source is input into Equation 2.11 to calculate R_{mask}, the size of the masking aperture radius. R_{mask} scales directly with this relative flux ratio, such that an isolated star on a dark flat background will require a larger masking aperture than an embedded star on a bright background, In doing so, STARBUGII can preserve as much information about the surrounding environment without losing information in the masking. Equation 2.11 includes the parameter σ which is the FWHM of the PSF being modelled, and two variables, (A) a uniform scaling applied to every source and (B) the profile slope, which models the potential non-linearity between source brightness and relative width on the image. Factors σ and A

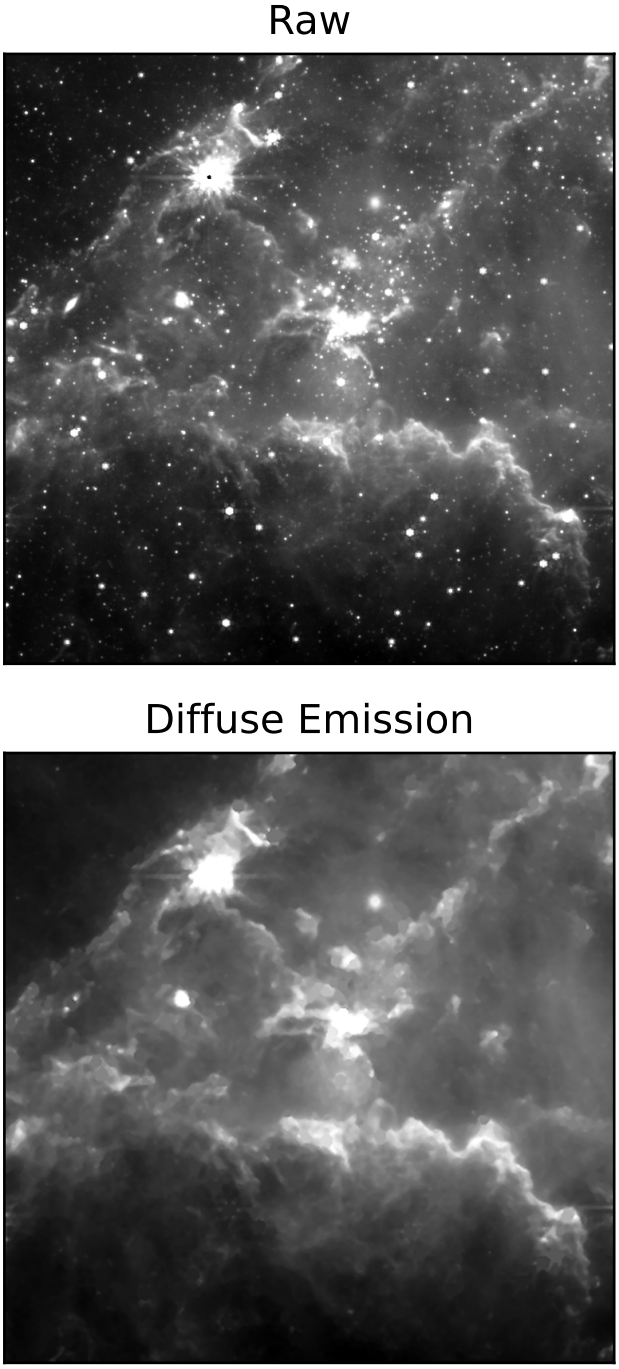

Figure 2.8 An example product of the Diffuse Background Estimation routine of STARBUGII. The left panel shows the raw image array, and the right shows an estimation of the underlying dust structure with the flux contribution from starlight removed.

have the same effect on the value of R_{mask}, but fixing σ usually results in a small variation around $A \sim 1.0$, leading to a more user-facing and understandable parameter

$$R_{mask} = A\sigma ln\left(\frac{F_{src}}{F_{sky}}\right)^{B} . \tag{2.11}$$

The lower panels of Figure 2.9 show the behaviour of R_{mask} against the flux ratio F_{src}/F_{sky} and how it varies with the scale factor A (left) and slope B (right). With careful alterations of these parameters, it is possible to construct a profile that effectively masks the central peak of a PSF. An example of this is seen in the upper panel, where a model PSF from *JWST* has been collapsed along one axis and added to a simulated sky noise against the number of FWHM from the PSF centre. The vertical dashed black lines show the boundary of the aperture mask with radius R_{mask}.

The aperture of radius R_{mask} is placed over the source and filled with a local sky estimate. This sky estimate is measured as the median pixel value inside a small sky annulus with radii $R_{sky} = (1.5R_{mask}, 1 + 1.5R_{mask})$. In doing so, the majority of the source flux is masked from the image and replaced with a representative value of nearby flux. This masked array is then passed into the following box blending step.

2.3.2 Box Blending

The raw image with masked apertures may be very noisy and lead to large photometric uncertainties if it is assumed to be a good measure of the diffuse emission by itself. STARBUGII passes the masked array into a blending routine to smooth out the noise from the array. This step in the routine uses the same PHOTUTILS Background2D function (Section 2.2.2) at its core and replicates the first half of the unsharp masking routine. As before, the function passes a box kernel across the image and fills the central pixel with the sigma-clipped median of all pixels under the kernel. In masking the apertures previously and filling them with a value representative of the local environment, STARBUGII can very effectively smooth the dust emission and produce a realistic model of the star-subtracted flux, as seen again in Figure 2.8.

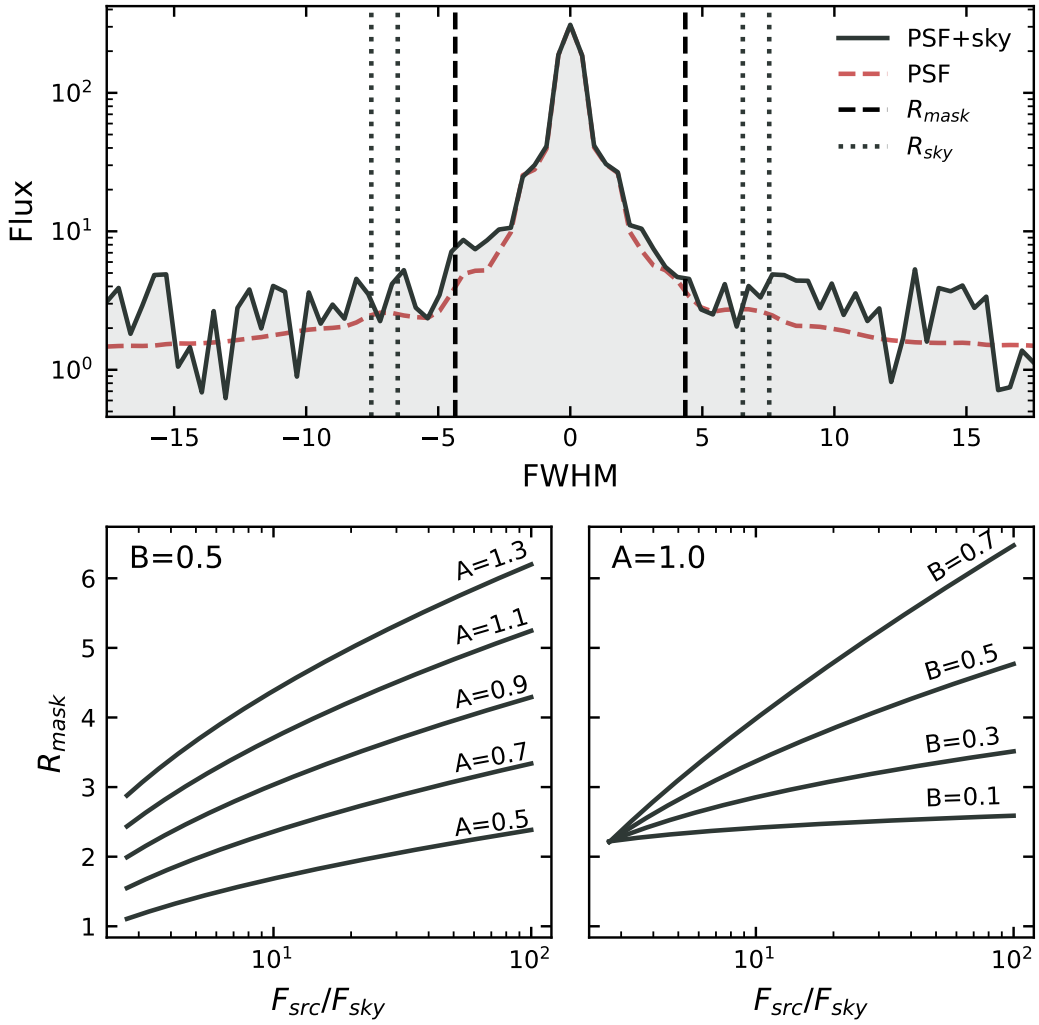

Figure 2.9 Modelling the width of a source PSF on an image array, by comparing the ratio of source flux to a local sky flux. The upper panel shows a source PSF collapsed into one dimension, on top of a simulated noisy sky. The vertical dashed line shows the size of the masking aperture, and the vertical dotted line shows the region from which the aperture fill value is measured. The lower panels show the scaling of the aperture mask radius with respect to the two parametrised variables, factor A (left) and slope B (right).

Changing the Background Resolution

Box blending the image allows any residual starlight or potential over-subtraction of the starlight to be smoothed out of the image. However, selecting the resolution of the blurred array will affect the final result. If the blurring kernel is small, the resulting array will precisely map the diffuse emission spatially, but it is significantly more affected by noise and residual starlight in the masked array. On the other hand, a large kernel will nullify the noise but lose the spatial accuracy, which in a complex environment may lead to larger uncertainties in the photometry.

Figure 2.10 shows the effect of altering the kernel size using the STARBUGII parameter BOX_SIZE.

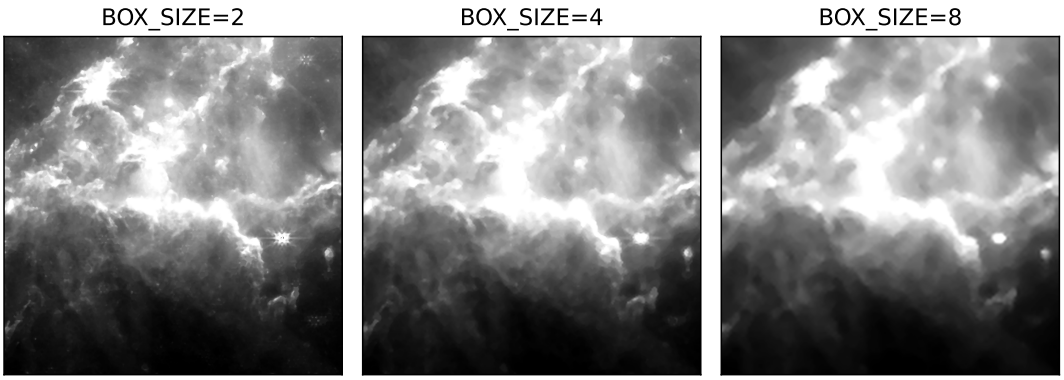

Figure 2.10 Output from the diffuse emission background estimation routine where the blending resolution has been decreased from 2–8 pixels.

2.3.3 Discussion on Performance

This STARBUGII routine has proven effective at isolating and characterising the diffuse emission to aid in the detection of embedded sources and measure accurate photometry, but there are several caveats to it performance.

The input source list

The quality of the source list provided to the routine is of primary importance. Only input sources are masked from the image, and an incomplete catalogue can result in stray starlight remaining in the background estimation, potentially leading to an overestimation of the background in the photometry. Care must be taken in the detection and selection of morphological parameters to provide the

routine with the best possible source list. Any extraneous flux in the image that is not associated with a point source list can be viewed as a positive. Background galaxies, bright dusty peaks and blended clustered stars that have been removed from the detection list will all be considered as background emission to STARBUGII. This allows for more accurate photometry as contaminating non-point-like sources are completely removed from the data array.

Saturation

Following on from a high-quality source list is the issue of saturated sources. No saturated stars are included in the high-quality source list. However, saturated stars present in the data contribute large amounts of flux. This emission must be taken into account when evaluating the image and its resulting photometry. It can be seen in Figure 2.8 that a large saturated region exists in the image in the upper left region. No point source has been detected in the centre of this region so no aperture masking has taken place. Furthermore, a circular aperture is largely inappropriate for covering such a region due to the elongated PSF fringes. Any diffuse emission estimation or photometry will always be noisy and uncertain in close proximity to saturation, but contaminating flux due to the PSF fringes can be easily removed with this routine, assuming no fringe peaks have been mistakenly detected as point-like sources.

Crowding

Finally, extreme crowding can cause problems with the diffuse emission routine due to the local sky estimation. The tight annulus around the masking aperture, inside which a measure for the underlying dusty emission is initially measured, may be contaminated by nearby stars. To minimise this effect, the annulus is placed as tight to the source as possible, without picking up the PSF edges, and the sigma-clipping will remove a large number of anomalously bright pixels from the measurement.

If the region of interest is extremely compact or blended, this routine will not miraculously remove the underlying flux underneath the point sources.

2.4 PSF Photometry

The PSF of a telescope is the shape which a point source exhibits on the detector. This shape is dependent on telescope optics and light path, the size of the aperture, the detector's pixel scale and the wavelength of the light. As such, every photometric filter on every telescope will have a unique signature PSF shape.

We can use this effect to our advantage by precisely modelling the shape and fitting it to each star in an image to gain highly accurate measurements of flux and position. During fitting, the central position (x,y) and total flux ($F_{\rm src}$) are varied until they match the source in question. By subtracting this modelled source from the image, you can overcome flux contamination from crowded overlapping FWHMs and gain precise astrometry from sources not centrally aligned on a pixel.

2.4.1 The Fitting Routine

At its core, STARBUGII uses the Photutils PSFPhotometry function to handle the pure fitting. For a given source detected on the image, a non-linear least squares fit is conducted to minimise Equation 2.12 for a set of free parameters θ, where D_i represents the pixel values from a cutout of the data around a source and $M(x_i, y_i, \theta)$ is the model pixel values for set θ at the x_i,y_i position on the PSF. This process is iterative as the routine incrementally works towards a minimum in parameter space. The set of parameters, θ, includes the central position of the PSF and source flux

$$f(\theta) = \sum_{i=1}^{n} \left[D_i - M(x_i, y_i; \theta)\right]^2 \ . \tag{2.12}$$

Nearby or overlapping sources can influence each other's fit for θ. In aperture photometry, this results in an uncontrolled over- or underestimation of source flux. PSF photometry provides the tools to negate this issue completely. By grouping these sources together and building a compound model for each source within the group, they can remain unbiased by each other. Equation 2.13 shows the compound fitting function, summing each source model M_j for parameter set

θ_j. The number of free parameters fit simultaneously is therefore proportional to the number of sources within the group

$$f(\theta) = \sum_{i=1}^{n} \left[D_i - \sum_{j=1}^{m} M_j(x_i, y_i; \theta_j) \right]^2 . \tag{2.13}$$

Source grouping works as a branching tree structure. From the central position of any source, another source within CRIT_SEP pixels is added to the group. This is repeated over all sources in the group until the group size stabilises. The value of CRIT_SEP needs to be chosen carefully; large groups of sources fit simultaneously have more accurate photometry, but fitting many free parameters is computationally expensive.

The minimised compound model is subtracted from the raw data, and the next grouped set of sources is fit. The full routine takes the form:

1. Nearby sets of sources are *grouped* together.
2. Data is cutout around the group to improve fitting speed.
3. A non-linear least squares *fit* is conducted to optimise parameter set θ
4. The compound model is *subtracted* from the data.
5. Repeat steps 1–4 for all sources in the image.

Residuals

With estimated flux contributions from both point sources and the diffuse background emission, subtracting these from the original raw input array will leave a residual. If these are both well estimated, the residual array will be mostly flat. Any sources that have not been detected before, perhaps due to their faintness or close proximity to another bright source that overpowered them, will be left in the residual.

Figure 2.11 shows the raw (left), background estimation (middle) and residual (right) for a small region on an image. Three sources are present in the data, but only the central source (cyan) has been detected due to the high detection threshold set. The flux from this source has been PSF fit and subtracted, leaving

a clean area in the residual image. The two undetected sources (green) are not fit but are highly contrasting in the residual image. This would allow them to be detected in the residual if a second iteration of photometry is conducted.

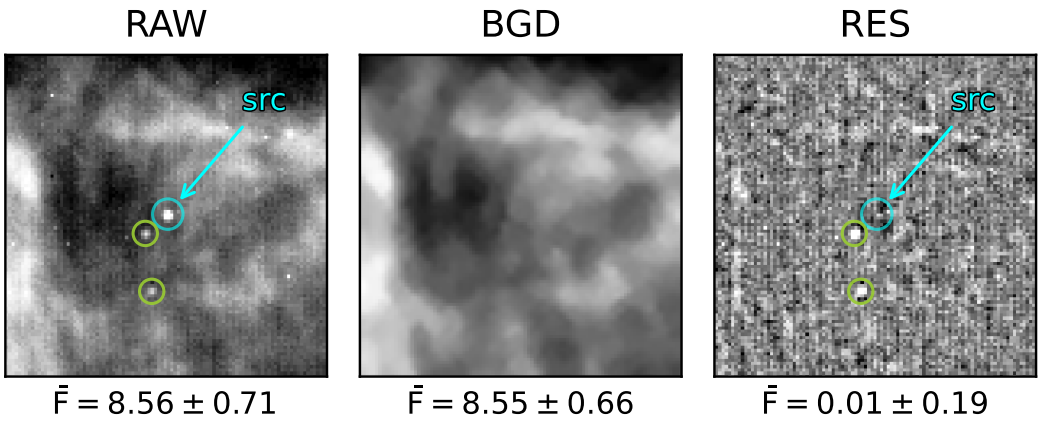

Figure 2.11 Three sources are present in the raw data array (left), with PSF fitting conducted on the central source (marked in cyan). The estimated background (middle) and fitted source flux are subtracted to produce the residual (right). The mean pixel flux is shown under each panel in MJy/sr units; the raw image has the highest, and the background estimation is expectedly slightly lower as no point sources are present. The residual image is close to zero but crucially positive, as the point sources present bring the average up.

2.4.2 WEBBPSF

Accurate modelling of the PSF is vital for all photometric outputs from a telescope. In preparation for the launch of *JWST*, a lot of resources went into this process, leading to the development of WEBBPSF (Perrin et al., 2012, 2014). This is designed as a flexible suite of optical simulation tools to model all the PSF shapes of every detector in every observing mode from *JWST*.

While a STARBUGII user can define their own PSF model to use for a given run of the routine using PSF_FILE, by default it simulates one with WEBBPSF. A separate 5″model is built for every submodule of each detector. That is, eight separate PSF models for each short wavelength NIRCam photometric band, two for long wavelength and one for MIRI. In total, this is 145 individual models for photometry on single-exposure images. Three examples of these can be seen in Figure 2.12, which shows the diversity of PSF shapes across the three detectors: NIRCam short, NIRCam long, and MIRI.

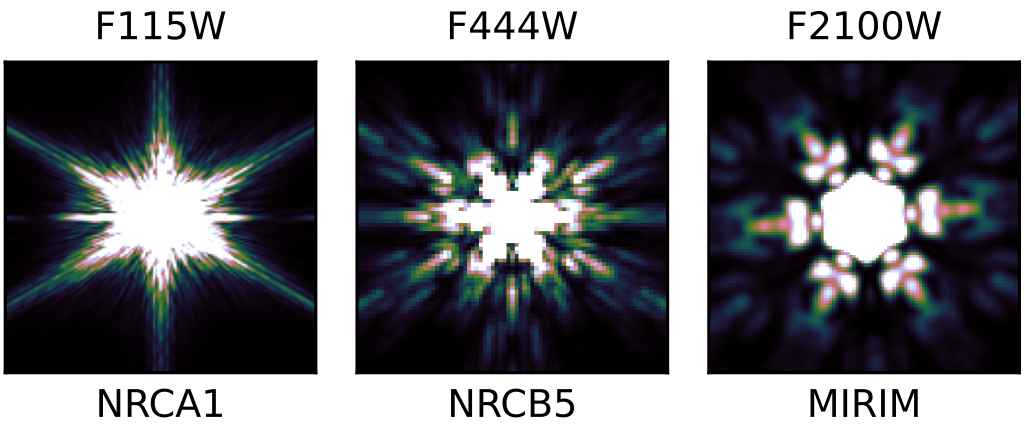

Figure 2.12 Three unique PSFs generated with WEBBPSF. Each photometric filter and detector module exhibits a subtly different scattering response.

2.4.3 Quality of fit

Uncertainties from the PSF fitting essentially measure how well characterisable the source is. This is done with a covariance matrix C from the Jacobian J of the model with respect to each parameter. The variance in flux is indexed from this matrix C_{ii} and the standard deviation quoted as $\sigma_f = \sqrt{C_{ii}}$

$$C = \sigma^2 (J^T J)^{-1} \,. \tag{2.14}$$

Wandering Stars

STARBUGII introduces the idea of a *maximum wander*. This measures the offset between the initial position and the fit position. The fitting may struggle to lock onto the central position of a source that is not PSF-like. This could be a spurious detection of a dusty peak that has happened to pass the morphological criteria in Section 2.2.4. STARBUGII identifies sources that have wandered more than MAX_XYDEV from their original position and flags them. This is primarily a measure of the poorness of the source quality, and they can usually be discarded; however, STARBUGII will force photometry on them regardless.

Forced Photometry

Fitting the source position as well as the flux improves both the photometry and the astrometry. However, it is computationally expensive. Forced photometry is the act of fixing the position and only fitting for the source flux. In doing so, less accurate measurements of flux are gained at a much faster rate. By setting FORCE_POS=1, STARBUGII will conduct forced PSF photometry. As the fit quality of these sources is generally lower, STARBUGII flags them in the output.

Saturation

The PSF routine in STARBUGII is also able to recover flux from saturated stars, but this has to be done deliberately and with care. By using a very large model PSF (significantly larger than the default 5″), the fitting routine can analyse the strength of the source PSF fringes rather than the central peak height. The source position needs to be forced, and the routine run on individual sources.

2.4.4 Photometric corrections

JWST images are calibrated into MJysr^{-1} with the PHOTOM CRDS files. As calibrations of these references improve, they are fed back into the PSF scaling in STARBUGII. It uses up-to-date PHOTOM references with the pixel scale of each detector array to convert the image into Jy units and output flux measurements in Jy. Fluxes are converted into the AB magnitude system with the flux zero point 3631Jy, alternatively, a custom zero point magnitude (ZP_MAG) can be included as a parameter to convert and apply an instrument-specific offset. STARBUGII can convert to the Vega system using the most up-to-date calibrations for "AB to Vega offsets" in the CRDS files.

2.5 Catalogue Matching

All the routines discussed so far act on a single image at a time. Whether this involves a single exposure, a large-scale multi-band program, or is internal to the routines (for instance, source detection in Section 2.2), cross-matching point source catalogues is a vital step in data reduction.

Built into STARBUGII are several user-facing matching routines, enabling flexib-

ility in approach (depending on the science goal) while drawing from a set of generalised functions.

2.5.1 Generic Matching

The primary matching routine that is used most often in any internal function or any data processing is "GENERIC" match. This uses a nearest neighbours approach to locate, if available, the source in a catalogue that matches most closely the sky position of a source in another catalogue.

This can be done with pixel coordinates in the case of the detection routine, where the catalogues being matched have been produced from the exact same image. However, in higher-level data products, it is usually done with right ascension and declination coordinates at slightly different dither positions. By taking a source in the "base" catalogue A, and computing the magnitude of separation (in the chosen coordinate system) to every source in a second catalogue B, a distribution of separations is built. By sorting this distribution into size order and identifying all sources which have a separation less than a maximum threshold (MATCH_THRESH), a subset of viable matches is identified. This process is repeated for every source in A.

Now we investigate all the subsets of valid matches. For a given subset A_i, the first source B_j is the closest match. Every other subset is searched for B_j to see if it is a valid match elsewhere. In the case where no other valid matches of B_j are found, an entry is made in the resulting catalogue Y with source $A_i + B_j$. If B_j is a valid match to a number of sources in A, we assess which of these matches is best. In this generic base algorithm, it is simply, if A_i and B_j have the closest separation, we consider this the match and add that entry to Y. If it is not the nearest, and B_j matches better with another source in A, A_i does not get a match in B. After all subsets are compared, any remaining sources in B which have not been matched are appended to the end of Y.

It is often necessary to match several catalogues simultaneously, for example, by combining a large number of single exposures that have been dithered. In this case, each new catalogue queued for matching is sequentially compared to the result of the last match. That is, combining $A + B = Y$ and then $Y + C = Z$. As each new catalogue is matched to the base catalogue, all positions associated with each source are averaged with a nan-masked median. In doing so, the central

position of each source is refined with every subsequent match. The resulting catalogue will take the form seen in Table 2.1.

A
A_1
A_2

Input 1

+

B
B_1
B_2

Input 2

+

C
C_1
C_2

Input 3

=

A	B	C
A_1	B_1	C_1
A_2	–	–
–	B_2	C_2

Output

Table 2.1 A framework of output from GENERIC matching. Three tables (A, B, C) have been combined, each containing two unique sources $(_{1,2,3})$. The first source in each table are positively matched together. A_2 is unique and not present in B and C. Sources B_2 and C_2 are matched together and the end of the table.

Adjusting the value of the separation threshold (MATCH_THRESH) can affect the quality of the output catalogue. If the value is high, exceeding the associated uncertainty in the position of each source, it can result in a large number of mismatches, where unrelated sources that exist in close proximity can be mistakenly matched together. Conversely, setting this value too low, below the associated position uncertainty, can result in legitimate matches between the catalogues not occurring, due to them being on the opposite extreme ends of the error around a central position. Fortunately, an appropriate value for the threshold can be derived from the data itself. Figure 2.13 shows the distribution of matched source separations when setting the threshold arbitrarily high. Two separate populations are visible in this distribution. The first peaks sharply at zero, where positively matched sources appear at similar positions in the two catalogues. The second is a broad population centred at ~ 0.5, where high numbers of mismatches begin to occur. Between these two populations, the distribution drops to zero. By finding the point of intersection between these distinct populations in the distribution, the matching threshold can be set to maximise the number of positive matches while minimising the mismatches.

2.5.2 Cascade Matching

While GENERIC matching offers a simple routine to crossmatch several catalogues simultaneously, it can lead to large, sparsely populated tables in the case where large numbers of catalogues with minimal crossover are combined. This situation may arise if photometry has been conducted on many individual dithers across

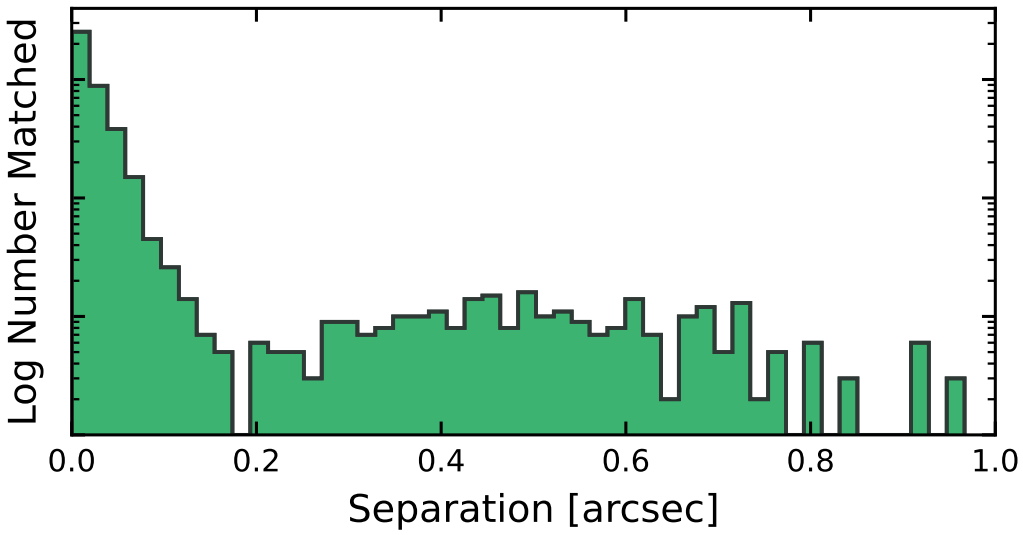

Figure 2.13 The distribution of the magnitude of separation between matched sources in two catalogues. Two distinct populations are visible in the distribution: a low-separation peak of positively matched sources and a broader group of mismatches around a larger mean separation.

a large multi-tile mosaicing program, and each exposure gets a new column (or set of columns) in the final table, quickly bloating its size. Mosaic tiles may overlap at the edges for data continuity, but the percentage overlap may be only a few percent. To reduce the memory and data storage load of large programs, STARBUGII has an augmented version of GENERIC matching called CASCADE matching.

CASCADE matching is used when the order of input catalogues does not need to be preserved. In other words, it is not important if, for example, the flux, from the n^{th} exposure, appears in the n^{th} column in the table; all that is required is the overall list of flux values associated with that source. This is ideal for data obtained within the same photometric band across a large series of mosaicing exposures.

This matching routine simply "left justifies" all values in between each new sequential match to a new table, moving them into the leftmost available space. That is, if there are two entries, and only the second one has a value, the routine moves the second value into the first column and deletes the second column. In doing so, the table becomes half the overall size and large amounts of memory are saved during the computation. Table 2.2 shows an example output of this routine.

A	B	C
A_1	B_1	-
-	B_2	C_1
A_2	-	C_2

Input

$\longrightarrow$

A	B
A_1	B_1
B_2	C_1
A_2	C_2

Output

Table 2.2 The framework of the CASCADE matching routine. The values from three columns get "left justified", by moving to the leftmost available column. In doing so, the size of the table can be shrunk. The input table is sparsely distributed with missing values, the output table is condensed.

2.5.3 BAND MATCHING

One major issue involved in *JWST* imaging programs arises from the large wavelength baseline of the telescope. Spanning more than 25μm, the FWHM of the longest wavelength PSF is two orders of magnitude broader than the shortest wavelength. An additional problem is that the NIRCam and MIRI instruments trace stellar populations which differ substantially in their stellar density. As such, the shorter wavelength images are often more abundant in faint blue stars with very narrow PSFs. Conversely, the longer NIRCam and MIRI data traces further down the Rayleigh-Jeans tail of the black body emission, where stars are typically fainter or less commonly bright, and where they may exhibit an infrared excess due to dust. In the most extreme cases, these very red objects might not have an optical or near-IR match due to extinction. Consequently, severe blending may occur when attempting to cross-match stars from long-wavelength catalogues to short-wavelength catalogues, where multiple sources may exist within the long PSF.

STARBUGII uses a modified "boot-strapping" method to crossmatch catalogues built from different photometric bands. Due to the increasing PSF size with respect to increasing wavelengths, the shortest-wavelength photometric catalogues have the smallest uncertainties in astrometric measurements. A list of input catalogues is first sorted in order of increasing photometric wavelength and crossmatched sequentially. So catalogue A+$B \rightarrow AB$, and then AB+$C \rightarrow ABC$. A source in C that was not present in AB will be appended to the bottom, as seen in GENERIC matching above. Crucially, all position RA/DEC values used for any source are taken from the shortest wavelength (most astrometrically accurate) catalogue in which it was resolved. In doing so, uncertainty is not compounded, and highly accurate positions can be given for longer wavelength detections.

A
A_1
A_2

$+$

B
B_1
B_2

$\longrightarrow$

A	B
A_1	B_1
A_2	$-$
$-$	B_2

$+$

C
C_1
C_2

$=$

A	B	C
A_1	B_1	C_1
A_2	$-$	$-$
$-$	B_2	C_2

Table 2.3 The framework of the BAND matching routine. Catalogues are boot-strapped from shortest to longest photometric wavelength. At each stage, only the position (RA/DEC) from the shortest available wavelength is used.

2.5.4 Exact Value Matching

STARBUGII marks each source in a source list with an identifying CATALOGUE NUMBER. This can be used to match between catalogues that have been modified and worked on for scientific analysis, and matched back together. This is done by the STARBUGII EXACT VALUE matching routine, which simply scans a column in one catalogue for an exact match in a column of a second catalogue. If the scanned column is CATALOGUE_NUMBER, the sources can be easily identified, and all values associated with that source between the matched catalogues will be combined.

2.6 Artificial Star Testing

It is difficult to validate the performance of both the source detection and the accuracy of photometric measurements, without any known truths. We can, however, produce simulated data with known source properties and attempt to recover these with the photometry routines. This is the underlying principle of ARTIFICIAL STAR TESTING (AST). By simulating stars inside an image, we can understand the limits of detection depth and constrain the uncertainties in photometric measurements.

A single AST follows the following structure:

1. Simulate a number of stars (N_s), drawn from some distribution or a specified input catalogue.
2. "Inject" these stars into an image.
3. Proceed to run source detection and photometry on the image.
4. Construct a table of results flagging whether the injected source was

detected and if so, what its measured flux was.

5. Repeat steps 1-4 N_T times, until enough of the input parameter space has been covered.

The result will take the form of Table 2.4. A large list of sources will have initial input parameters x_0, y_0, and f_0, their associated measured values $x_{\rm det}$, $y_{\rm det}$ and $f_{\rm det}$ as well as the status of their successful recovery (1) or otherwise (0).

x_0	y_0	f_0	$x_{\rm det}$	$y_{\rm det}$	$f_{\rm det}$	status
1.0	1.0	10	1.0	0.9	10.1	1
2.0	2.0	9.0	-	-	-	0

Table 2.4 Primary output from the artificial star tests. Three input parameters x_0,y_0 and f_0 are given, and the values measured by the pipeline are given as $x_{\rm det}$, $y_{\rm det}$ and $f_{\rm det}$. The final column "status" flags whether they have been detected by the routine. Two sources are shown here, the first has been detected, and the second has not.

2.6.1 Source Injection

To simulate a single star, we start from a normalised PSF. This PSF must be appropriate for the detector, either empirically measured or simulated. When conducting AST on *JWST* images, we can again employ WEBBPSF, simulated for the submodule of each detector, as described in Section 2.4.2. Assuming the injected stars are being procedurally generated, initial positions and magnitudes are drawn from a linear distribution. To save computational resources, the limits of position are drawn 1 FWHM from each detector edge. Similarly, initial brightness is drawn from a flat distribution of magnitudes rather than fluxes. Sampling from non-linear fluxes leads to an over-modelling of bright stars and requires more computational resources to fill parameter space. The sampled magnitudes are simply converted back to the appropriate flux unit for the input image.

The normalised PSF is multiplied by the flux and added to the raw image array. If the position is misaligned from the centre of a pixel, the PSF has to be resampled to align with the pixels.

The number of injected stars N_s must be considered carefully. To appropriately cover the input parameter space, there will inevitably be a large total number of stars tested. This is especially true if the fraction of stars detected is to be

measured spatially across the whole image. In selecting a small number for N_s, many individual tests will need to be conducted to reach the desired number, which proportionally scales the computational expense. However, injecting too many stars in a single test will increase the overall flux in the image and issues involving crowding may begin to take effect, causing greater uncertainty in flux measurements and artificially lower detection rates. The ballpark number of 10% of the total number of stars detected in the raw image is commonly used.

2.6.2 Detection Limits

After the pipeline conducts source detection on the image, the output source list is matched to the list of injected stars. Injected sources within MATCH_THRESH arcseconds of a detected source is marked as having been successfully recovered (status=1), else it has failed (status=0).

The initial injected magnitude of all artificial stars is binned, and the fraction of positive detections to the total injections is measured for all sources within each bin. The resulting "*recovery fraction*" can be seen in Figure 2.14. The black points represent the recovery fraction at the centre of each binned magnitude. It is clear that above a threshold magnitude, the detection rate is level but drops quickly thereafter. This profile can be modelled with the logistic function in Equation 2.15

$$f(x) = \frac{l}{1 + e^{-k(x-x_0)}}\,, \tag{2.15}$$

where l (the upper limit), x_0 (the turning point) and k (the slope steepness) are all freely fit. This profile is overlaid in green. By parametrising the profile, values for 50, 70 and 90% completeness limits can be derived.

Spatial Completeness

Along with photometric depth, the recovery fraction can be used to measure the completeness spatially across the image. In regions of high crowding or complex backgrounds, it would be expected that the completeness depth is brighter, due to the challenging conditions. By binning the initial injection positions and measuring the recovery fraction within these, a spatial map of completeness can be constructed. The size of the bins would vary on the level of information required and the limits of computation time, as filling the spatial bins to a sufficient level

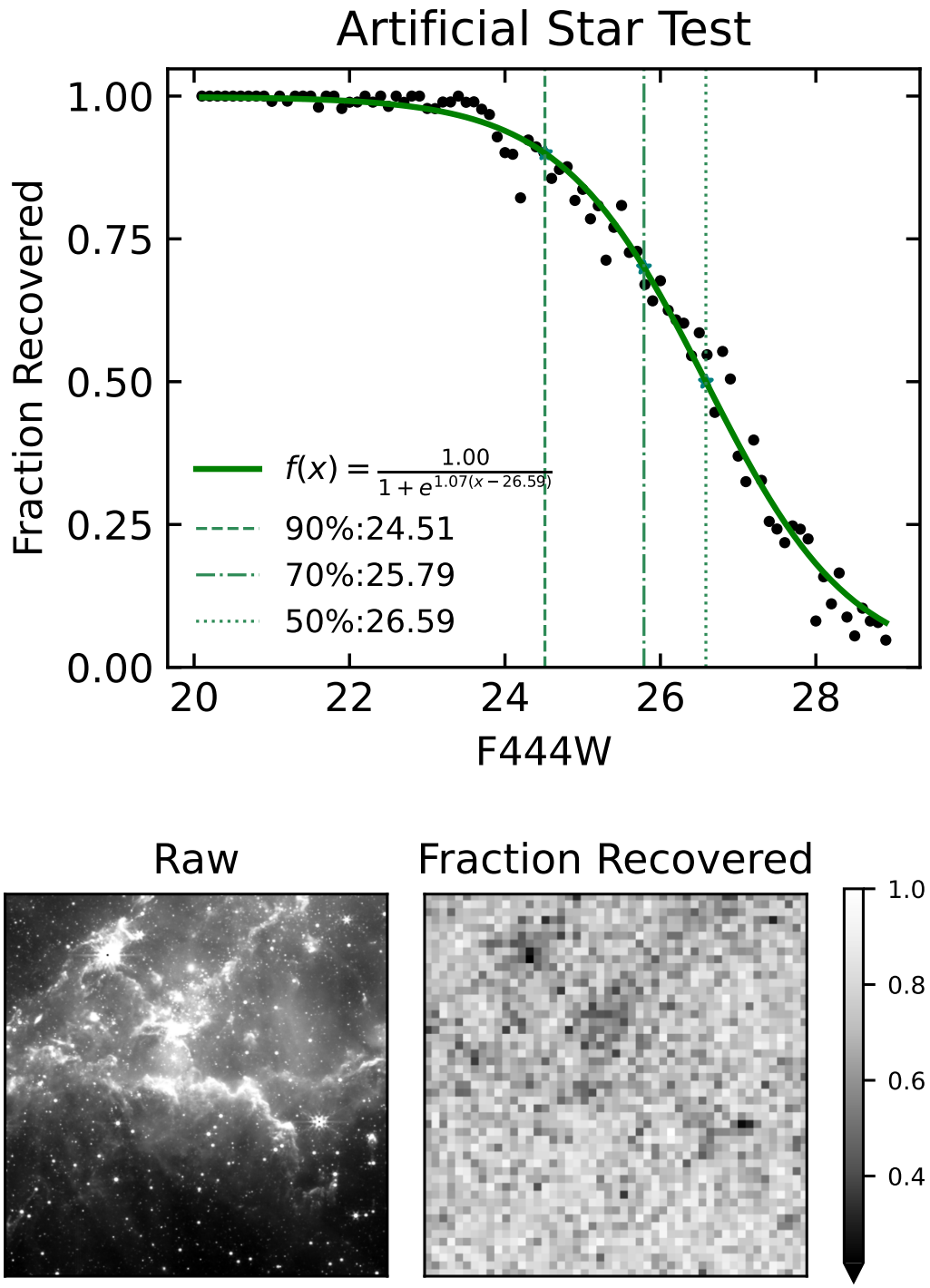

Figure 2.14 AST outputs, the upper panel shows the recovery fractions as measured by AST. Black points are the detected fraction as a function of binned input magnitude. Overlaid is a logistic function fitting this profile. The lower panels show the result of measuring the completeness limit spatially across the image. The lower left panel shows the raw image, and the lower right panel shows the fraction of detection within spatial bins.

that the results are accurate is very expensive and time-consuming.

Figure 2.14 shows how the fraction of detection would vary across the image. The recovery fraction has been calculated in pixel bins of width 20 pixels, but the resolution can be increased for a more fine-tuned understanding of the effect of crowding and dust emissions on the photometry, or reduced in images that vary over much larger areas.

2.6.3 Photometric Uncertainty

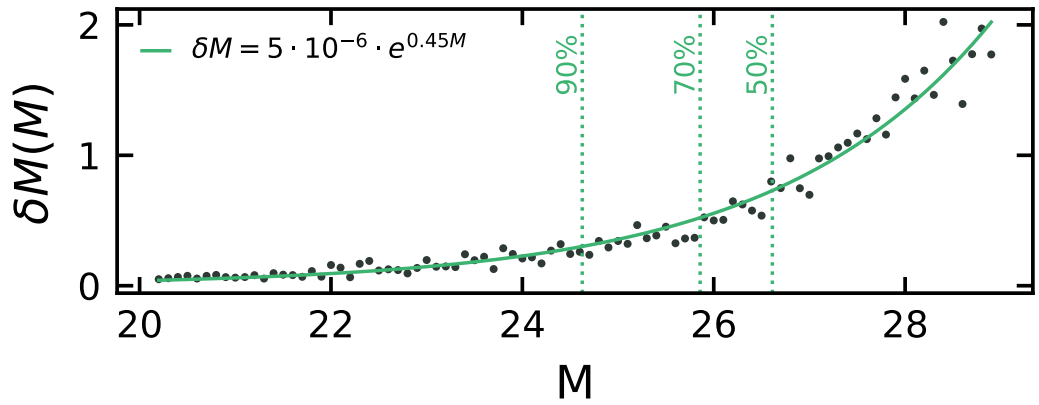

Figure 2.15 Calculating the error in the photometry using artificial star testing. Black points show the error in magnitude in magnitude bins, overlain by green line models this in the form: $\delta M = Ae^{BM}$.

Photometric errors can be constructed from observed pixel values as in aperture photometry discussed in Section 2.2.5 or by deriving them from the quality of fit of PSF photometry in Section 2.4.1. However, both measures are theoretical and do not account for the inner workings of the pipeline, such as how well it deals with crowding or bad pixels. To best understand the photometric uncertainties in STARBUGII, we can compare the initial flux for each source to the measured flux. In STARBUGII this is done by binning the artificial stars by input magnitude and finding the standard deviation of the input magnitude versus measured magnitude, see Equation 2.16. The values can easily be translated back to fluxes as discussed in Section 2.4

$$\delta M(M) = \sqrt{\frac{\sum^{n}(M_0 - M_{\rm det})^2}{n-1}}\,. \tag{2.16}$$

2.6.4 Optimisation

Artificial star testing is notoriously computationally expensive. To adequately cover the input parameter space and fit a well-constrained logistic function to the results can require millions of artificially-injected sources. If this is being applied across large mosaics to map the completeness level spatially, or across large numbers of photometric bands, it can quickly add up to weeks of computation time. To reduce the overheads of gaining well-constrained completeness estimates, STARBUGII uses a number of optimising measures.

Parallelisation

One simple optimisation is parallelisation. Each test is independent from the others and therefore can easily be split into parallel processes. STARBUGII divides the catalogue of input parameters to the artificial stars and passes each division to a number (N_P) of subprocesses. Each of these processes executes N_T/N_P tests, taking N_S sources from the supplied catalogue per test until it has finished processing all the input sources. The results from each subprocess are passed back to the main process and are simply appended into one master catalogue to be compiled into the completeness estimation results described above.

Assuming enough memory is available on the system running the parallelised AST, the total time for the test is reduced to a fraction of the time, as the overheads of splitting the tests are negligible.

Built into the routine is a safety measure to recover killed processes. On shared resource cluster computers, where variable demand may make the execution speed unpredictable or the user does not have the privilege to prioritise their own requests, it might arise that a subprocess dies or hangs, causing the AST to pause indefinitely. This could result in many days' worth of computing being lost. So STARBUGII periodically exports to file the current state of each subprocess, which at any point can be recovered and compiled into the final product. In doing so, nothing is lost if the AST gets stopped or killed halfway.

SubImages

The quantity of data processing of an image by the STARBUGII routines is proportional to the size of the image. Any process inside a routine that needs to examine every pixel (like a simple median) scales with the image area. Therefore, running an AST repeatedly over a large image will increase the required time.

However, the image can easily be split up into "sub-images" and processed in smaller chunks. By randomly cutting a smaller region from the full raw image, a single AST can be conducted at a much faster pace. As long as the position of the subimage is kept, the input x_0 and y_0 can be transformed back to the global coordinate system and photometric depths and spatial completeness can still be calculated.

One caveat is that the subimage cannot be too small, otherwise flux from injected stars is lost over the edge of the cutout, and the flux recovery is not 100%.

Routine Selection

The final optimisation comes in the form of routine selection. By default, the AST routine will run source detection, aperture photometry, diffuse emission estimation and then PSF photometry. However, any one of these routines can be toggled on or off. If the primary goal of an AST run is to determine the detection limit, there is no reason to spend large amounts of resources on the computationally expensive PSF photometry. Therefore, simply turning off all unnecessary routines will reduce the required processing time drastically.

2.6.5 Using AST to forecast Pipeline Performance

With the optimisation steps, the AST routine in STARBUGII is fast. On the order of thousands of artificial stars can be tested on a single NIRCam exposure in one or two minutes. While this is an insufficient number to fully explore the input parameter space and measure precise photometric uncertainties, it is more than enough to gauge the rough performance of STARBUGII on that image. With this in mind, during the many steps in photometric processing where detailed fine-tuning of parameters such as SHARPNESS or SIG_SKY has to be iteratively decided upon, AST can be used to forecast the expected overall effect of those decisions. Supplying the parameter file to STARBUGII AST and running a small test will allow a user to quantitatively understand exactly how setting a specific parameter will affect the overall results, without needing to run every routine over a large number of images.

2.7 Application of StarbugII in *JWST* programs

During the final stages of *JWST*'s commissioning period, our first GTO (1227) images were taken with NIRCam of the star-forming region in the SMC, NGC 346 (Jones et al., 2023a), seen in Figure 2.17. It was on this data that STARBUGII received its first real data testing. At this point, the in-flight PSFs and PHOTOM references had not been well calibrated, and the astrometric distortion across the chips was not well understood. Leading the photometric processing, I set STARBUGII to work on this initial *JWST* data, resulting in the publication of the first *JWST* CMD in Jones et al. (2023a), seen in the left panel of Figure 2.16. For this publication in Nature Astronomy, I was the second author, acknowledging my substantial scientific contribution. I conducted the photometric processing with purely aperture photometry of the NGC 346 star-forming region. For this, I used the individual exposures of F115W, F187N, F200W, F277W, F335M and F444W, rather than the mosaics, due to astrometric alignment issues in the *JWST* reduction pipeline. Even with these limitations, we published the first NIRCam two-colour CMDs (F115W–F200W vs. F200W and F115W–F444W vs. F444W) and four-colour CCD (F115W–F187N vs. F200W–F444W). The source catalogue reached 10 magnitudes below the *Spitzer* SAGE faint source limit at 3.6μm and 4.5μm for the region. This uncovered a significant population of dust-embedded YSOs and subsolar-mass pre-main-sequence stars. Additionally, many of the dusty YSOs exhibited H_α excess emission associated with ongoing accretion. The existence of emission from both dust and accretion revealed for the first time the possibility of rocky planet formation in a low metallicity environment. This result has later been confirmed by NIRSpec MOS data (De Marchi et al., 2024), who shows accretion disks around solar mass stars appear to last longer when the metallicity is low.

As part of the same *JWST* GTO program, we revisited the same region with F770W, F1000W, F1130W, F1500W and F2100W MIRI filters, seen in Figure 2.18. This data was obtained months after the NIRCam images published in Jones et al. (2023a). Due to improvements in the NIRCam flux calibrations and PSF models, I helped to conduct full PSF photometry on the NIRCam data. The marked improvement in depth and precision of the NIRCam PSF photometry can be seen in the right panel of Figure 2.16, adapted from Habel et al. (2024). Unfortunately, at this stage, the MIRI fluxes, flat fields and PSFs were still poorly

calibrated, so as with the earlier NIRCam data, I aided in the production of an aperture photometry catalogue with the MIRI view. Combining the NIRCam PSF and MIRI aperture photometry data to construct an eleven-band matched catalogue, we could perform accurate SED fitting for the detected YSOs. Habel et al. (2024) finds a close association between the positions of the YSOs and filamentary structure bright in the infrared, which is seen in the Figure 2.6, where YSO candidates of increasing confidence (calculated using colour-cuts) are shown in blue, magenta and red, overlaid on a MIRI image of the region. A total of 196 YSOs were detected, including 23 classified as high confidence. The fitted SED models estimate the objects' temperatures, luminosities, and masses, showing that the YSOs in the sample approach $1M_{\odot}$, the lowest mass of extragalactic YSOs detected to date.

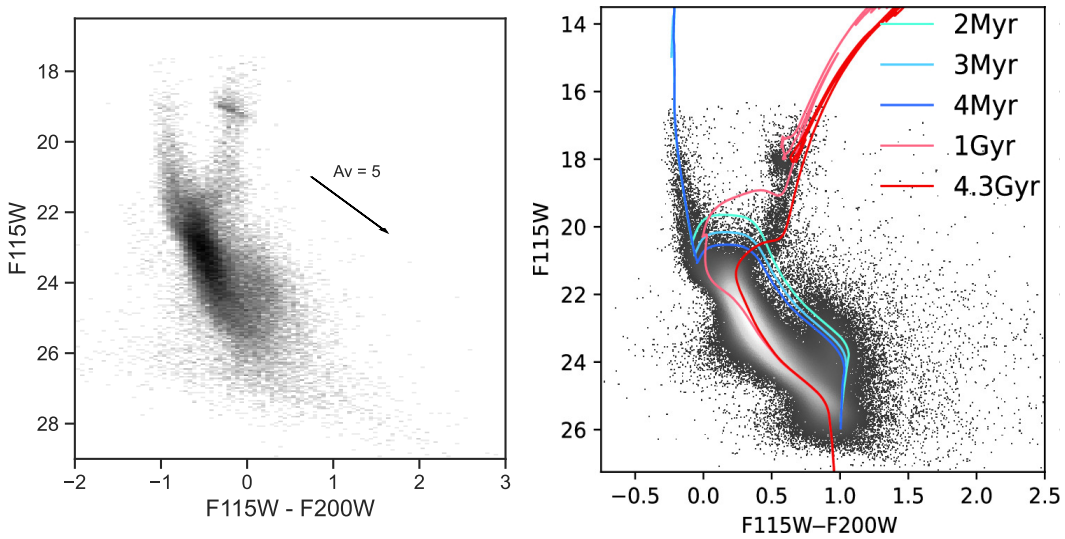

Figure 2.16 CMDs F115W–F200W vs. F200W from Jones et al. (2023a) (left), using the first round of aperture photometry and Habel et al. (2024) (right) using PSF photometry with updated flux calibrations to the *JWST* pipeline.

We continued the YSO studies in the LMC's N79 region (see Figures 2.19 and 2.20) with Nayak et al. (2024a,b). By now, the MIRI PSF models have been fully modelled, allowing me to conduct the first PSF photometric catalogue from MIRI. In total, over 100 YSOs were identified with SED fitting. Five massive objects were centrally located in a super star cluster, which was found to have likely formed through collisions of dust filaments, and the ensuing winds and radiation triggered the rest. Clean detection in this region proved to be the most challenging yet and led directly to the development of the SMOOTHNESS parameter due to the dominant bright dust features and faint embedded sources therein. The detection of these objects confirmed N79 to host a super star cluster, with high

YSO mass accretion ($\sim 0.02 M_{\odot} yr^{-1}$) and turbulent bow shocks and whirlpools.

Pushing *JWST* resolved stellar analysis towards its distance limit, Hirschauer et al. (2024) used STARBUGII to provide PSF photometry for the extremely metal poor ($\sim 3\% Z_{\odot}$) distant (18.2 Mpc) dwarf galaxy 1Zw18, seen in Figure 2.21. Despite the compact nature, localised sites of young upper main sequence and red supergiants were identified, as well as a broader distribution of more evolved AGB and RGB stars.

STARBUGII is easily installed via pip and fully documented on readthedocs, it is now also listed on the official *JWST* community tools page. Due to its effectiveness and simplicity, STARBUGII has been picked up by the wider astronomical community and used to conduct photometry in challenging fields. For example, while observing the low metallicity star cluster NGC 602, in the SMC, Zeidler et al. (2024) utilised STARBUGII to detect the first ever extragalactic brown dwarf stars. They identified 64 candidate brown dwarfs in the region shown in Figure 2.1, which will be key to refining the understanding of the subsolar mass function at very low metallicities and young ages. STARBUGII was vital to this science, as it enabled the *JWST* faint detection limits to be pushed to the lowest mass objects seen outside our galaxy.

2.8 Summary

This Chapter details the underlying routines of STARBUGII, a PSF photometry suite designed to detect dust-embedded sources in complex and crowded regions seen with *JWST*. As outlined, STARBUGII has proven successful in measuring the stellar populations of challenging fields in NGC 346, N79, and 1Zw18. In the following Chapters 3 and 4, I will focus on the properties of the stellar populations of the Local Group galaxy, NGC 6822 (seen in Figures 2.22 and 2.23), in which I published (Nally et al., 2024) in conjunction with (Lenkić et al., 2024) and have (Nally in prep.) to be submitted.

Figure 2.17 NGC 346 NIRCam NASA, ESA, CSA, STScI, O. Jones, M. Meixner

Figure 2.18 NGC 346 MIRI Credit: NASA, ESA, CSA, STScI, N. Habel, M. Meixner

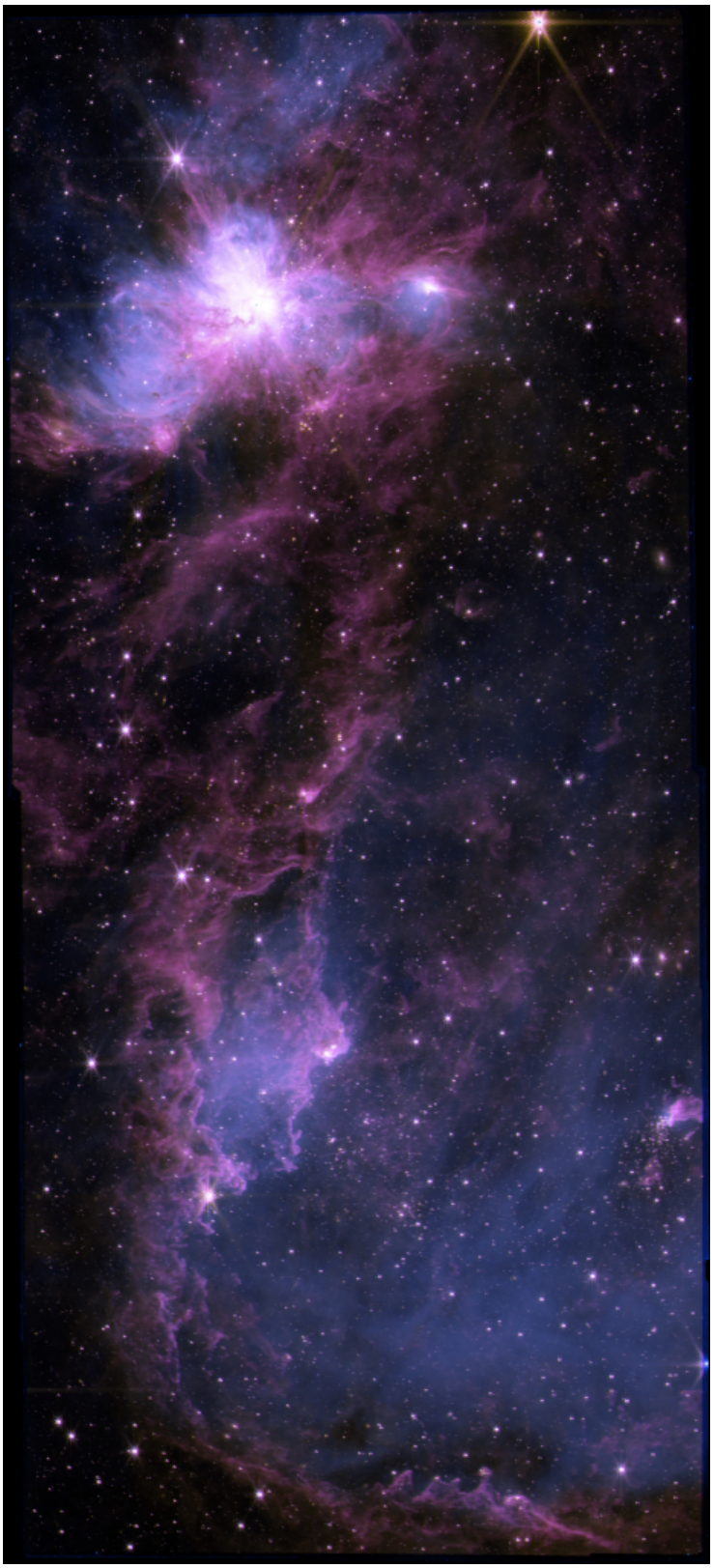

Figure 2.19 N79 NIRCam Credit: NSF, AUI, NSF NRAO S. Dagnello, M. Meixner

Figure 2.20 N79 MIRI ESA/Webb, NASA, CSA, O. Nayak, M. Meixner

Figure 2.21 1Zw18 NIRCam + MIRI ESA/Webb, NASA, CSA, A. Hirschauer, M. Meixner et al.

Figure 2.22 NGC 6822 NIRCam ESA/Webb, NASA, CSA, C. Nally, M. Meixner

Figure 2.23 NGC 6822 MIRI ESA/Webb, NASA, CSA, L. Lenkić, M. Meixner

3 NGC 6822 *JWST* Stellar Populations

With a 6-inch Equatorial it was very difficult to see.

— Edward Barnard

3.1 Introduction

This Chapter presents an overview of the NGC 6822 *JWST* imaging program, including the observation details, data reduction, and the photometric extraction with STARBUGII. Combined NIRCam and MIRI CMDs are constructed and used to identify their various stellar populations, with a focus on the evolved stars. Section 3.2 presents the observational strategy in detail. Although I was not heavily involved in planning the observation strategy, the description is provided here for completeness, offering context for the data reduction and photometry described in Section 3.3. In Section 3.4, I present and discuss the resulting images, stellar classifications, and luminosity functions. Finally, I summarise the results in Section 3.5.

3.2 Observation Strategy

The central bar of the galaxy NGC 6822 (adopted properties given in Table 3.1) was imaged with *JWST* (Program ID: 1234; PI: M. Meixner), utilising both the NIRCam and MIRI. In total, 19.92 hours of integration time was split between NIRCam (~4.80 hours) and MIRI (~15.12 hours). The spatial coverage for the

Table 3.1 Summary of NGC 6822 properties and survey details.

Properties of NGC 6822	
Nominal centre point	19:44:56 -14:47:51
Distance	490 ± 40 kpc (Mateo, 1998)
Distance modulus	23.45
E(B-V)	0.35 ± 0.04 (Tantalo et al., 2022)
Metallicity	[Fe/H]= −1.2 (Lee et al., 2006)

two instruments is illustrated in Figure 3.1. The field-of-view (FoV) of both instruments includes the newly-discovered young, massive, embedded super star cluster (SSC) candidate region Spitzer I (e.g., Jones et al., 2019; Hirschauer et al., 2020; Lenkić et al., 2024), in addition to a plethora of IR-bright, dusty sources in the galaxy's central stellar bar (Sibbons et al., 2012; Jones et al., 2019; Hirschauer et al., 2020; Kinson et al., 2022). Additionally, coordinated parallel observations of off-target regions were obtained.

The observations with NIRCam comprised a total of ~4.80 hours of integration time and were obtained on 2022 September 4, utilising the F115W and F200W short-wavelength filters and the F356W and F444W long-wavelength filters. The dithering pattern (FULLBOX 4TIGHT) ensured the ~43″ gaps between the subarrays of each detector module were filled. Table 3.2 presents filter properties and Appendix Table B.1 gives a complete summary of exposure parameters.

Coverage of NGC 6822's central stellar bar was achieved by restricting the aperture position angle (PA) of the *JWST* spacecraft to between 92.0° and 93.0°. The NIRCam mosaic was centred at RA = 19:44:56.1990, Dec. = –14:47:51.29; the tile with a MIRI coordinated parallel is centred at RA = 19:45:00.2644, Dec. = –14:47:55.23.

MIRI observations totalling ~15.12 hours were obtained between 2022 September 4 and 2022 September 15, utilising the F770W, F1000W, F1500W and F2100W filters. The 1×6 mosaic was restricted to a PA of 93° centred at RA = 19:44:58.0949, Dec. = –14:48.20.62; the MIRI tile with a NIRCam coordinated parallel was centred at RA = 19:44:58.4923, Dec. = –14:46:40.85. A list of filter properties can be found in Table 3.3, and a list of exposure parameters, including groups per integration and integrations per exposure for each filter, is provided in Appendix Table B.2.

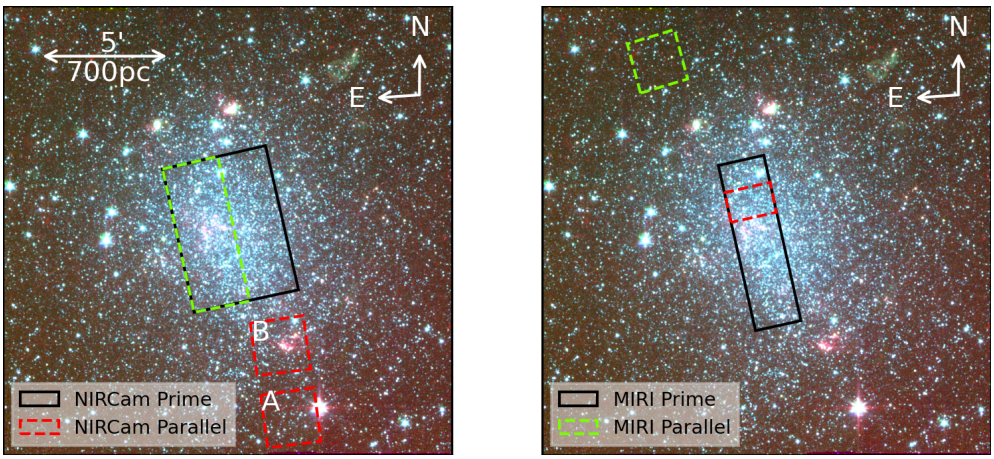

Figure 3.1 *Spitzer* three-colour image of NGC 6822 from Cannon et al. (2006) with the *JWST* NIRCam and MIRI survey regions superimposed (solid lines). The left image shows the NIRCam coverage and the right image the MIRI coverage. The NIRCam tile with an associated MIRI parallel is shown in green dashes, while the MIRI tile with its associated NIRCam parallel is in red dashes, with detector modules A and B labelled accordingly. North is up, and east is to the left.

Table 3.2 Summary of NIRCam observation properties. Note that the quoted values for the PSF full widths at half maximum are those of the empirical PSF.

NIRCam Observation Properties	
Survey area (arcmin^2)	29.0
Total time (hr)	4.80
Filters	F115W, F200W, F356W, F444W
Central λ (μm)	1.154, 1.990, 3.563, 4.421
FWHM at λ (pixel)	1.290, 2.129, 1.841, 2.302
Completeness limits at λ (mag)	25.60 24.58 23.21 23.09

3.2.1 Parallel Imaging

In addition to the primary observations, parallel observations were obtained in both NIRCam and MIRI. Only one of the two 2×1 mosaic tiles in the primary NIRCam observations has an associated MIRI coordinated parallel (green in Figure 3.1). This parallel observation was designed to provide background comparison images by observing a field offset from the primary target, taking into account the intrinsic physical separation between NIRCam and MIRI on the *JWST* focal plane. The pointing was positioned such that the eastern tile of our primary NIRCam mosaic was placed along the galaxy's main body, and the coordinated MIRI parallel was located north of the disk, offset from the Hubble X

Table 3.3 Summary of MIRI observation properties.

MIRI Observation Properties	
Survey area (arcmin^2)	14.5
Total time (hr)	15.12
Filters	F770W, F1000W, F1500W, F2100W
Central λ (μm)	7.528, 9.883, 14.932, 20.563
FWHM at λ (pixel)	2.445, 2.982, 4.436, 6.127
Completeness limits at λ (mag)	20.43 19.41 16.80 16.86

star-forming region.

One of the six mosaic tiles in the primary MIRI observation has a NIRCam coordinated parallel (red in Figure 3.1). This tile was selected due to the advantageous position in the instrument focal plane of the Hubble IV star-forming region, which falls into NIRCam's Module B. Module A is situated further from the galaxy and is thus a helpful pointing for obtaining information on a region of the galaxy that is not actively forming stars.

3.3 Data Reduction and Photometry

Due to the nature of inflight calibrations that were ongoing at this early stage of *JWST*'s operation, image processing was repeated and steps altered until the data were adequate for analysis. This was a collaborative effort across several research groups, as continual improvements were made to the underlying calibrations or workaround methods developed. The majority of the image reduction on this program was led by collaborators and will not be detailed in this thesis. For a complete description of the treatment of the raw data, see Nally et al. (2024) and Lenkić et al. (2024). Here, I offer a brief overview of the key details.

To obtain science-ready NIRCam images, uncalibrated raw exposures were processed through a modified version of the *JWST* reduction pipeline version 1.9.6 and Calibration Reference Data System (CRDS) version 11.16.20. Individual calibrated exposures were astrometrically aligned to *Gaia* DR3 using the *JWST/Hubble* Alignment Tool (JHAT; Rest, 2023). These are processed through the final *JWST* pipeline stage to produce stacked mosaics.

MIRI images were processed through the *JWST* pipeline version 1.9.5 using CRDS version 11.16.21. The only major deviation from the NIRCam image

Table 3.4 STARBUGII parameters used for all photometry.

Parameter	F115W	F200W	F356W	F444W	F770W	F1000W	F1500W	F2100W
SIGSRC	5.0	5.0	5.0	5.0	5.0	5.0	4.0	3.0
SIGSKY	2.0	2.0	2.0	2.0	1.8	1.8	1.8	1.8
RICKER_R	1.0	1.0	1.0	1.0	2.0	2.0	5.0	5.0
SHARP_LO	0.4	0.4	0.55	0.4	0.4	0.4	0.225	0.2
SHARP_HI	1.1	0.9	0.9	0.85	0.76	0.9	0.53	0.84
ROUND_LO/HI	±1.5	±1	±1	±1	±0.6	±1.0	±0.6	±0.5
ENCENRGY	0.6	0.6	0.6	0.6	0.6	0.6	0.6	0.6
SKY_RIN	3.0	3.0	3.0	3.0	4.0	4.0	5.0	6.0
SKY_ROUT	4.5	4.5	4.5	4.5	5.5	5.5	6.5	7.5
BOX_SIZE	15	15	5	5	2	5	5	8
CRIT_SEP	5	6	8	8	8	8	8	8
MATCH_THRESH	0.1	0.1	0.1	0.1	0.15	0.2	0.2	0.2
NEXP_THRESH	2	2	2	2	3	3	3	3

processing was the calibration of instrumental backgrounds. These were modelled from tiles in the mosaicing pattern that contained the least diffuse emission, and subtracted from the uncalibrated exposures.

3.3.1 Source Detection

Point-source photometry was extracted using the STARBUGII photometric tool and pipeline, which has been fully described in Chapter 2. As a reminder, this pipeline performs point-source extraction and band merging across multiple observations and wavelengths, utilising core functions from the python PHOTUTILS (Bradley et al., 2022) package. A complete set of relevant STARBUGII parameters and their values adopted for my photometric extractions are listed in Table 3.4.

The individual *Gaia*-aligned exposures are used for source detection with `starbug2 --detect`. Sources with a 5σ detection above the sky, which is initially estimated locally within an annulus, are first located by centroid fitting. The geometry of each point source is calculated, and SHARPNESS and ROUNDNESS values are assigned. As a reminder, SHARPNESS is the ratio of the peak pixel value of the source to its median within an aperture. I remove cosmic rays from the catalogue by setting an upper limit on SHARPNESS and faint peaks in the dust structure by setting a lower limit. The source symmetry is measured by comparing normal functions fit to the source along the vertical and horizontal axes, which

is defined as ROUNDNESS. I can remove most resolved background galaxies and further spurious detections within the dust structure by limiting the allowed level of asymmetry.

The NIRCam FULLBOX 4TIGHT dithering mode results in four sets of three overlapping exposures for a given pointing. Only sources detected in at least two frames of each set are retained in the resulting catalogue; any spurious source not meeting this threshold is discarded as a likely cosmic ray or other detector artefact while maintaining accurate sources at the detector edges. For the MIRI images, the FULL CYCLING SMALL mode results in four dithers, so I stipulate that a source must be detected in three or more exposures. The flux distribution between the exposures is examined, and sources with asymmetric distributions (the mean and median differ by more than 5%) are assigned the flag `SRC_VAR`. Matching between frames in the image stack is done with a nearest neighbour calculation with a threshold separation of 0.1 arcseconds.

I conduct aperture photometry on these sources in each individual frame. An aperture radius scaled to 60% of the encircled energy of the PSF and a sky annulus with an inner and outer radius of 3.0 and 4.5 pixels, respectively, is used for all NIRCam bands, and the aperture correction is interpolated between values given in CRDS `jwst_nircam_apcorr_0004.fits`. The MIRI images are treated the same, with 60% encircled energy aperture sizes but I increase the sky annuli to 4.0-5.5 pixels for F770W and F1000W, 5.0-6.5 pixels for F1500W and 6.0-7.5 pixels for F2100W to account for the larger PSFs at longer wavelengths. Aperture corrections are calculated from `jwst_miri_apcorr_0005.fits`. The data quality array within the aperture of each source is inspected and I flag sources with saturated or `DO_NOT_USE` pixels with the STARBUGII flag `SRC_BAD` and pixels that contained a jump during detection with `SRC_JMP`.

Table 3.5 contains a list of source counts for every filter and an estimate of their sensitivity values.

3.3.2 PSF Photometry

I conduct PSF photometry for the sources in the NIRCam images. The diffuse background emission underlying the images of NGC 6822 is modelled using `starbug2 --background`. This routine places masking apertures of varying sizes, calculated on the flux of each source, and fills them with the median pixel

value within a local annulus. For every pixel in the image, the background is measured by averaging all the local pixels within a set box size. This process creates an effective representation of the diffuse emission. By subtracting this diffuse emission background from a single exposure, I create a clean image of the field with diffuse emission removed, onto which PSFs can be accurately fit.

For each detector subarray within NIRCam, I generated a 5-arcsecond PSF using WEBBPSF (Perrin et al., 2014) version 1.1.1. I run PSF photometry using `starbug2-psf` on the background-subtracted image at the source positions from the combined and cleaned source list generated in the aperture photometry step. The centroid position is left as a free parameter, allowing both flux and position to be fit during the routine. If the newly fitted centroid position differs from the initial guess by more than 0.1 arcseconds, I refit the flux but hold the position fixed at the initial guess. This results in a poorer fit; therefore, I flag the source with `SRC_FIX`.

3.3.3 Photometric Corrections

I calculated and applied instrumental zero point magnitudes to calibrate the PSF photometry because the PSF models are not normalised to physical units. For each filter, a cleaned aperture photometry catalogue which retains only the most reliable point sources is used as the base to determine the zero point. To produce the clean source list from the main catalogue, both the faintest and brightest sources are removed to limit the number of sources with low S/N, partially saturated objects, and any potential remaining detector artefacts. Sources must have a photometric error of less than 0.1 and must not have any poor-quality data flags. These cuts eliminate over 80% of the sources in the main catalogue. Finally, these sources are matched to the equivalent source in the PSF catalogue. I use `starbug2 --calc-instr-zp` to calculate the median difference in the source magnitudes measured by aperture photometry and PSF fitting to obtain instrumental zero point magnitudes, which are subsequently used to calibrate the PSF photometry from STARBUGII to the AB magnitude system. For easier comparison with past works, I convert these magnitudes to the Vega system using the reference files `jwst_nircam_abvegaoffset_0001.asdf` and `jwst_miri_abvegaoffset_0001.asdf`.

Finally, as NGC 6822 is located at a low Galactic latitude, it is necessary to correct the photometry for foreground reddening. I adopt the value E(B−V) =

0.35 (Tantalo et al., 2022) to correct for the moderate Galactic foreground extinction and apply the extinction curve of Cardelli et al. (1989) assuming $R_V = 3.1$. Differential extinction internal to NGC 6822 was ignored, as this is assumed to be insignificant compared to photometric uncertainties due to crowding.

3.3.4 Catalogue

Individual filter band catalogues are merged together to form a combined NIRCam and MIRI point-source catalogue for NGC 6822 with `starbug2-match --band`. Before any matching, the photometric uncertainty of each source is assessed, and any sources with a magnitude error greater than 10% are removed from the individual catalogues. This reduces the likelihood of mismatching high-quality sources with any remaining spurious sources, producing a reliable band-matched catalogue at the possible cost of completeness.

Initially, I treat the NIRCam and MIRI catalogues separately, applying the same methodology to the band matching within each instrument. The matching routine starts with the shortest-wavelength catalogue, as the smaller PSF full width at half maximum (FWHM) leads to the highest astrometric certainty. This is matched with a nearest neighbours method to the next-shortest wavelength catalogue, with any unmatched sources above the separation threshold appended to the end. The position used for each source is taken from the shortest-wavelength catalogue in which it initially appeared, allowing for faint red objects such as highly dust-enshrouded AGB stars that are not visible in the near-IR to be retained. I used a separation threshold that increases as the PSF size increases, as using a single threshold larger than the astrometric uncertainty of the longest MIRI wavelengths would cause mismatching in the shortest NIRCam filters. I match short wavelength NIRCam filters using a threshold of 0.06″ and long wavelength NIRCam filters with 0.1″. Within MIRI I adopt 0.15″ for F770W and F1000W, 0.2″ for F1500W, and 0.25″ for F2100W.

Finally, I merge the NIRCam and MIRI catalogues with a separation threshold of 0.3″. I expect many of the reddest and most dust-enshrouded sources detected in the long-wavelength MIRI data to be missing from the shortest-wavelength NIRCam images. However, the depth and sensitivity of F115W and F200W result in a catalogue populated by many faint blue sources. Consequently, a simple positional matching approach between a long-wavelength MIRI band and

a short-wavelength NIRCam band would likely result in a significant number of mismatches due to the numerous sources present at short wavelengths, which lie along similar lines of sight. To combat this issue, I require any sources matched between NIRCam and MIRI to have an F444W detection. In other words, a source in the MIRI catalogue will be compared with all sources in the NIRCam catalogue within the matching radius and paired with the nearest source for which a detection in the F444W band exists. If no NIRCam sources within the matching radius are detected in the F444W band, the MIRI source will be assumed to have no NIRCam counterpart. It will subsequently be appended to the catalogue as a new object. Thus, both blue and red objects in the catalogue will be retained, and the chance of a mismatch between co-located sources will be reduced.

3.3.5 Foreground Contamination

To remove foreground Milky Way stars from the *JWST* NGC 6822 source list, I examine *Gaia* Data Release 3 (DR3 Gaia Collaboration et al., 2021) for foreground contamination. First, the *Gaia* catalogue is cleaned of sources with poor astrometry and possible non-single objects within the *JWST* FoV, as outlined by Fabricius et al. (2021). This involves keeping sources with: RUWE ≤ 1.4, astrometric_excess_noise_sig ≤ 2.0, visibility_periods_used ≥ 9 and ipd_gof_harmonic_amplitude ≤ 0.1. The cleaned *Gaia* catalogue is matched to the NGC 6822 photometry, resulting in 656 positive matches within the main field. Sources that exhibit a significant (5σ) parallax or proper motion are considered to be foreground sources and are thus removed from the catalogue. I check that the proper motion of the sources do not deviate significantly from the global proper motion of the NGC 6822, as outlined by Dimitrova et al. (2021).

In total, I find that 179 sources exhibit proper motion above the threshold, with all but one also deviating significantly from that of NGC 6822. I also find that every source with significant parallax also exhibits proper motion. This allows for 178 sources to be removed from the catalogue as foreground contaminants. Despite NGC 6822's proximity to the Galactic plane, I see a low number of foreground stars in the dataset. The STARBUGII detection routine is unable to recover many of the bright foreground stars due to the saturation limits of the data. Furthermore, *Gaia* only detects the brightest IR sources in NGC 6822; this, paired with the small FoV of the observations, means that the number of foreground contaminating stars in the catalogue is low, as expected.

3.4 Results and Discussion

3.4.1 Mosaic Images

The NIRCam prime mosaics shown in Figure 3.2 cover a FoV of ~29.0 arcmin^2, whilst the MIRI mosaic covers a ~14.5 arcmin^2 FoV, with the NIRCam FoV overlapping nearly the entirety of that of MIRI. These mosaics image NGC 6822, located at a distance of 490 kpc, with resolutions from 0.040″ (0.095 pc) to 0.145″ (0.344 pc) in NIRCam, and from 0.268″ (0.638 pc) to 0.673″ (1.601 pc) in MIRI. This provides an improvement over existing *Spitzer* imaging by up to a factor of 10.

The NIRCam field shows a smooth distribution of stars increasing in density towards the centre of the FoV. Scanning by eye reveals an assortment of clear extreme candidates with bright blue or red colours on a backdrop of many faint stars. The background galaxies are evenly distributed across the image, with some showing detailed spiral structures and others only visible in the longest wavelengths. A dense globular cluster (Hubble VII) is visible in the centre-right of the image. The extent of the MIRI footprint is overlaid as a white dotted line. The NIRCam data are almost devoid of all dust structure, whereas complex diffuse emissions completely dominate the MIRI data of the same region. The centre of the FoV covers the young massive star-forming region Spitzer I, for which a detailed study of the young stellar objects has been conducted by Lenkić et al. (2024).

3.4.2 Stellar Population Classification

This section presents *JWST* CMDs covering the galaxy within the full extent of the survey. I select colour combinations that highlight significant population separation and those which represent similar wavelength coverage as *Spitzer* filters used in the SAGE surveys (Meixner et al., 2006; Gordon et al., 2011). I adapt point-source classification methodologies and boundaries from prior work (Blum et al., 2006; Jones et al., 2017b; Hirschauer et al., 2020) and investigate the location various stellar populations occupy in different *JWST* colour combinations, which I anticipate will be helpful in future stellar surveys.

Figure 3.3 shows one NIRCam-only CMD (F115W−F200W vs. F200W) in contour

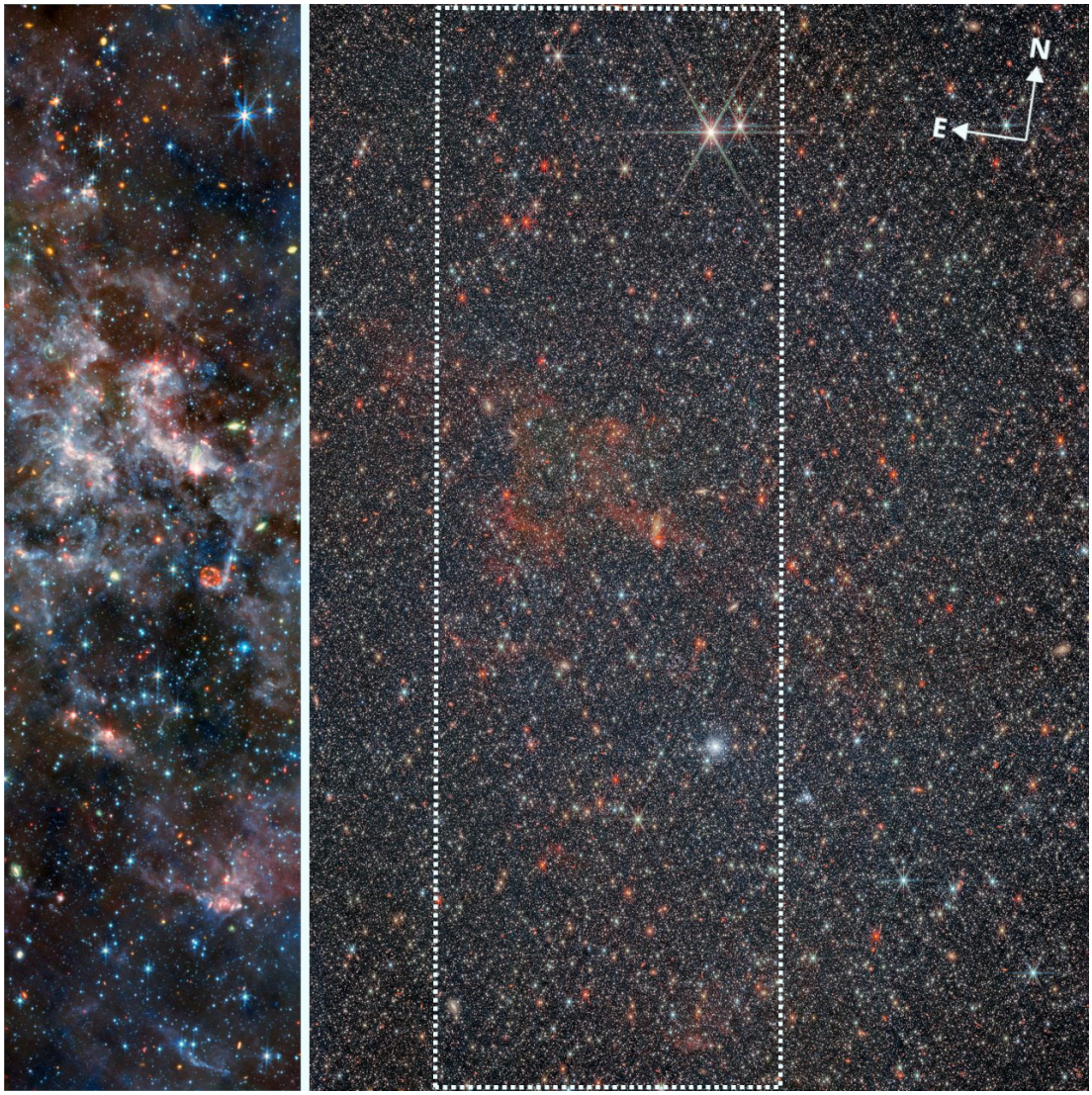

Figure 3.2 *JWST* full-colour mosaics displaying the spatial coverage from both instruments. The left shows MIRI coverage with F770W (blue), F1000W (green), F1500W (yellow) and F2100W (red). The right shows the NIRCam coverage with F115W (blue), F200W (cyan), F356W (yellow), and F444W (red), with the extent of the MIRI footprint marked by a white dotted line. East is to the left, and north points upward. Images credited to ESA/Webb, NASA & CSA, M. Meixner.

and Hess diagram format, one MIRI-only CMD (F770W−F1500W vs. F770W), and one combined CMD (F444W−F770W vs. F770W) with the most prominent populations indicated. The first CMD, with a filter combination most similar to the ($J - K_s$ vs. K_s) CMDs of previous NGC 6822 studies (e.g., Cioni & Habing, 2005; Sibbons et al., 2012; Whitelock et al., 2013), was chosen because it utilises the most sensitive photometry and therefore reveals the faintest populations. The diagram is shaped as a collection of sources that splits vertically into two main branches from the base, with the breadth of the base likely being a result of greater scatter as the sensitivity limit of the photometry is approached. The blue finger follows the *Upper Main Sequence* (UMS), with more massive stars appearing higher up. The right-hand fork is primarily the RGB, with the RC appearing as a dense bulge at F200W=22.1, and the *AGB bump* (AGBb) embedded just above at F200W=21.0. The vertical track seen above the RC is formed by intermediate-mass helium-burning stars (VRC) evolving toward the AGB. The RSG track splits from the RGB below the TRGB and runs diagonally upward, consisting of some of the brightest sources in the galaxy. Above the TRGB, the TP-AGB stars separate into OAGB and CAGB. A fraction of the TP-AGB will likely be mid-thermal pulse and sit below the TRGB. Formal separation of these fainter AGB stars from RGB stars is difficult photometrically due to this overlap; however, they make up only a small percentage (<10%) of the overall TP-AGB population (Boyer et al., 2015a).

Upper Main Sequence

The UMS population is visible in the top left panel of Figure 3.3 as the prominent branch located at F115W−F200W < 0.4 and approaching F115W−F200W = 0.0. At F200W = 25.0 this branch connects with the base of the RGB, though it is unclear if this constitutes the *Main Sequence Turn-Off* (MSTO) for an aged population as the confusion introduced into the photometry as it approaches the completeness limit merges the populations together. An optical survey of NGC 6822 by Zhang et al. (2021) isolated the UMS with ages <100 Myr and confirmed that the population perfectly traced the HI gas distribution that lies orthogonal to the bulk of the stellar component of the galaxy. Because they trace recent star formation, these stars provide information about the underlying gas and its evolution over time.

UMS stars are generally very bright and have expelled any nearby dust; they possess SEDs peaking in blue wavelengths. As such, they are detectable in the short NIRCam filters but become difficult to detect at longer wavelengths.

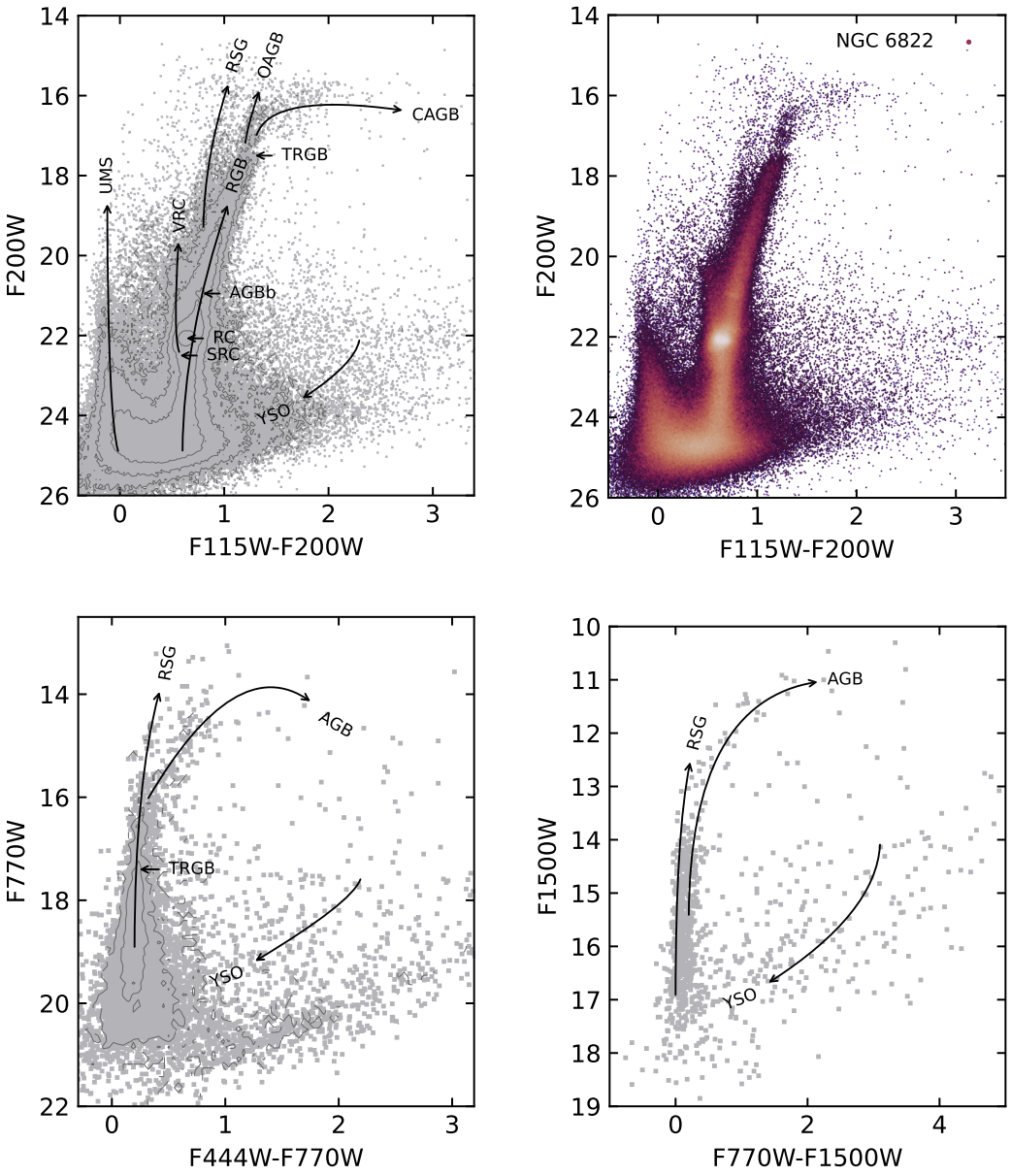

Figure 3.3 Colour-magnitude diagrams over three filter combinations with broad stellar classification tracks overlaid and labeled accordingly, point density displayed as contours where appropriate: F115W – F200W vs. F200W (top), F444W – F770W vs. F770W (lower left) F770W – F1500W vs. F1500W (lower right). Upper right plot shows a second F115W – F200W vs. F200W CMD in Hess format.

Red Giant Branch

The RGB begins at F200W = 25 and F115W − F200W = 0.6 in the top left panel of Figure 3.3 and extends vertically in a steep diagonal towards the red. This sequence is formed by stars that have just left the MS and have begun H-shell burning. It is one of the most prominent features in near-IR CMDs. In a single-aged population, the MSTO will appear as a tight track connecting the MS to the base of the RGB. The multi-aged population of NGC 6822, a product of continuous star formation, broadens the RGB and is consistent with an old population spanning 2−10 Gyr. Previously Zhang et al. (2021) isolated the brighter portion of this branch to show that the old stars contribute to the galaxy's eccentric elliptical stellar component that twists radially and is perpendicular to the younger stellar component.

The TRGB is well-defined in the shorter wavelengths, as shown in Figure 3.3, but it does not appear as a distinct feature in the longer MIRI filters. The method of roughly calculating its position is discussed in Section 3.4.3.

The position of a star on the RGB depends on its age and metallicity, but disentangling these effects is not straightforward. Younger RGB stars appear slightly to the blue, while older RGB stars appear more to the red when considering a fixed value of metallicity. On the other hand, when given a fixed population age with varying metallicity, more metal-poor stars appear bluer than the more metal-rich stars. This effect is known as the age-metallicity degeneracy (Worthey, 1999; Carrera et al., 2008). For a given individual star, it is difficult to determine with certainty whether its position on the RGB is caused by its age, metallicity, or both. It results in a spreading of the sequence; the width of the RGB in the CMDs exceeds the expected characteristic scatter caused by photometry uncertainty, and therefore, it is likely caused by a broad range of ages and metallicities across the galaxy. Indeed, detailed surveys of the metallicity of NGC 6822 have been conducted by Patrick et al. (2015), who detect a metallicity gradient across the innermost regions of the galaxy, which coincides with the *JWST* FoV. Furthermore, the spread in RGB colour in the *JWST* CMDs is in agreement with Tantalo et al. (2022, 2025), who find that the RGB in NGC 6822 spans 1.2 mag in $g - i$ colour, indicative of NGC 6822's complex star-formation history and chemical composition.

Red Clump

Low-mass stars evolving up the RGB deposit helium onto their degenerate core. Once a sufficient core mass (0.48 $M_{\odot}$; Bildsten et al., 2012) is reached, the core temperature breaks the electron degeneracy suddenly, in a helium flash (Habing & Olofsson, 2003, and references therein). The uniform initial characteristics of the now helium-burning cores lead to the stars clustering in a tight sequence on the CMD, known as the RC, with the differing properties predominantly affecting their convective outer layers. Lower mass or more metal-poor stars will have less massive convective layers above the core which will cause less "dampening" of the radiation and therefore appear in the hotter HB, not immediately visible on the CMDs (see Girardi, 2016, for a detailed review on RC stars.).

Due to its prominence and well-defined position in CMDs, the RC can be used as a standard candle due to its small dependence on age (e.g., Bovy et al., 2014; Ruiz-Dern et al., 2017; Ting et al., 2018; Hawkins et al., 2018) although there is a small metallicity dependence (Alves, 2000; Shan et al., 2018).

The over-density from the RC structure is pronounced in the CMDs, sitting just left of the RGB at F200W $\sim$ 22.1. In the shortest-wavelength filters, I resolve sources three magnitudes below the RC; however, a decrease in the depth of photometry at redder wavelengths prevents their detection at $\lambda > 4$ μm, as shown in Figure 3.3. The RC has been used to measure SFH in NGC 6822 (e.g., Wyder, 2001) by comparing age-sensitive RGB with the age-insensitive RC. The increased sensitivity of the catalogue will allow for more finely sampled calculations of the SFH within the inner regions of the galaxy. Additionally, differential reddening in NGC 6822 introduces a spread in the photometry of the theoretically tight RC. This effect can be used to build an extinction map of the galaxy (Wyder, 2001). Such an exercise is beyond the scope of this study, which can be addressed in the future.

Vertical Red Clump

Intermediate mass stars do not experience a helium flash and instead begin quiescently burning helium in their cores (Habing & Olofsson, 2003; Karakas, 2017b). The ignition of helium moves them off the RGB and onto a vertical sequence shown on the CMDs in the upper panels of Figure 3.3 at a colour of F115W-F200W=0.6 and 2.5 magnitudes from F200W=22.5. The feature is often associated with the RC on CMDs and therefore gets the name, VRC (Girardi, 2016).

VRC stars' luminosity monotonically increases with stellar mass (Girardi, 1999). The feature extends a few tenths of a magnitude below the RC, with the limiting depth marking the critical lowest mass above which helium can ignite quiescently in the core (~2 $M_{\odot}$; Chiosi et al., 1992). This is visible as a small plume underneath the RC in the upper right panel of Figure 3.3 and is known as the Secondary Red Clump (SRC; Girardi et al., 1998).

AGB Bump

The AGBb is a population of rarely-observed stars that emerges as evolving early AGB stars stall momentarily as their H-burning shells are extinguished by the expansion of their convective layers, with the ignition of the He-burning shell (Caputo et al., 1978; Dréau et al., 2022). Observing this feature is difficult, as it requires a large number of sources and may be quickly obscured by even minor photometric errors. Yet, it is clearly visible in the upper plots of Figure 3.3 embedded in the RGB at F200W = 21. The age and metallicity of the stars influence their positioning on the CMD, and as such, the AGBb can be used to gain some insight into the SFH of the galaxy (Ferraro, 1992). Although the AGBb is visible in optical data in NGC 6822 (Tantalo et al., 2022), this often neglected population is a useful mark to constrain evolutionary tracks.

Red Supergiants

At F200W = 19.5, the RSG branch forks blueward from the RGB and extends steeply to the saturation limit of the data. The sequence is clearly visible in the upper-right plot of Figure 3.3, although the source density drops at the brightest end. This corresponds to the upper part of the red helium burning sequence. The existence of an RSG population in the galaxy has been shown by Gallart et al. (1996a), Whitelock et al. (2013), Hirschauer et al. (2020), Dimitrova et al. (2021) and Tantalo et al. (2022), where they follow the structure of the central bar. This result was expected as RSG stars are young (8–20 Myr) and massive (~8–40 $M_{\odot}$), so have not had sufficient time to wander far from the star-forming sites in the centre of the galaxy (e.g., Humphreys & Davidson, 1979; Massey & Olsen, 2003; Davies & Beasor, 2018). The colour-cut to isolate this branch is denoted by the green region drawn in the left panel of Figure 3.4. The region is drawn by eye based on point densities in the CMD and was informed by previous NGC 6822 stellar classification studies (Sibbons et al., 2012; Hirschauer et al., 2020). The isolated RSG stars form a distinct blue "horn" in F444W – F770W vs. F770W as seen in the lower-left panel of Figure 3.3 where the labelled arrow marks the span

of the branch. In the longer MIRI wavelengths, the generally dust-free stellar sources compress at a colour of zero, whereas RSG and O-rich AGB stars that are surrounded by dust envelopes also have similar, but redder, mid-IR colours due to their dust grains following the same condensation sequence (Ferrarotti & Gail, 2006). Thus, separating RSG and AGBs (with and without a circumstellar excess) becomes more difficult in the lower right panel of Figure 3.3.

Asymptotic Giant Branch

In Chapter 4, I will revisit the evolved star populations to explore their dust production properties in more detail. Here, I present initial cuts to determine the general positions of the RSG, OAGB, and CAGB stars. To inspect the locations of these evolved populations in colour space, I show in the first panel of Figure 3.4 a zoom-in of the F115W−F200W vs. F200W CMD, where they appear to follow diagonal sequences upwards and to the red following the stars' core H and He exhaustion. Thermally pulsing AGB stars occupy the reddest and brightest branches. Above the TRGB at F200W = 17.5, a small gap separates the TP-AGB stars from the RGB. For populations fainter than the TRGB, there can be substantial overlap in colour between early AGB stars, RSGs, and the more numerous RGB stars (as seen by Tantalo et al., 2022, in NGC 6822), which limits classification accuracy.

AGB stars can be separated by the distinct chemical makeup of their photospheres. Here, free carbon and oxygen are bound in very stable CO molecules. The overabundance of one of the two components is then left unbound in the photosphere. It will form the basic ingredient for the atmospheric chemistry and dust grain formation once it is lifted from the stellar surface into the circumstellar envelope of the star (Bowen, 1988). AGBs with a C/O ratio > 1 are defined to be carbon-rich, and those with C/O<1 are oxygen-rich (Iben & Renzini, 1983). The molecular and dust species formed are dictated by this chemical difference, with CAGBs forming carbonaceous molecules and dust grains whilst OAGBs form oxides and silicates, enabling these evolved populations to be photometrically separated (e.g., Habing & Olofsson, 2003; Höfner & Olofsson, 2018, and references therein).

For the bright TP-AGB stars, I separate the CAGB and OAGB sequences with a diagonal line above the TRGB at F115W − F200W ≥ 1.4 with a gradient of -12.8. Historically the AGBs in NGC 6822 have been split with a vertical line in the near-IR (see e.g., Cioni & Habing, 2005; Sibbons et al., 2012), or by

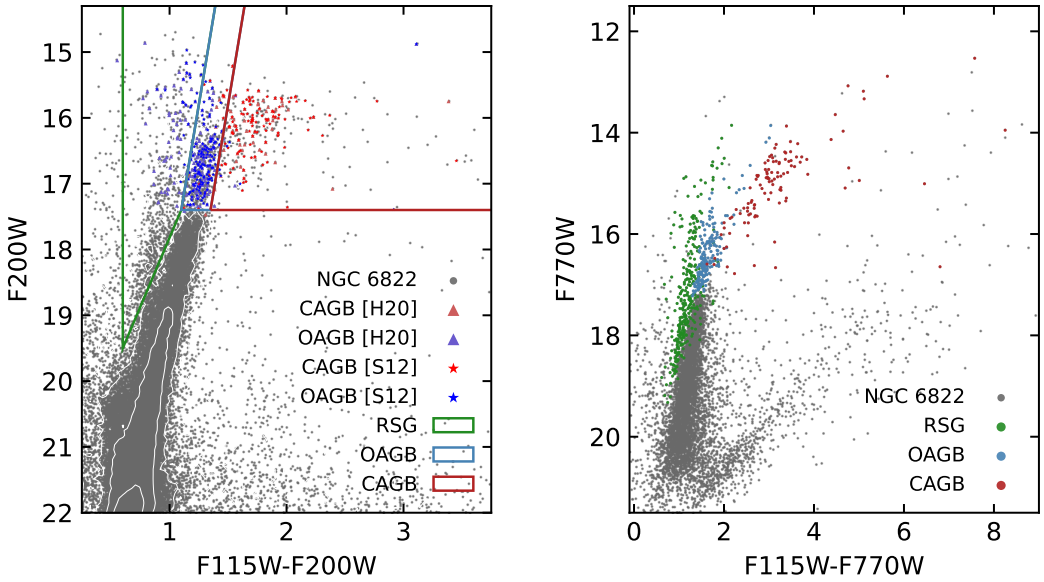

Figure 3.4 CMDs showing the evolved population separation from near-IR to mid-IR. The candidate RSGs in green, OAGBs in blue, and CAGBs in red in the right panel are defined by the solid boundaries shown in the F115W – F200W vs. F200W CMD (left panel). The white contours represent the source density on the RGB. The left plot also shows the OAGB (blue) and CAGBs (red) candidates classified by Sibbons et al. (2012) (stars) and Hirschauer et al. (2020) (triangles).

employing a wide range of colour diagnostics to identify members of this bright intermediate-age stellar population (e.g., Tantalo et al., 2022). Combining mid-IR *Spitzer* and near-IR United Kingdom Infrared Telescope (UKIRT) data for broader baseline photometry, Hirschauer et al. (2020) developed a novel statistical approach to separate them with more complex colour cut boundaries. I cross-match the catalogue with the catalogues of AGB candidates from Sibbons et al. (2012) and Hirschauer et al. (2020) to identify where these populations lie on the *JWST* CMDs. I present this comparison in the first panel of Figure 3.4, where blue data points represent OAGBs and red data points represent CAGBs. I find that the classification of sources as CAGB stars by both of these previous studies is broadly consistent with the colour space they occupy in the *JWST* CMDs (red region), with a total of 165 sources in agreement and 14 OAGBs being classified as CAGB within the cuts. Similarly, I find a total of 241 OAGB classifications in agreement with 21 CAGBs being classified as OAGBs here.

Separating the OAGBs and RSGs is more involved due to the lower point density in the CMD at the brightest magnitudes. However, RSGs typically have warmer effective temperatures than AGB stars and do not experience a third dredge-up, so they ordinarily have slightly bluer colours and are less numerous than the AGB stars. To select RSG stars, I adopt a diagonal line above the TRGB at F115W − F200W = 1.1. In contrast, below the TRGB the colour selection is informed by the prominent density changes at the blue edge of the RGB branch, until a depth of 19.5 mag when the brightest VRC stars begin to overlap with RSG stars; this region (denoted in green) is where I classify objects as RSGs. In the Magellanic Clouds, the $J - K_s$ vs. K_s CMDs of Blum et al. (2006) and Boyer et al. (2011) possess a similar RSG feature.

The majority of the OAGB candidates from Sibbons et al. (2012) and Hirschauer et al. (2020) are classified as OAGB stars in the *JWST* data. However, 70 of these sources appear to fall within the space I define as corresponding to RSGs. This is to be expected as separating these classifications becomes difficult towards the mid-infrared (Boyer et al., 2011; Jones et al., 2017a). Here, there is some overlap between the two branches as stellar temperature no longer affects the CMD; spectroscopy is required to distinguish between them definitively. Finally, there are a few sources that were previously classified as OAGB or CAGB that fall along the RGB; these are likely TP-AGBs that are mid-pulse or stars that have not yet undergone a third dredge-up (Iben & Renzini, 1983). A caveat of this comparison is that the improved resolution of *JWST* resolves previous

bright sources into multiple fainter stars. These would appear on the CMD in the first panel of Figure 3.4 to the right of the RGB and below the space occupied by CAGBs. These sources (roughly half from the catalogues of Sibbons et al., 2012; Hirschauer et al., 2020) have however been omitted from Figure 3.4 for clarity. While the colour cuts I have applied here effectively distinguish the brighter, least contaminated regions of the evolved stellar populations' colour space, I caution that circumstellar extinction imposes limitations on identifying the dustiest sources in the near-IR. Although it is assumed that everything to the red of the diagonal cut I have defined at F115W−F200W= 1.35 (red line) is a CAGB (Boyer et al., 2015b), in cases where OAGBs and RSGs produce large quantities of silicate dust, they will also occupy this colour space (Aringer et al., 2016; Jones et al., 2017a). Separating the dustiest OAGB and CAGB stars requires spectroscopic observations. I also expect that for the most extreme dust-enshrouded AGB stars, extinction will cause the star to have a very red colour and be fainter than the TRGB used to identify the evolved stars in Figure 3.4. As such, these heavily extinguished sources will be excluded from the AGB classification. However, these objects are extremely rare and short-lived (van Loon et al., 2010).

Using the classification schemes defined above, I overlay the sources onto F115W−F770W vs. F770W in the second panel of Figure 3.4. The RSGs, OAGBs, and CAGBs remain visible as three distinct populations, although increasing absorption effects caused by dust at longer wavelengths begin to increase the scatter among the populations. This colour combination distinguishes the CAGBs from the OAGBs, with the bulk of the two populations separated by nearly one magnitude in colour space. This combination bears a close comparison with the $J-[8.0]$ CMD of the LMC from Blum et al. (2006), where the RSGs and CAGBs fork above the bulk of the OAGBs. With NIRCam- and MIRI-equivalent filters, I observe the same morphology.

Long-wavelength MIRI photometry is crucial for chemically distinguishing the most dust-enshrouded sources in the catalogue. Figure 3.5 shows the distribution of sources in F770W − F2100W vs. F2100W, where the source density is very low due to the significant dust presence and rarity of sources which are bright at these wavelengths. The CMD splits into two distinct groups, spanning six magnitudes in colour space. This combination has shown to be analogous to *Spitzer* [8.0] − [24] vs. [24] in work by Jones et al. (2017b), which allows me to draw a comparison to SAGE work on the LMC where Srinivasan et al. (2009) demonstrated a triple forking sequence. In their work, CAGB (and extreme-

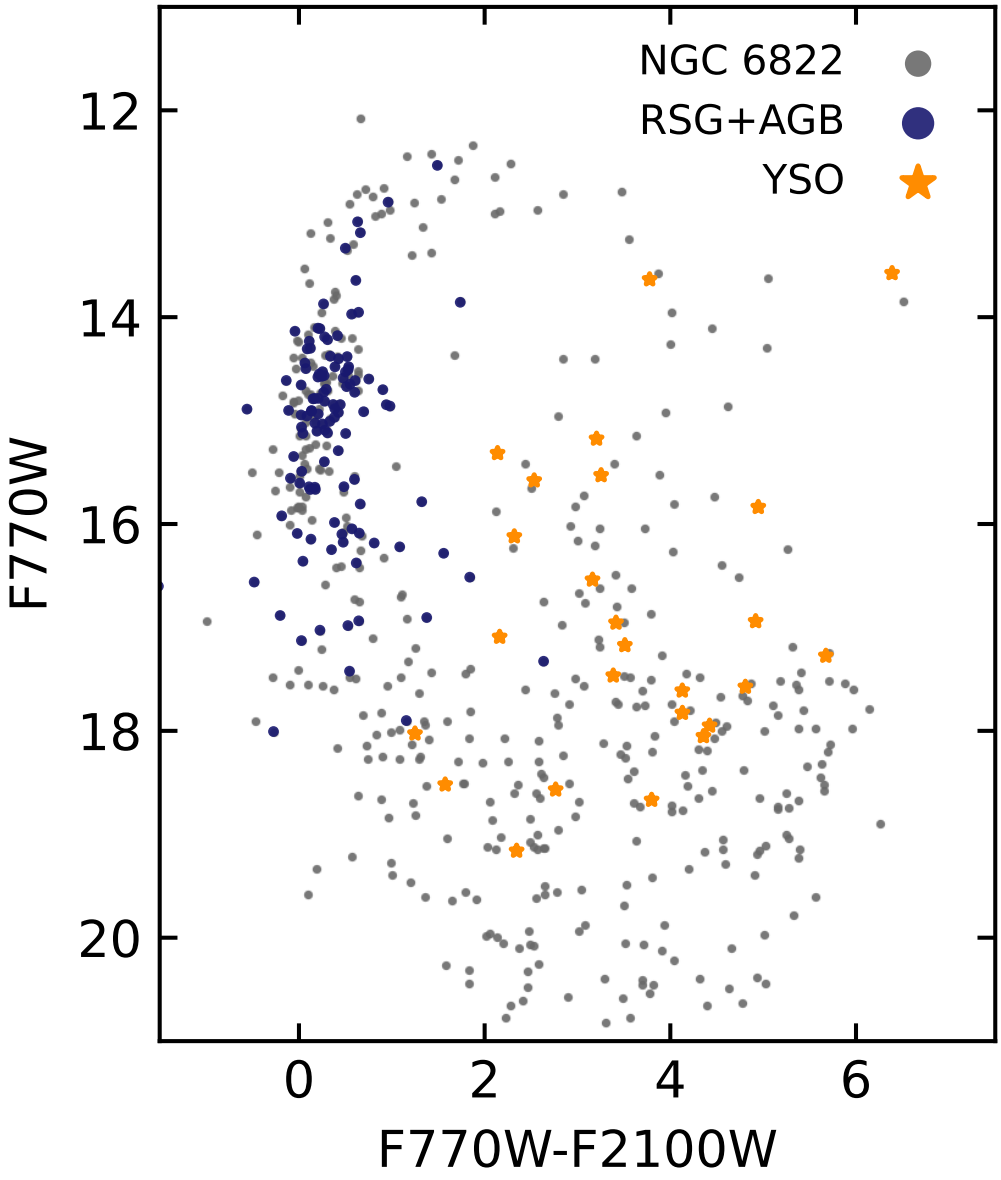

Figure 3.5 Colour-magnitude diagram with MIRI F770W – –2100W *vs.* F770W. NIRCam-identified RSG, OAGB and CAGB candidates are overplotted in blue and YSO sources from Lenkić et al. (2024) are overplotted in orange.

AGBs) lie on the most luminous and blue finger of the fork, whereas the OAGBs are fainter and redder but bifurcate into two fingers above [8.0] − [24] > 1. Later, Sargent et al. (2011) used the Grid of Red supergiant and Asymptotic giant branch star ModelS (GRAMS) models to show that the central fork is occupied by OAGBs exhibiting the highest mass loss, as well as some RSG stars. The CMD suffers from a low number of sources, drawing a direct comparison is difficult, but the most extreme AGB stars turn over at F770W∼13 and the RSG and less extreme AGBs collect on F770W-F2100W=0.

Young Stellar Objects

In all filter combinations shown in Figure 3.3, the YSOs reside in the red area to the right of the RGB, below the CAGB sequence. These red dust enshrouded objects have characterisable SEDs which typically rise towards longer wavelengths. Lenkić et al. (2024) identifies 140 YSOs in the Spitzer I region in NGC 6822, using *JWST* data. I overlay the high-confidence YSOs from that study onto Figure 3.5, demonstrating the effective separation of these young pre-main-sequence sources from AGB and RSG sources using MIRI filters. The *JWST* colour cuts to identify young populations are summarised in Lenkić et al. (2024) and Jones et al. (2023a). The area in the CMD where YSOs reside may also be inhabited by any contaminating background galaxies that remain after the cuts described in Section 3.3.1 have been applied.

3.4.3 Luminosity Functions

In Figure 3.6 I present the luminosity function from the whole band merged catalogue in the F115W filter. The logarithmic-scaled distribution is plotted in black, and its linearly-scaled version is plotted in filled grey. The optimal bin width is calculated for the number of sources present in each case using Knuth's Rule (Knuth, 2006). I crudely estimate the completeness of the sample in each *JWST* filter by identifying the location of the turnover of the luminosity functions at the faint end of the magnitude distribution for each band, marked in the figure with a dashed line.

I measure the TRGB for every filter in the catalogue sensitive enough to detect it. The TRGB is an essential feature from an astrophysical perspective, as it is a well-constrained standard candle that depends only weakly on age and metallicity (Cioni et al., 2000; McQuinn et al., 2019; Freedman et al., 2020). It

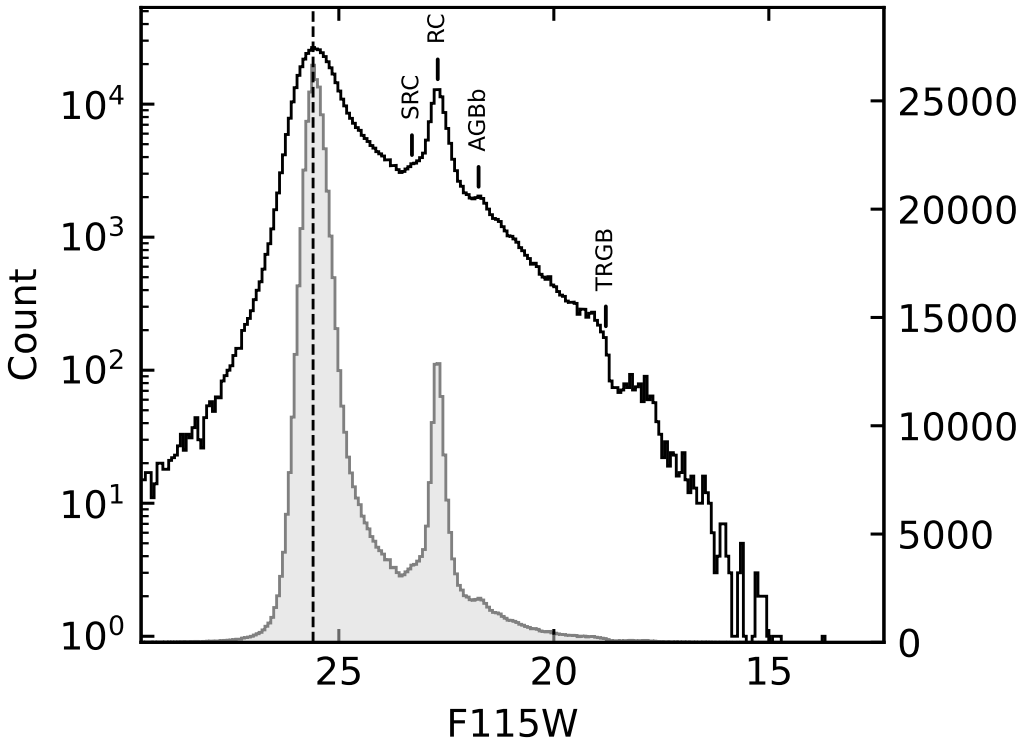

Figure 3.6 Luminosity function for the F115W filter. Log-scaled distribution is drawn in black and linear-scaled distributions in filled grey. Bin sizes have been scaled optimally for the number of sources detected. A dashed vertical line denotes the inferred completeness estimates, and the locations of TRGB, AGBb, VRC, and SRC are marked. Before generating this luminosity function, the F115W catalogue is cropped to F115W−F200W> 0.4, removing the UMS.

represents the final stage of evolution along the RGB before the onset of helium core burning, moving the star off this branch and onto either the HB, RC, or VRC, depending on the age, metallicity, and mass of the star. At this upper boundary, RGB stars have a hydrogen-burning shell supported by an electron-degenerate core of helium. This prominent feature is used to separate the RGB stars from the TP-AGB stars, which are typically (~90%) brighter than the TRGB (Boyer et al., 2015a). Due to molecular emissions in the photosphere of the RGB stars, it is expected that the TRGB will not be flat but will slope upwards in the IR (e.g., McQuinn et al., 2019; Cerny et al., 2020; Durbin et al., 2020). This results in a less steep drop in the luminosity function than would be expected in the optical. This spread in the measured *JWST* TRGB magnitudes and corresponding uncertainty requires careful empirical calibration before use as a standard candle. The TRGB positions measured here are estimates to provide context for identifying features and stellar populations in the *JWST* CMDs; a comprehensive analysis of the TRGB position and its slope is beyond the scope of this study.

To measure the position of the TRGB, I first remove the blue UMS sources with F115W−F200W< 0.4. I randomly sample each source from a normal distribution, based on its magnitude and magnitude error. I build a new "*sample*" distribution from all these sampled points, and smooth it with a kernel density estimate. The first-order derivative of the smoothed distribution is calculated using a Savitzky-Golay filter, and the TRGB is located at the point of steepest decline, as indicated by a sharp trough in the differential. This process is repeated thousands of times with different samples of the catalogue, and the results are averaged to determine the TRGB. I quote the error on this measurement from the standard deviation of the calculated TRGB values for multiple iterations of the algorithm, which accounts for the distribution of photometric errors in a given magnitude bin (see e.g., Hirschauer et al., 2020; Jones et al., 2023b).

The SED of an RGB star steadily falls with increasing wavelength in the IR. It will become undetectable in the mid-IR, where an IR excess from circumstellar dust may also contribute to the flux emission from AGB and RSG stars, potentially causing the most extreme of these to drop below the TRGB. Furthermore, at these wavelengths, other objects (e.g., YSOs) with cold dust emission may contribute substantially to the integrated flux (Jones et al., 2015b). This makes a clear identification of the TRGB challenging in the MIRI data. I identify the TRGB in MIRI up to and including F1000W with the procedure described above, but it is not visible in F1500W and F2100W. Table 3.5 lists the number of sources

Table 3.5 Source count per filter and sensitivity limits estimated by locating the turnover at the lower end of the luminosity functions, and upper limits placed around the brightest collection of sources. The TRGB is calculated by finding the point of steepest decline in the luminosity function. All magnitudes are given in the Vega system.

Filter	Source Count	Completeness [VegaMag]	Bright Limit [VegaMag]	TRGB (error) [VegaMag]
F115W	792424	25.57	15.3	18.79(04)
F200W	539377	24.58	15.0	17.51(03)
F356W	184141	23.21	14.5	17.49(06)
F444W	155327	23.09	14.0	17.65(12)
F770W	97817	20.43	12.5	17.43(19)
F1000W	7098	19.41	11.5	17.40(13)
F1500W	1311	16.80	10.0	-
F2100W	794	16.86	9.0	-

detected at each wavelength, the corresponding faint and bright source limits for that filter, and, where appropriate, the magnitude of the TRGB.

In F115W I am roughly complete to F115W = 25.57, around ~2.8 magnitudes below the RC population visible at F115W ~ 22.1 mag. This feature is not symmetrical; a shoulder is present towards fainter magnitudes at F115W=23.3, which is formed by the plume of the SRC described in Section 3.4.2.

The luminosity function also shows the prominent AGBb (Ferraro et al., 1999) at F115W = 21.75 and the TRGB at F115W = 18.79. The prominent nature of the TRGB position may allow further constraints on the distance to NGC 6822 and improve our understanding of the sloped relation visible in the IR. Brighter than the TRGB, the AGB stars form a shoulder to F115W = 18.0. Saturation affects the completeness of the catalogue at around F115W = 15.3. This low saturation limit will cause the sample to be less sensitive to the brightest sources detected in JHK_s data in previous surveys.

3.4.4 Parallel Field Photometry

The spatial coverage of the two parallel fields is shown in Figure 3.1. NIRCam parallel B contains the star-forming region Hubble IV. NIRCam parallel A contains no known areas of active star formation but is contaminated by the PSF spikes from a bright off-field foreground star, which may affect the quality of the photometric extractions for point sources located within these spikes.

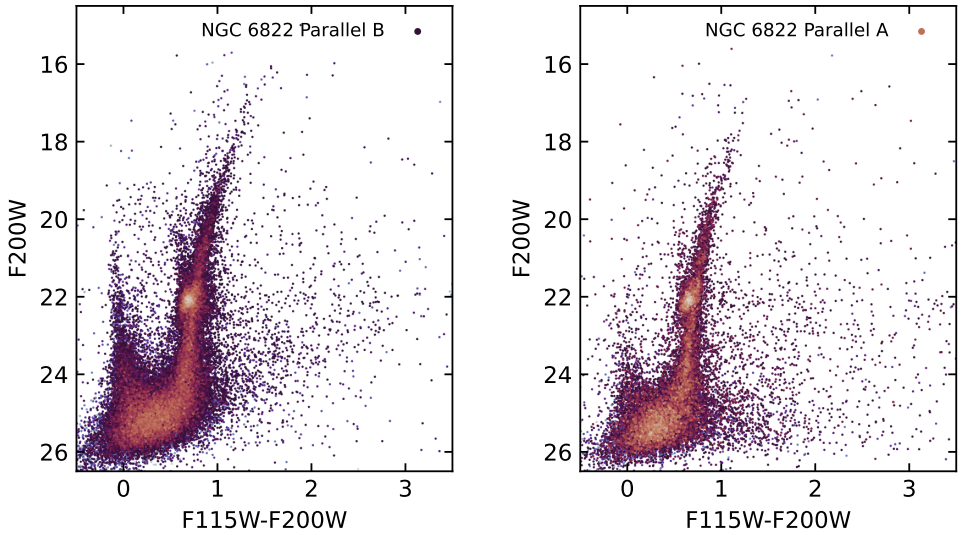

Figure 3.7 Colour-Magnitude Diagrams F115W – F200W vs. F200W in Hess format for the parallel imaging fields. Parallel B (left) is the NIRCam module B, appearing closest to the centre of NGC 6822, containing the star-forming region Hubble IV. Parallel A (right) is the NIRCam module A, the furthest field away from the centre of the galaxy.

I conduct photometry for the two NIRCam parallel imaging fields and plot the F115W – F200W vs. F200W CMD in Figure 3.7. For consistency, the STARBUGII photometric parameters listed in appendix Table 3.4 used for the main field of NGC 6822 are also used for the photometric extraction in these parallel fields. I also match the parallel catalogues to *Gaia* DR3 and remove any foreground contaminants that meet the criteria given in Section 3.3.5, before generating any CMDs and correcting the catalogue for extinction as described in Section 3.3.3. Both parallel fields A and B have source detections approximately 0.5 magnitudes deeper than the main field, likely due to the decreased crowding and hence a lower surface brightness in these regions.

The NIRCam parallel B field contains young UMS stars seen in Table 3.7 as a tight track on the left of the CMD. The RGB turns off and extends upwards to the red, but the TRGB itself is not well defined. The RC sits prominently to the left of the RGB, from which the intermediate-age VRC track extends vertically. A faint track of RSG stars splits from the RGB at F200W~19.5 and is well separated from a small collection of AGB stars above the TRGB calculated in Table 3.5.

NIRCam parallel A does not contain many UMS stars beyond a short scattered track above the MSTO. Similarly, the VRC stars are only marginally present, and no obvious RSG sequence is seen. The relative lack of very young stars is

due to the absence of an active star-forming region in the FoV.

3.5 Summary

In this Chapter, the *JWST* NIRCam and MIRI data of the central region of NGC 6822 are reduced into mosaics. I conduct source detection on images in all eight photometric bands, perform PSF photometry on NIRCam and aperture photometry on the MIRI exposures. By band-matching all eight source lists, I create a deep catalogue of the central stellar bar.

Using CMDs, I demonstrate the diverse array of young and old stellar populations present in the region. These include the UMS and RGB, along with the RC (and its associated structures), the bright evolved AGB and RSG stars, as well as the elusive AGBb. Using luminosity functions, I estimate TRGB measurements in NIRCam and MIRI filters. Finally, using parallel near-IR photometry of fields outside the central stellar bar, I demonstrate that the young populations are absent or significantly reduced in number.

4 AGB Dust Production

The 're' in research stands for 'redo'.

— Margaret Meixner

4.1 Introduction

TP-AGBs are key producers of dust in galaxies (Riebel et al., 2012; Boyer et al., 2015b; Srinivasan et al., 2016; Jones et al., 2018; Hoppe et al., 2022), responsible for enriching their ISM. During this evolutionary phase, they can lose up to ~80% of their initial mass through dust-driven mass-loss (Gall et al., 2011). Although AGB stars evolve more slowly than high-mass stars, which end their evolution in a supernova explosion, they can produce large quantities of dust in as little as 30 Myr (Boyer et al., 2017). Additionally, unlike supernovae, which potentially destroy dust produced during earlier stages of the star's evolution, AGB-produced dust is not subject to imminent destruction from the progenitor star, establishing them as crucial contributors to the massive dust reservoirs seen in high redshift galaxies (Algera et al., 2023; Schneider & Maiolino, 2024b).

In this Chapter, I aim to constrain the properties of AGB star candidates in NGC 6822 and measure their dust production rates. This work builds directly on the work presented in Chapter 3, utilising high-quality *JWST* photometry extracted using STARBUGII. Section 4.2 describes the improved photometric measurements used in this chapter. In Section 4.3, I describe the modelling of the individual stars' SED to determine their stellar parameters and chemical classification. I present the results in Section 4.4 and the conclusions in Section 4.5.

4.2 Improved Photometry

4.2.1 MIRI PSF Photometry

The NGC 6822 MIRI has complex variable background emission, making PSF point-source photometry challenging. In Chapter 3, *JWST* source catalogues were produced using PSF photometry for NIRCam observations and aperture photometry to extract fluxes of point sources in the MIRI data (see also Nally et al. (2024) and Lenkić et al. (2024). At the time of processing, model PSFs for MIRI did not fully characterise all optical distortion effects (Gáspár et al., 2021; Dicken et al., 2024). Thus, the MIRI aperture photometry catalogues for NGC 6822 have larger errors due to the complex backgrounds in the annulus and may include slightly extended sources, like background galaxies in low surface brightness regions and bright, dusty density enhancements in high background areas.

Following updates to the calibration files in September 2023, including a time-dependent flux calibration and revised aperture corrections (STSci, 2023), high-quality PSFs for MIRI became available. Here, I use these to conduct PSF photometry on the MIRI F770W, F1000W, F1500W and F2100W data with STARBUGII (Nally, 2023) version 0.7.3 to produce a high-fidelity MIRI point-source catalogue for NGC 6822 and improve the flux estimates and associated errors of the extracted objects. I perform source detection on each of the single-band mosaics, which have the best signal-to-noise and hence reveal the faintest dust-embedded sources compared to the individual exposures. I use `starbug2 --detect` with the relevant STARBUGII parameters given in Table 4.1. These parameters have been fine-tuned to detect low-contrast sources even in dense regions with a high background. Other detection parameters, such as SHARPNESS and ROUNDNESS, provide a quality assessment of the detected sources. Their parameters were chosen to remove sources with values characteristic of cosmic rays, extended or resolved objects, clusters, blends, and imaging artefacts.

One challenge with the MIRI data compared to NIRCam is the presence of false detections caused by bright dust peaks that are prevalent in mid-IR images. To address this complexity, I use the SMOOTHNESS parameter in STARBUGIIdescribed in Section 2.2.4. As a reminder, this source parameter measures how smoothly the image scales up from the surrounding environment to the source, providing a

Table 4.1 STARBUGII parameters used in the MIRI photometric point source extractions, applied with STARBUG2−ν0.7.3. A detailed description of each parameter can be found in the STARBUGII documentation.

Parameter	F770W	F1000W	F1500W	F2100W
SIGSKY	1.8	1.8	1.8	1.8
SIGSRC	5.0	5.0	4.0	3.0
SHARP_LO	0.4	0.4	0.225	0.2
SHARP_HI	0.76	0.9	0.53	0.84
ROUND1_HI	0.9	1.0	0.7	0.5
ROUND2_HI	0.6	1.0	0.6	0.6
SMOOTH_HI	0.98	1.0	0.98	-
RICKER_R	2.0	2.0	5.0	5.0
BGD_SIZE	2	10	2	15
CRIT_SEP	8	8	8	8
MAX_XYDEV	3p	3p	3p	3p
MATCH_THRESH	0.15	0.2	0.2	0.25

useful measurement to help determine whether the particular detection is just a bright, dusty ISM region or flux emitted from a genuine point source. Combined, the stringent point-source detection and quality acceptance criteria for STARBUGII ensure reliable astronomical source lists are made for each photometric band.

After using the level-3 mosaics for detection, point-source photometry is conducted on the individual stage-2 data frames, which have more accurate fluxes compared to mosaiced data. Using WEBBPSF (Perrin et al., 2014) version 1.2.1, I generate 5″ PSFs for the four MIRI photometric bands F770W, F1000W, F1500W, F2100W. I subtract the diffuse ISM emission from the single exposures with `starbug2 --background` and perform PSF fitting on these background-subtracted images with `starbug2 --psf`. This routine requires a clean and complete input source list to produce an accurate estimation of the background diffuse emission; any bright spots in the result have arisen from sources in the input image that failed the geometric quality checks provided in Table 4.1. Once complete, all the photometric data from all the exposures for a single photometric band are spatially matched together with `starbug2-match` using the separation threshold MATCH_THRESH values given in Table 4.1 in arcsecond units. Each source must be present in at least three individual exposure source lists; otherwise, it is not considered high enough fidelity. This procedure generates a point-source catalogue for each of the four photometric bands and guards against any artefacts along the frame edges or from cosmic-ray contamination, which may still be present in the data.

4.2.2 Cross-Band and Cross-Instrument Matching

The four MIRI point-source catalogues are merged into a single MIRI source catalogue with `starbug2-match --band`. The matching algorithm uses a simple nearest-match criteria and allows a source detected and extracted with high reliability in some, but not necessarily all bands to be included in the combined MIRI point-source catalogue. For each wavelength of data, I adopt increasing match separation thresholds as each of the individual photometric catalogues with a larger FWHM becomes incorporated into the master catalogue (see Table 4.2). Taking F770W as a base, we match F1000W with a threshold of 0.15″. Similarly, F1500W and F2100W are matched successively with respective separation thresholds of 0.2″and 0.25″. Unmatched sources are appended to the bottom of the table, and the RA/DEC position is taken from the shortest wavelength at which the individual source was detected. This accounts for the different photometric depths achieved with each of the MIRI filters while still maintaining astrometric accuracy.

The next task is to match the MIRI catalogue to the NIRCam PSF photometry catalogue described in Section 3.3. The F770W base of the MIRI catalogue can act as one half of a bridge with the longest available NIRCam wavelength, F444W, as the other half, to combine the MIRI catalogue with the NIRCam catalogue described in Nally et al. (2024). I expect that most F770W detections will also be above the detection threshold in F444W and therefore, match between these two filters with a separation threshold of 0.3″ to limit the likelihood of mismatching sources across the wide wavelength range. However, there is a greater than an order of magnitude increase in the PSF FWHM from the shortest (F115W) NIRCam band to the longest (F2100W) MIRI band. Consequently, there may be compact areas in NIRCam that are blended with MIRI. I assess the impact of blending clusters from NIRCam images to unresolved point sources in MIRI images by defining a metric of clustering. This is the number of sources that appear within the FWHM of each F770W source in shorter wavelengths.

4.2.3 Contamination Corrections

To remove foreground sources, the catalogue is matched to *Gaia* Data Release 3 (Gaia Collaboration et al., 2021) using the same procedure described in Section 3.3.5. No new foreground stars were found in addition to the ones seen

Table 4.2 Properties of each filter used.

Filter Name	Number Sources	Pixel Scale	FWHM [arcsec]	AB-Vegamag Zeropoint
F115W	792424	0.031″	0.040	0.764
F200W	539376	0.031″	0.066	1.686
F356W	184139	0.063″	0.116	2.811
F444W	155326	0.063″	0.145	3.238
F770W	11518	0.11″	0.269	4.384
F1000W	8916	0.11″	0.328	4.956
F1500W	1829	0.11″	0.488	5.839
F2100W	3360	0.11″	0.674	6.532

earlier, likely due to the detection limit of *Gaia* being much higher in the MIRI wavelength range. The mistaken detection of resolved background objects is largely mitigated using the STARBUGII routines described in Chapter 2; any that remain are manually removed by visual inspection in Section 4.3.3.

4.2.4 Photometric Corrections

I correct the photometry for foreground reddening using the *dust_extinction* package (Gordon, 2024). I adopt the value E(B−V) = 0.35 (Tantalo et al., 2022) to correct for the moderate Galactic foreground extinction and apply the extinction curve of Cardelli et al. (1989) assuming $R_V = 3.1$.

Fluxes are measured in *Jy* and first converted to AB magnitudes and then finally to Vega magnitudes using values in the CRDS files (see Table 4.2). All results and photometry are presented in the Vega magnitude system.

4.3 Results and Analysis

4.3.1 Description of Point Source Catalogue

I present the PSF photometry catalogue band-matched across NIRCam and MIRI. I find 922570 unique point sources present in NIRCam images, 19286 in MIRI, and 11338 of which are detected across both NIRCam and MIRI. On publication of this work, the NGC 6822 *JWST* point-source catalogue will be available electronically from the Mikulski Archive for Space Telescopes (MAST)

Table 4.3 Description of point source catalogue columns. All NULL values in floating-point columns are represented as "nan"; other columns do not contain NULL values.

Column Name	Description
Catalogue_Number	The identifying name of the source
RA	Right ascension J2000 (deg)
DEC	Declination J2000 (deg)
Teff	Effective temperature from blackbody fitting (K)
Lbol	Bolometric luminosity from blackbody fitting ($L_\odot$)
F115W	Magnitude in F115W NIRcam filter (Vegamags)
F200W	Magnitude in F200W NIRcam filter (Vegamags)
F356W	Magnitude in F356W NIRcam filter (Vegamags)
F444W	Magnitude in F444W NIRcam filter (Vegamags)
eF115W	Error on F115W magnitude
eF200W	Error on F200W magnitude
eF356W	Error on F356W magnitude
eF444W	Error on F444W magnitude
F770W	Magnitude in F770W MIRI filter (Vegamags)
F1000W	Magnitude in F1000W MIRI filter (Vegamags)
F1500W	Magnitude in F1500W MIRI filter (Vegamags)
F2100W	Magnitude in F2100W MIRI filter (Vegamags)
eF770W	Error on F770W magnitude
eF1000W	Error on F1000W magnitude
eF1500W	Error on F1500W magnitude
eF2100W	Error on F2100W magnitude

Portal and VizieR. Table 4.3 describes the contents and columns in the NGC 6822 point-source catalogue. The source coordinates, RA and DEC, are measured from the shortest wavelength band (and therefore, are the most astrometrically precise) in which a source was reliably detected. Source magnitudes are reported using the Vega system for each photometric band and the associated photometric error is given the column name prefix "e", e.g. filter F770W and error eF770W. The columns Teff and Lbol are effective temperature and bolometric luminosity as measured in Section 4.3.2.

4.3.2 Black Body Fitting

To obtain approximate temperatures and luminosities for the sources in our combined NGC 6822 NIRCam and MIRI catalogue, I fit each of their SEDs with

a blackbody model (Eq. 4.1),

$$F_\nu(A, T_{\rm eff}) = A\frac{2h\nu^3}{c^2}\frac{1}{e^{\frac{h\nu}{k_b T_{\rm eff}}} - 1}, \tag{4.1}$$

where $F_\nu(A, T_{\rm eff})$ is the flux at frequency ν for a star with effective temperature $T_{\rm eff}$. Scale factor A scales the model linearly to account for distance, the speed of light c, the Boltzmann constant k_B and the Planck constant h. Values for A and $T_{\rm eff}$ are varied freely, to minimise the χ^2 value, with *scipy.optimise.minimise*, measured between the SED photometric points and blackbody flux in linear space. To obtain estimates for the effective stellar temperature, I require that a source must have been detected in at least four of the eight photometric bands to provide sufficient constraints on the SED. This constraint results in 123761 sources in the *JWST* catalogue with valid temperature fits. The star's bolometric luminosity $L_{\rm bol}$ was then calculated by integrating the blackbody formula with each scale factor A and effective temperature $T_{\rm eff}$. The effective temperature and stellar bolometric luminosity estimated from the blackbody fits are given in the *JWST* NGC 6822 point-source catalogue described in Table 4.3. These typically correspond to brighter objects in our catalogue, with temperatures determined to an approximate completeness of F200W ~22.5, around ~0.5 magnitude below the RC. The resulting H–R diagram of the 123761 fit sources is shown in the greyscale density map on Figure 4.1. It can be seen that the RGB is accurately traced in the contours and AGB stars, based on forthcoming results from Section 4.3.4, are positioned above the TRGB where expected.

There are two important caveats to obtaining well-defined estimates of the effective temperature and luminosity of the sources using this method. First, hot (blue) stars exhibit blackbody emission that peaks at shorter wavelengths than any of the NIRCam filters. The peak of F_ν in Equation 4.1 occurs at wavelength λ satisfying the relation $\lambda T = 5099.3\ \mu$mK as described by (Zhang & Wang, 2010). Thus, any source with $T_{\rm eff}$ hotter than ~4500K, will have SED peaks in the UV or optical, outside of the photometric range covered by the *JWST* photometry and will exhibit progressively worse SED fits as $T_{\rm eff}$ increases. The sources with the best constrained $T_{\rm eff}$ in our NGC 6822 sample correspond to K- and M-type stars which peak in the near-IR. The second caveat is that if a particular source has an IR excess, caused by emissions from circumstellar dust around AGB stars or a circumstellar disk or envelope in YSOs, it will diverge from a simple blackbody-like SED, and therefore, the integrated blackbody fit will overestimate the luminosity values. For sources with circumstellar material,

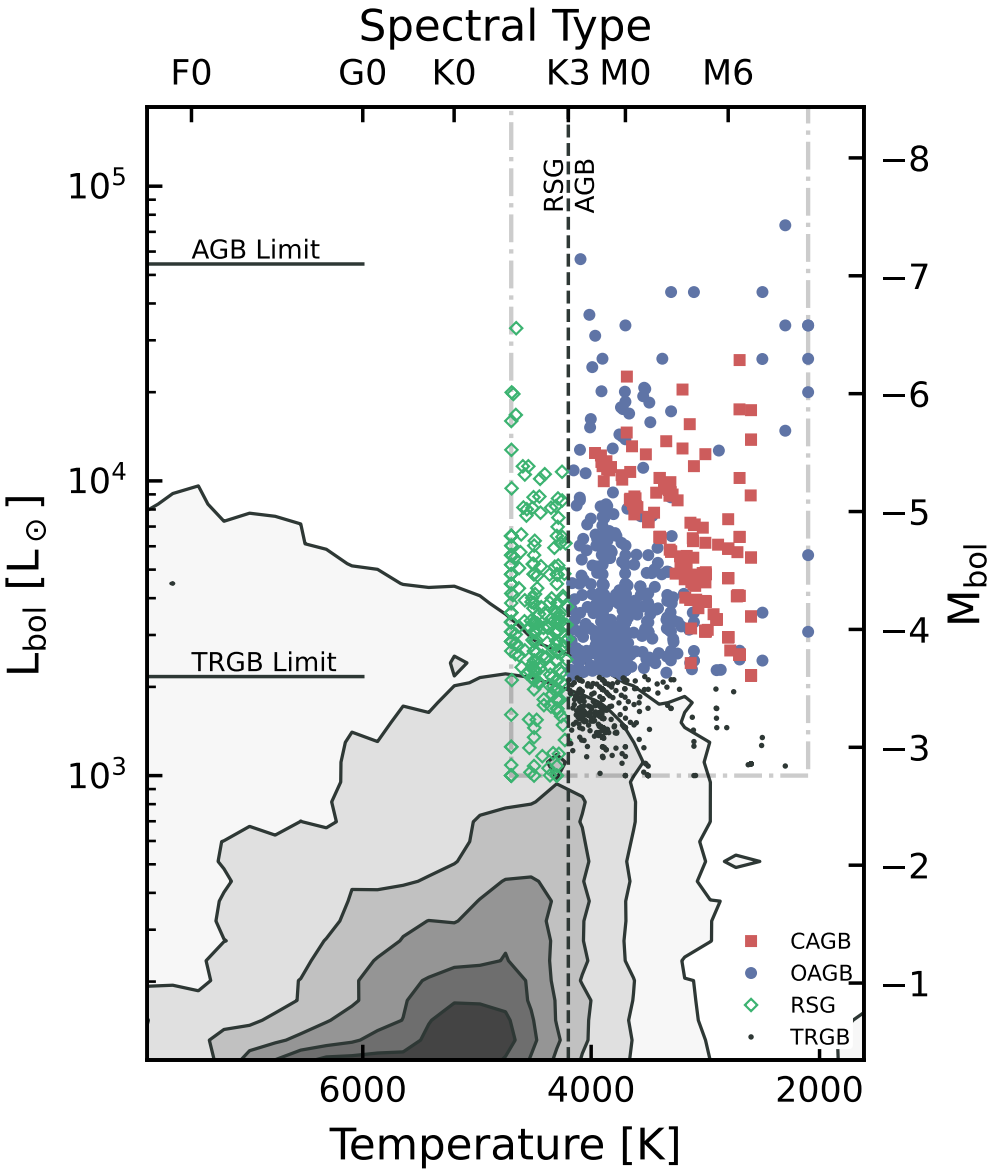

Figure 4.1 H-R diagram of the central bar of NGC 6822. The x axis shows the source's effective temperature (T_{eff}) and the y axis shows the bolometric luminosity (L_{bol}) in solar luminosity units on the left and the corresponding bolometric magnitude on the right. The underlying contour map displays the blackbody temperature and luminosity of all point sources in the full NGC 6822 catalogue, as produced in Section 4.3.2. Darker colours represent a greater density of stars. Blue circles are OAGBs, and red boxes are CAGBs. The grey dot-dashed line shows the bounds of the GRAMS model parameters. Horizontal lines at $M_{bol} = (-3.6, -7.1)$ show the classical TRGB limit and AGB limit, respectively. The dashed vertical line at 4200K (K3III star) shows the separation between AGBs and RSG stars.

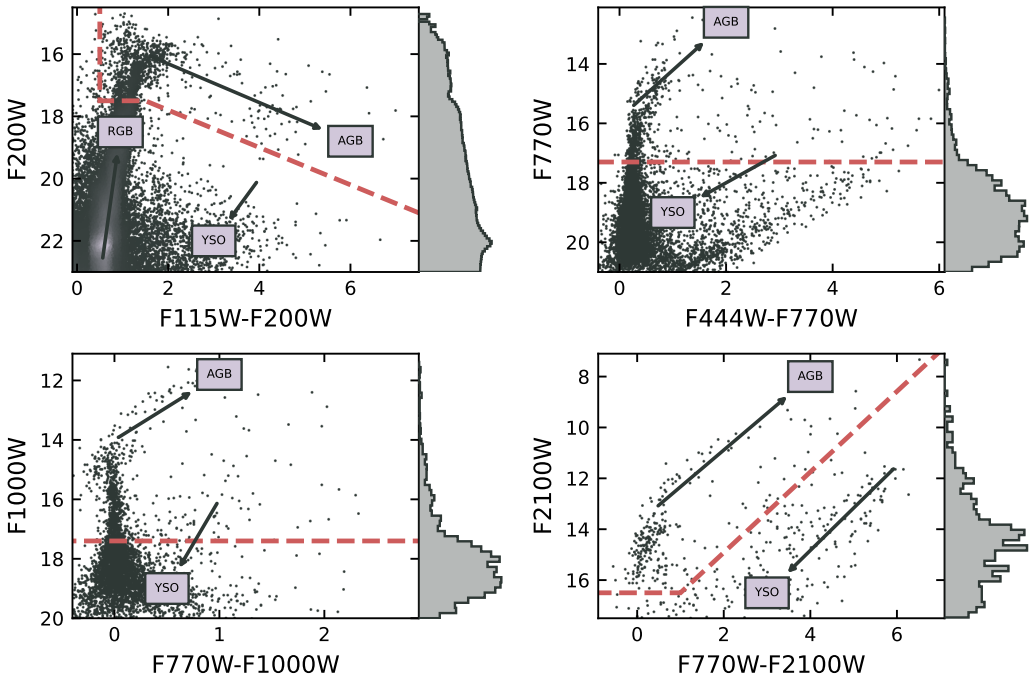

Figure 4.2 NGC 6822 CMDs displaying evolved star candidate selection boundaries. Four colour combinations are presented: F200W vs F115W-F200W, F770W vs F444W-F770W, F100W vs F770W-F1000W, F2100W vs F770W-F2100W. Selection boundaries overlaid in red and numerical values for selections quoted in Table 4.4. The distribution of magnitudes are represented with the histograms on the right; the upper left panel shows this on a log scale due to the large number of sources, while the rest are scaled linearly. The general trajectory of evolution for the key populations (AGB, YSO, RGB) are labelled.

I improve upon these luminosity estimates in Section 4.3.4, where I conduct more detailed modelling of the AGB stars identified in our sample. For modelling of YSOs in NGC 6822 and their best-fit parameters, see Section 4.3.5 and Lenkić et al. (2024).

4.3.3 Selecting Evolved Star Candidates

Due to the limitations in modelling dusty evolved star SEDs as blackbodies, I use colour-magnitude cuts in the *JWST* point-source catalogue to build an inclusive list of evolved star candidates. The TRGB provides a practical limit for defining these cuts. Guided by TRGB measurements and source classification for NGC 6822 made in Chapter 3, I define a series of NIRCam and MIRI colour cut boundaries displayed in Figure 4.2 (see Table 4.4). To be included in our

Table 4.4 Evolved star colour-cut selection criteria. For each colour-magnitude combination, the coordinates in (colour,magnitude) pairs are given. Sources above these boundaries are included in the list of evolved star candidates.

Colour Combination	Boundary Coordinates
F115W-F200W vs F200W	(0.5,17.5) (1.5,17.5) (9.0,22.0)
F444W-F770W vs F770W	(-0.5,17.3) (7.0,17.3)
F770W-F1000W vs F1000W	(-0.5,17.4) (3.0,17.4)
F770W-F2100W vs F2100W	(-1.0,16.5) (1.0,16.5) (7.0,7.0)

provisional NGC 6822 AGB star candidate selection, a point source must satisfy at least one of these colour criteria. The first panel shows F115W-F200W vs. F200W, where minor differences in the temperature of the evolved stars are traced well due to the filter combination straddling the blackbody peak for the expected temperature range. In this combination, I draw a horizontal cut at the TRGB F200W ~17.5 and slope down from (1.5, 17.5) to (9.0, 22.0) as dust extinction causes the more extreme sources to drop below the TRGB. The second and third panels show F444W-F770W vs F770W and F770W-F1000W vs F1000W, respectively. In both cases, I draw the boundary slightly below the TRGB F770W~17.3 and F1000W~17.4 and keep all sources above these limits. Finally, in the last panel, F770W-F2100W vs F21000W, I place a diagonal boundary between the expected separation of AGB stars and YSOs shown by Jones et al. (2017b).

These cuts are deliberately liberal and are not designed to isolate AGB stars perfectly, but instead capture a complete list of all evolved stars, potentially at the expense of over-selecting other sources that occupy a similar colour space. These contaminations may include dust-accreting YSOs, unresolved star-forming galaxies in the background, or post-AGBs (Jones et al., 2017a).

In total, 1480 sources in the *JWST* NGC 6822 point-source catalogue have at least four photometric flux measurements and fulfil at least one of the evolved star colour cuts. These sources make up the provisional NGC 6822 evolved star candidate list.

Using the high spatial resolution of the NIRCam images, I can visually inspect the sources for any resolved background galaxies which may still be present in our catalogue. Resolved background galaxies with compact, point-like cores can appear morphologically similar to dust-embedded sources in the STARBUGII

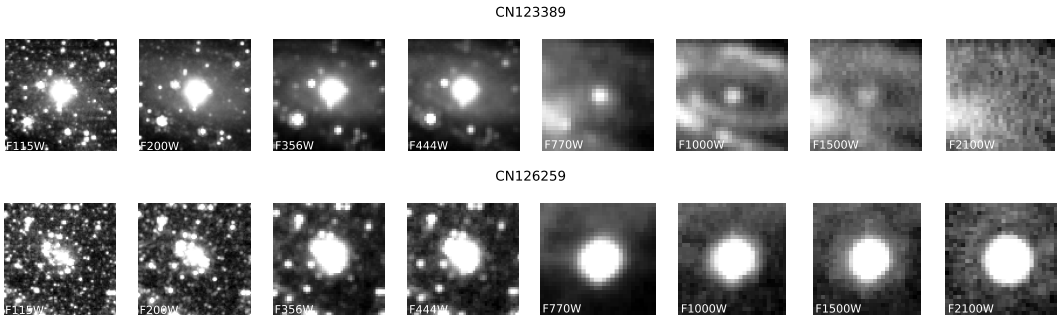

Figure 4.3 Zoom-in images of two contaminating sources in the provisional evolved star candidate selections, across the eight *JWST* mosaics, increasing in wavelength from left (F115W, 1.15μm) to right (F2100W, 21μm). The upper row shows source CN123389, a spiral galaxy with a point-like core. The lower row shows source CN126259, which exhibits a point source in the MIRI images but is resolved, revealing a cluster of stars in the NIRCam data.

detection routine. For example, the upper panel of Figure 4.3 shows a galaxy with a compact point-like nucleus, which has resolved structure due to its elongated disk and dust lanes that are visible in specific wavelengths.

The spatial resolution of the MIRI images is >0.638 pc at the distance of NGC 6822, while NIRCam is <0.344 pc. Therefore, the larger PSF associated with MIRI images may cause stars in clusters to become blended into a single point-like object at longer wavelengths. The lower panel of Figure 4.3 shows one such object, which appears point-like in all MIRI images, even exhibiting PSF wings. With the resolving power of NIRCam, I can disentangle this object into a resolved cluster comprised of several stars and discount them.

The provisional NGC 6822 evolved star candidate list contained 56 objects that fell into one of these two categories. These objects are removed from the sample of evolved stars.

4.3.4 Dusty Mass-Loss Model Fitting

Thermally-pulsing AGB stars are reliable producers of large quantities of dust, with extreme sources undergoing a superwind and losing mass at a rate of 10^{-4} $M_{\odot}yr^{-1}$ (Vassiliadis & Wood, 1993). The quantity of dust production, the rate of evolution and the type of dust grain growth are inextricably linked to the chemistry in the circumstellar envelope of the AGB star. Molecular and dust signatures in the spectra of the star can be traced with well-sampled SEDs (Jones

et al., 2017b). Following a similar methodology to Riebel et al. (2012), Srinivasan et al. (2016) and Jones et al. (2018), I fit the SEDs of the NGC 6822 evolved star candidates with a grid of evolved star models to confirm their evolutionary status, chemically classify them into C- and O-rich stars, and measure their dust production rates.

The photometric data from each of the 1424 colour-selected evolved star candidates in NGC 6822 are fit to the 80843 model SEDs from a Grid of RSG and AGB radiative transfer models (GRAMS). This grid is split between carbon-rich (Srinivasan et al., 2011) and oxygen-rich (Sargent et al., 2011) sets, computed with the 2Dust radiative transfer code (Ueta & Meixner, 2003) and stellar photosphere models for carbon-rich (Aringer et al., 2009) and oxygen-rich (Kučinskas et al., 2005, 2006) stars. The O-rich dust is modelled using astronomical silicates (Ossenkopf et al., 1992). For C-rich stars, a combination of amorphous carbon (90%) and silicon carbide (10%) is used. The models were computed for representative metal-poor stars Z~0.5 $Z_{\odot}$ in the Magellanic Clouds (Bernard et al., 2008), which have comparable metallicities to NGC 6822. O-rich models are prepared from an input grid by Sargent et al. (2011) with effective temperature ($T_{\rm eff}$) ranging between 2100-4700 K, optical depth at 10μm (τ_{10}) between 10^{-4} – 26.0 and dust shell inner radius ($R_{\rm in}$) from the set 3, 7, 11, 15 $R_{\rm star}$, resulting in a bolometric luminosity ($L_{\rm bol}$) ranging from 10^{3} – 10^{6} $L_{\odot}$ for the whole O-rich grid. The C-rich models are generated by Srinivasan et al. (2011) are from 2600≤ $T_{\rm eff}$ ≤4000 K, optical depth at 11.3μm ($\tau_{11.3}$) between 10^{-3} – 4.0 and $R_{\rm in}$ from 1.5, 3, 4.5, 7, 12, resulting in 1100≤ $L_{\rm bol}$ ≤ 26000 $L_{\odot}$. The C-rich models also introduce the parameter $C2O$, representing the surface carbon-to-oxygen ratio, from the set 1.4, 2, and 5. The O-rich grid holds this value at 0. Dust mineralogy is fixed and not varied in the grid. These parameters provide key values to establish the evolutionary stage and chemical type of the sample of NGC 6822 evolved star candidates.

Each NGC 6822 candidate is compared against every model SED (i) in the grid, measuring the quality of fit between the observed photometric points and the GRAMS models. For the SED fitting, I convolved these models with the *JWST* filters. I then scale the model flux F_{ν} values by a factor A, correcting for the adopted distance to NGC 6822 (490 kpc) from the LMC distance (50kpc), where the models are generated. Due to the non-linear nature of the SED flux data, a χ^2 is not appropriate to use as a quality of fit metric; instead, I measure reduced χ^2 per photometric point (χ^2 over the number of flux measurements) as outlined by

Srinivasan et al. (2016). This value is hereafter referred to as χ^2_i, where i denotes each model SED index, thus creating a distribution of quality of fits across the set of model SEDs. Stars whose lowest χ^2_i (best fitting model) is greater than 10^4 are marked as clear contaminants in the source list and will be removed. Each model in the grid has a likelihood given by $\mathcal{L}_i \propto w_i = e^{-0.5\chi^2_i}$, which, with flat priors, is proportional to its posterior probability. By using these probabilities as weights, a weighted mean of model outputs naturally combines information from all plausible models, giving more influence to better-fitting models while accounting for uncertainty in which model is "correct."

The grid parameters key to this research are T_{eff}, L_{bol}, and dust production rate (DPR). For each model parameter (x) and evolved star candidate, I perform a weighted average of the SED model fits to obtain representative values of the physical properties. I take a weighted mean of parameter x with Equation 4.2 using the probability density function and take a weighted standard deviation on that measurement with Equation 4.3

$$\bar{x} = \frac{\sum w_i x_i}{\sum w_i}, \tag{4.2}$$

$$\sigma = \sqrt{\frac{\sum w_i (x_i - \bar{x})^2}{(n-1)\sum w_i}}, \tag{4.3}$$

where n is the number of models. This approach takes into account every model in the grid, and the weight of their contribution to the final average is represented by how well they fit the SED. In doing so, I can sample from the grid with a finer resolution than the grid itself, and values are not trapped in potentially local minima in the χ^2 fitting parameter space.

Figure 4.4 shows the SEDs and best-fitting GRAMS models for four example sources. The figure panels display the photometric points as black diamonds, with lines indicating the 100 "best-fitting" models (for illustrative purposes), where carbon-rich models are shown in red and oxygen-rich models in blue. The model with the lowest χ^2 is shown in a solid black line, and a dashed line represents the best blackbody fit. The upper left panel shows the dusty star CN60364 with well-fitting carbon-rich models. The upper right panel shows CN102234, a dust-

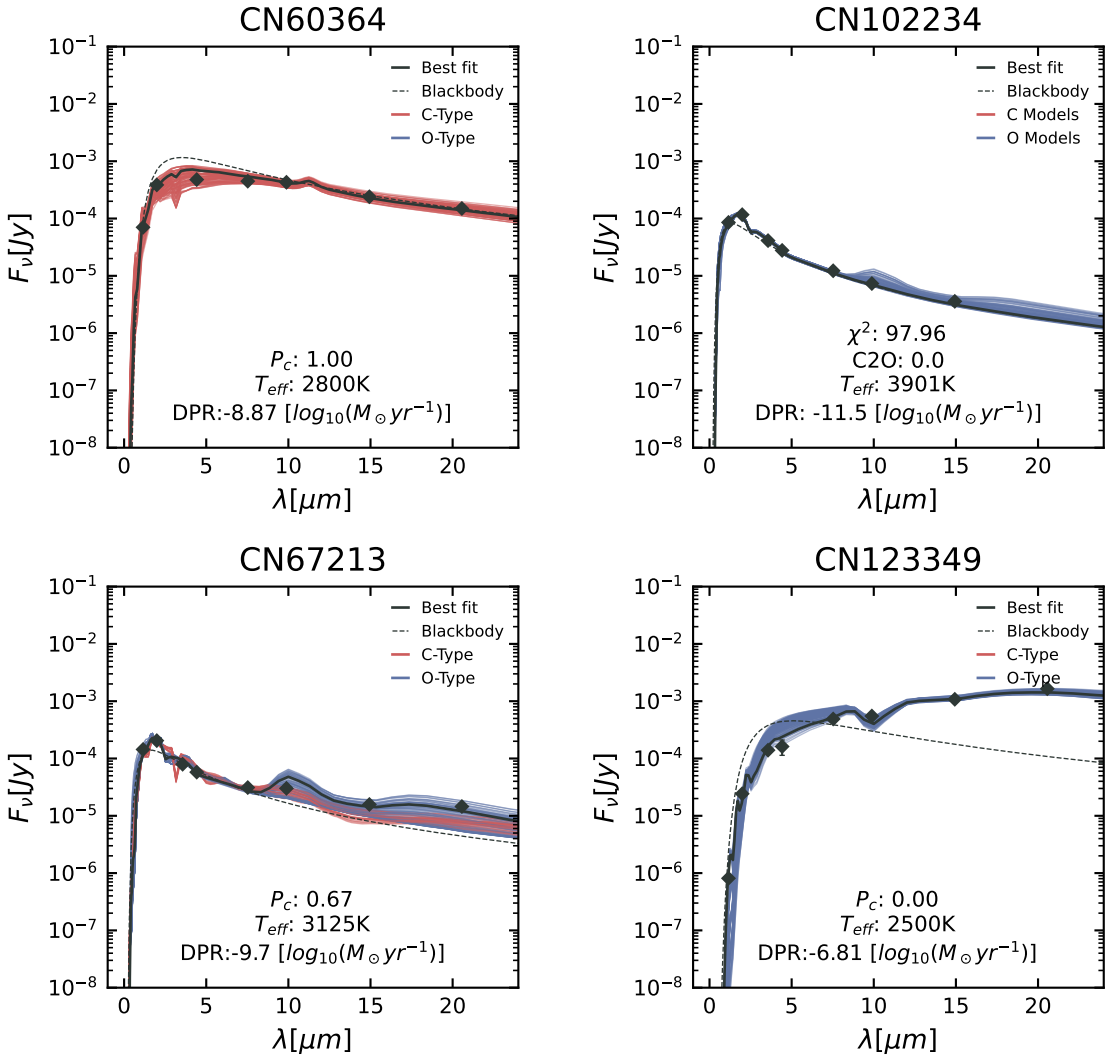

Figure 4.4 Four examples the GRAMS model fitting to the NGC 6822 evolved sources. All figures show the top 100 best-fitting GRAMS models to a particular source's SED (black diamonds, errors on flux shown where visible). Red lines indicate models from the set of carbon-rich models, while blue lines are from the set of oxygen-rich models. The black solid line indicates the best model and the dashed line shows the best blackbody calculated in Section 4.3.2.

Table 4.5 Description of the table containing the results of the GRAMS model fits to the NGC 6822 evolved star candidates.

Column Name	Description
Catalogue_Number	Unique source identifier
Teff	Effective temperature (K)
Lbol	Bolometric luminosity ($L_\odot$)
DPR	Dust production rate ($M_\odot yr^{-1}$)
P_C	Probability of being a carbon star
class[a]	Spectral classification
eTeff	Standard deviation on Teff
eLbol	Standard deviation on Lbol
eDPR	Standard deviation on DPR

[a] Values described in Section 4.3.6.

free star. The lower left panel displays CN67213, a moderately dusty source with a range of both carbon-rich and oxygen-rich models that fit well. Finally, the lower right panel shows the source CN123349, which exhibits a significant infrared excess and has the most extreme dust production rates in the entire sample (discussed in Section 4.4.2).

Results from the GRAMS model fitting are described in Table 4.5. The unique identifier of the source is given in the column "Catalogue_Number" and can be matched to Table 4.3. The effective temperature (T_{eff}), bolometric luminosity (L_{bol}) in $L_\odot$ units, dust production rate (DPR) in $M_\odot yr^{-1}$ units as measured by the weighted mean of fit parameters are given in separate columns. The L_{bol} and T_{eff} columns are more accurate than the values determined during blackbody fitting, and should be used over these when available. The weighted standard deviation of these values is provided in the columns with the prefix 'e'. The chemical classification, which is presented as the probability of being a carbon star (P_C), and the spectral classification "class" are both discussed in Section 4.3.6.

4.3.5 Removing YSO contaminants

Evolved stars are not unique in their colour space in infrared CMDs. Contaminants include YSOs, unresolved background galaxies, and planetary nebulae, all of which have rising SEDs that are bright in the mid-IR (Jones et al., 2017b; Nayak et al., 2024a; Habel et al., 2024; Lenkić et al., 2024). The colour cut selections described in Section 4.3.3 are designed to limit the number of these sources in our evolved star candidate list.

Visually inspecting the sources limits contamination from clearly resolved objects, as described in Section 4.3.3. However, removing contaminant YSOs is a more challenging process, as they appear as point sources in the *JWST* images. YSO SEDs are typically more steeply rising in mid-IR wavelengths, but this is also exhibited by particularly extreme dust-producing AGBs (Jones et al., 2017b; Nayak et al., 2024a; Habel et al., 2024). To remove these, I fit each source in the evolved star catalogue with the "spubhmi" model YSO SEDs from Richardson et al. (2024). These are the model SEDs from Robitaille (2017) convolved to the *JWST* filter throughput functions. Similar to the GRAMS SED fits discussed above, the SED fitter provided by Robitaille et al. (2007) tests the observed photometry against every model in the "spubhmi" model set, where the visual extinction A_V is the single free parameter, and returns a χ^2 per photometric point value for each as a goodness-of-fit metric ($\chi^2_{\rm YSO}$; see Robitaille et al., 2007). This method has been applied by Lenkić et al. (2024) in the central star-forming region of NGC 6822, Spitzer I. Here, I have expanded this to the full *JWST* footprint, but only for stars that pass the "evolved star colour cuts".

The results of the YSO and evolved star fitting can be compared with the Akaike Information Criterion (AIC). This provides provides a principled way to balance model fit quality against model complexity. It is defined as: AIC = $2{\rm k} - 2\ln\mathcal{L}_{\rm max} = \chi^2 + 2{\rm k}$, where $\mathcal{L}_{\rm max}$ is the maximised likelihood and k is the number of free parameters in the model fitting. The first term rewards models that fit the data well (low χ^2), while the second term penalises models with more parameters. This makes AIC particularly well-suited for comparing results from two different model-fitting routines that may not use the same methods. By comparing the fits on a common value, AIC allows for the judgement of which routine achieves a better quality of fit, rather than simply which one produces the lowest χ^2.

Figure 4.5 illustrates this comparison, where points located to the left of the figure indicate good evolved star GRAMS model fits, and points positioned at the bottom indicate good YSO fits. The black dashed line follows the $\rm AIC_{YSO} = AIC_{AGB}$ relation, such that any sources appearing above the line exhibit SEDs more characteristic of evolved stars than YSOs. However, I do not treat the boundary as absolute; I highlight the population of objects with ambiguous evolutionary status that fall under $\Delta{\rm AIC} \leq 0.5$. These sources are kept as tentative evolved objects, as they may exhibit extreme dust-producing properties. The blue squares represent the sources that show the resolved structure in visual inspection of the *JWST* images (see Section 4.3.3), these are included to demonstrate the

effectiveness of this method at segregating evolved stars from both contaminants.

In total, of the 1424 selected from the complete NGC 6822 source list, 1236 are better fitting evolved stars than YSOs. A further 14 exist close to the boundary and are also included in the final evolved star list (totalling 1250 candidates).

4.3.6 Evolved Star Classification

All potential contaminating sources in the evolved star catalogue are now removed, leaving a reliable list of evolved sources. I classify the evolved sources into one of four categories: oxygen- or carbon-rich AGBs, stars on the RSG, and stars fainter than the theoretical TRGB (henceforth simply TRGB). Their temperature and luminosity, as fit by the GRAMS models, are overlaid onto Figure 4.1 in green (RSG), blue (OAGB), red (CAGB), and black (TRGB). An overview of the classifications can be seen in Table 4.6.

The first separation is between RSG and AGB stars. The oxygen-rich GRAMS models do not distinguish between OAGB and RSG stars, so a straight cut at $T_{\rm eff} = 4200K$ from the GRAMS fit can be applied to separate these populations. A star hotter than this limit has a spectral type of $K3$ or above; I consider these stars to be on the RSG branch, as seen in Sibbons et al. (2012),Hirschauer et al. (2020) and Tantalo et al. (2022). I overlay this boundary as the dashed line on Figure 4.1. In total, I classify 261 stars as RSGs, which span the full luminosity range of AGB stars. It would be expected that several RSGs with luminosities greater than $M_{\rm bol} = -7.1$ are seen (Wood et al., 1983), as these are known to exist in NGC 6822 (Massey, 1998; Levesque & Massey, 2012; Patrick et al., 2015; Hirschauer et al., 2020; Antoniadis et al., 2025), however, saturation in the NIRCam images limits the number of these bright source detections.

The TRGB represents the final stage of evolution along the RGB, as described in Chapter 1. The TRGB magnitude is independent of the stars' initial mass and varies slightly with stellar metallicity, the effect of which can be calculated with Equation 4.4 (Sweigart & Gross, 1978; Salaris & Girardi, 2005)

$$M_{\rm bol}^{\rm TRGB} = -0.19[{\rm Fe/H}] - 3.81\,. \tag{4.4}$$

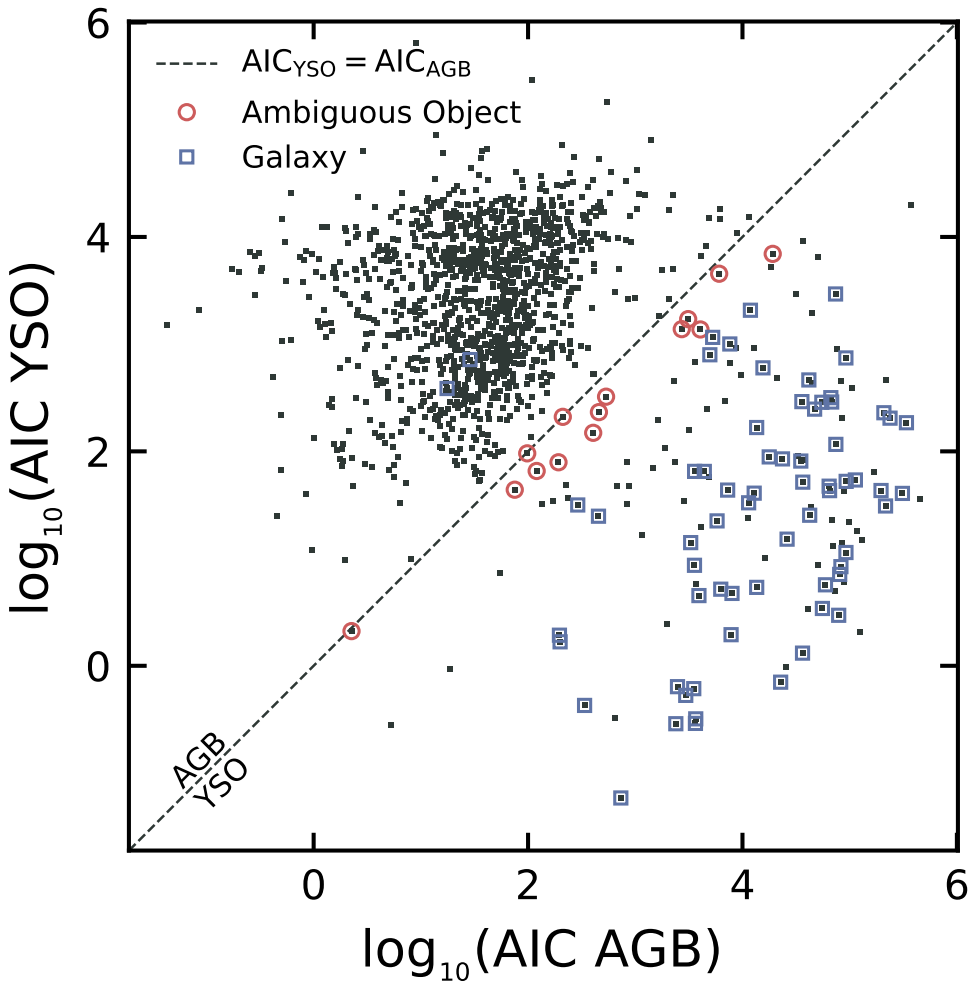

Figure 4.5 Comparison between evolved star x axis and YSO y axis model quality of fit for each source. The blue boxes represent sources identified as resolved background galaxies. The black dashed line shows the $\mathrm{AIC_{YSO}} = \mathrm{AIC_{AGB}}$ relation; sources above this line exhibit SEDs more characteristic of an evolved star. Red circles represent sources that fall within $\Delta\mathrm{AIC} \leq 0.5$ of this line and may still be dust-enshrouded, variable, evolved stars with more extreme properties. Spectroscopic information is required to confirm the true evolutionary nature of these objects.

The mean bar metallicity of NGC 6822, (logarithmic) [Fe/H]=-1.05, as estimated from the old population (Kirby et al., 2013), therefore, $M_{bol}^{TRGB} = -3.61$. Early AGB stars and RGBs have dust-free photospheres that can be fit by some models in the GRAMS grid, as they have spectral types similar to those used to construct the models (Sargent et al., 2011). To distinguish between the AGB and RGB population, I take a luminosity cut at $M_{bol} = -3.61$ in the H-R diagram. There are 618 AGB stars in our sample that exceed this limit and are cooler than 4200 K, while 371 stars fall below the TRGB.

Finally, the AGBs are separated into two chemical classes, OAGB and CAGB. Unlike the other parameters in the GRAMS models such as T_{eff} or DPR, the chemical classification is a binary choice between carbon-rich and oxygen-rich circumstellar envelopes. If the best-fit models comprise models of both chemistries, then a mechanism is required to assign a chemical classification to the star.

I define the property P_C as the probability that a given source is carbon-rich. Using the probability density function across all model fits for each source, I compute the weighted mean (Equation 4.2) over the model chemical types. Oxygen-rich models are assigned a value 0 and carbon-rich models a value 1, such that the resulting weighted mean lies between 0 and 1. Sources whose fit-quality weights are dominated by carbon-rich models therefore have high P_C values, while sources predominantly well-fitting oxygen-rich models have low values of P_C.

192 AGBs have $P_C > 0.5$ so are considered CAGB, and 426 OAGBs have $P_C < 0.5$. In Figure 4.1, CAGB sources are plotted in red, OAGB in blue.

Previous infrared surveys of evolved stars and their dust-production measurements in Local Group galaxies (e.g., Srinivasan et al., 2009; Riebel et al., 2012; Jones et al., 2017b) use the concept of the "best-fitting" model SED to determine the chemical type of the AGB star. In this work, I average across a larger number of models to probe the probability space of stellar properties. However, this may result in sources which I classify one way, but the best-fitting model suggests the alternative classification. By comparing the relation between P_C and the chemical class of the best-fitting model, I find that all classified oxygen-rich stars have a best-fitting oxygen model, but 10% of stars classified as carbon-rich have a best-fitting oxygen model. The remaining carbon-rich stars all have carbon-rich best fits.

Figure 4.6 shows the distribution of χ^2 values from the fitted SED models to a

particular source CN118456, which illustrates the potential issue with classifying the chemical type of a star from the best-fitting model SED. The red line (which has been smoothed with a Gaussian kernel density estimate) shows the distribution of carbon models, and the blue shows oxygen-rich models. It can be seen in the distributions that the bulk of the best-fitting models is weighted towards a carbon classification; however, the single best SED is with an oxygen model. This is potentially due to a local minimum in the χ^2 distribution, which happens to coincide with one single model. By constructing the probability density function from χ^2 values as described above, I can provide a more accurate estimate of the probability that a source belongs to a particular chemical classification. In the case of CN118456, I find that it has a $P_C = 0.87$ and is therefore most likely to be carbon-rich.

4.4 Discussion

4.4.1 Carbon Star Luminosity Function

The luminosity function of C-rich stars provides a key insight into the third dredge-up of AGBs, which is influenced by nucleosynthesis, surface chemical enrichment, and mass loss (Marigo et al., 1999). The carbon star luminosity function typically peaks around a bolometric magnitude of $M_{bol}\sim -4.5$ to -5.0, a range set by the underlying core mass-luminosity relation for AGB evolution (Paczyński, 1970; Iben & Renzini, 1983), with variations produced by differing mass and metallicity of the progenitor stars (Marigo et al., 2008). Third dredge-up efficiency in $\sim 1.5 - 4$ $M_\odot$ AGBs determines the luminosity at which a star can become carbon-rich. High efficiency dredge-up in low-mass cores allows for more stars to become CAGBs earlier and exhibit lower bolometric luminosities (Karakas et al., 2002). This is expected to be the case in lower metallicity environments, such as NGC 6822, as fewer third dredge-up events are required to raise the surface chemistry of the star C/O>1 (Marigo et al., 1999; Groenewegen, 2006; Marigo et al., 2008). Alternatively, in a higher mass case, CAGBs may reach $M_{bol}\sim -6.0$ during late-stage superwind; however, this is a short-lived phase (~500 years) and so these are statistically rare (Vassiliadis & Wood, 1993; Höfner & Olofsson, 2018). Observationally, the luminosity function peak reflects not only the physics of stellar interiors but also the cumulative effects of star formation history, selection biases, and circumstellar dust obscuration that

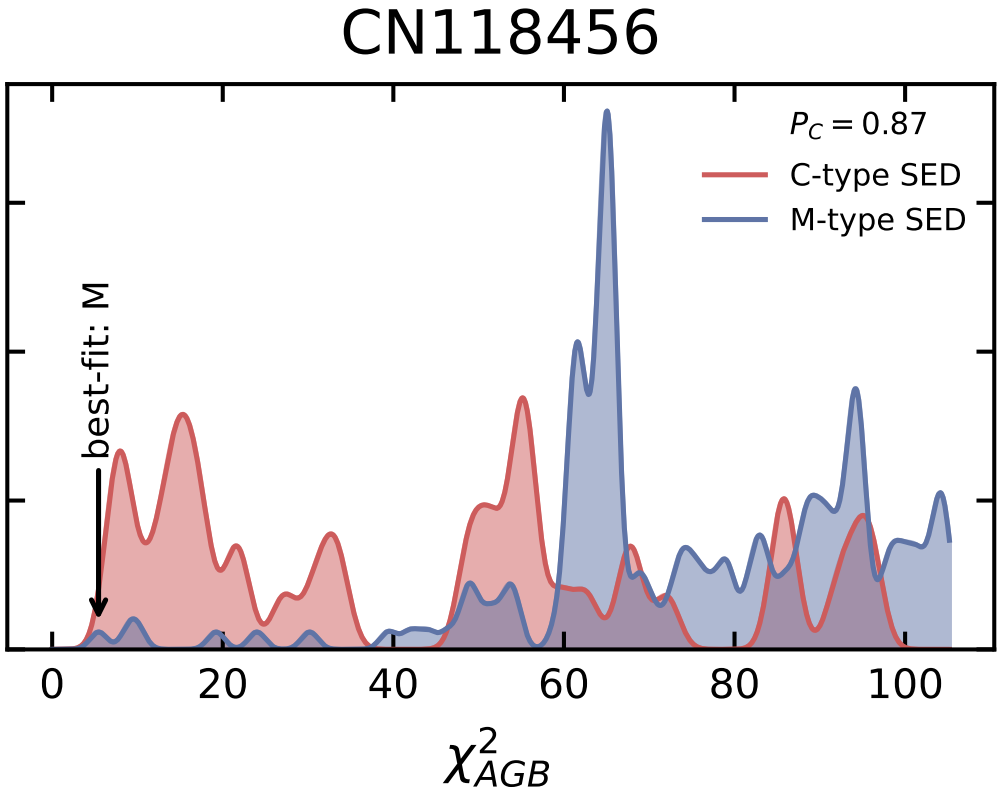

Figure 4.6 Distribution of χ^2 values from fitting carbon (red) and oxygen (blue) model SEDs to a single source. Of the top 70 best fit models (with $\chi^2 < 40$) 90 percent are carbon-rich, yet the single best-fitting GRAMS SED is oxygen-rich. This source would therefore be classified as O-rich by Srinivasan et al. (2009); Riebel et al. (2012); Jones et al. (2017b) but our classification method assigns it a probability of $P_C = 0.87$ and thus we classify this object as C-rich.

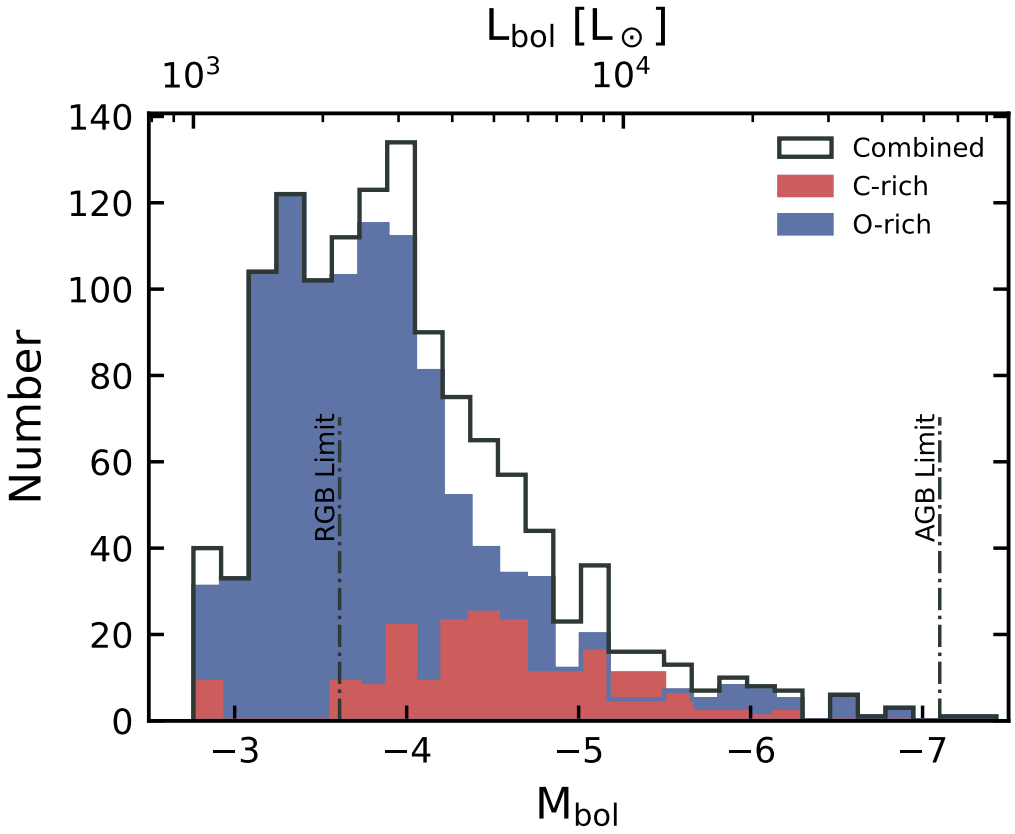

Figure 4.7 Luminosity function of the evolved stars in NGC 6822. The distribution of carbon-rich stars is shown in red and modelled as a Gaussian with the dashed line. All M-type sources (OAGB, RSG, TRGB stars) are shown in blue, and the cumulative distribution is overlaid in black. The classical RGB and AGB limits are shown.

influence which stars are detected and measured (Cioni et al., 2006b).

The luminosity function of the evolved star population of NGC 6822 is shown in Figure 4.7, for both the C-rich and O-rich (OAGB, RSG, TRGB) stars. Although C-rich AGBs are rarely observed to exceed $M_{bol} = -6.0$, theoretically the limit is closer to $M_{bol} = -6.4$ (Iben & Renzini, 1983). Above this threshold, stars are massive enough (~4 $M_\odot$) to trigger HBB, where the convective envelope touches the hydrogen burning shell (Boothroyd & Sackmann, 1992). Temperatures reach $\sim 30 \times 10^6 K$ at the base of the convective envelope, preventing the continued dredge-up of carbon and instead converting it to nitrogen through the CNO cycle (Ventura & D'Antona, 2005), thus setting an upper mass-limit on CAGBs. The brightest CAGB in the sample occurs at $M_{bol} = -6.3$ ($L_{bol} = 26,000$ $L_\odot$). I find three CAGBs brighter than $M_{bol} = -6.0$ observational ceiling. The median

CAGB $\bar{M}^{C}_{bol} = -4.48 \pm 0.6$ is consistent with the value measured from the catalogue of C-rich Miras in NGC 6822 produced by Whitelock et al. (2013, 2014), ($M_{bol} = -4.54$) assuming the distance modulus of 23.45. Similarly, Srinivasan et al. (2016) finds the carbon-star luminosity function in the SMC peaks at the same $M_{bol} = -4.5$. These two galaxies have similar metallicities; therefore, the dredge-up efficiency is comparable between the two populations, resulting in the carbon-star luminosity functions peaking at the same point. This is in spite of the two galaxies having differing star-formation histories, which would alter the progenitor mass of CAGBs. However, both galaxies have experienced active star formation within the last $\sim 1-6$ Gyr (Harris & Zaritsky, 2004; Fusco et al., 2014), accounting for a significant proportion of the low- to intermediate-mass CAGB stars visible today.

In terms of the full luminosity function distribution, the sample contains two oxygen-rich sources brighter than the classical AGB limit of $M_{bol} = -7.1$. This represents the luminosity, during steady hydrogen-shell burning, associated (through the core-mass luminosity relation Wagenhuber & Groenewegen (1998)) with a core mass exceeding the Chandrasekhar limit and igniting the degenerate helium core (Iben & Renzini, 1983; Vassiliadis & Wood, 1993). Instead, these stars are potentially RSGs (Hirschauer et al., 2020; Antoniadis et al., 2025), TP-AGBs that are highly evolved and undergoing a thermal pulse, momentarily pushing them above the classical brightness limit (Lattanzio & Wood, 2004), or finally, they may be higher mass (8-10$M_{\odot}$) "super-AGBs" that bridge the evolutionary gap between AGBs and RSG (Siess, 2006).

4.4.2 Evolved Star Dust Production

The luminosity and, consequently, the radiation pressure of an AGB star evolving through the thermally pulsing stage will increase, allowing for higher rates of mass loss to occur (Vassiliadis & Wood, 1993; Bloecker, 1995). Earlier in the evolution of AGB stars, the density of the stellar wind is too low for efficient dust grain growth, resulting in negligible IR excess (Höfner & Olofsson, 2018). Observations of AGBs in the Magellanic Clouds have shown that this produces a distinct dusty population above a threshold DPR $\geq 10^{-11.3}$ $M_{\odot}yr^{-1}$ (Boyer et al., 2012; Riebel et al., 2012; Srinivasan et al., 2016). Using the DPR values from the GRAMS models, I find that this broadly agrees with these observations. Figure 4.8 shows the measured DPR in units $\log_{10}$ $M_{\odot}yr^{-1}$ versus M_{bol} for the NGC 6822

Table 4.6 Dust production by evolved stars in NGC 6822. The total number of each class is provided, along with the number of sources with DPR $\geq 10^{-11.3}$ and their cumulative DPR. AGB stars are given as an independent measure, as well as their chemically separated subtypes.

Stellar Classification	Number	Sources with DPR $\geq 10^{-11.3}$	Total DPR [$M_\odot yr^{-1}$]	Percentage of Total DPR
AGB	618	383	5.3×10^{-7}	95
CAGB	192	181	1.9×10^{-7}	35
OAGB	426	202	3.4×10^{-7}	60
RSG	261	63	7.5×10^{-9}	1
TRGB	371	109	2.4×10^{-8}	4
Total	1250	555	5.6×10^{-7}	

evolved star sample. A histogram of binned DPR values for oxygen (blue) and carbon (red) dust is shown in the upper panel. Figure 4.8 can be divided into two distinct populations: dust-free sources that extend vertically upward in bolometric magnitude and dust-producing sources that have a dust production rate greater than $10^{-11.3} M_\odot yr^{-1}$.

Table 4.6 shows the breakdown of the cumulative DPRs from each class of evolved star. The total DPR from all evolved stars in the central bar of NGC 6822 is 5.6×10^{-7} $M_\odot yr^{-1}$. AGB stars produce 95% of this, with 4% being produced by sources that are below the brightness limit of the TRGB, and finally, 1% is produced by RSG stars. A small number of individual sources produce the vast majority of dust (52% comes from the top 4 sources). The total dust production is weighted 65% oxygen-rich and 35% carbon-rich.

Most CAGB stars in the sample are efficient producers of dust, with 181/192 (94%) producing dust at a rate higher than $10^{-11.3}$ $M_\odot yr^{-1}$. These CAGBs have undergone at least one third dredge-up event, bringing carbon to the stellar surface. The high opacity of the carbonaceous dust that forms in the circumstellar envelope as a result of the shocks following a dredge-up causes efficient transfer of momentum from the stellar radiation to the wind. As such, the presence of carbon in an AGB photosphere causes an increase in DPR (Lattanzio & Wood, 2004; Karakas & Lattanzio, 2014). The total quantity of carbonaceous dust produced by CAGBs in the central bar of NGC 6822 is measured at $\sum \mathrm{DPR_C} = 1.9 \times 10^{-7}$ $M_\odot yr^{-1}$. The majority of this is produced by a single source with a DPR = 6.8×10^{-8} $M_\odot yr^{1}$ and the overall median CAGB DPR = 8.4×10^{-11} $M_\odot yr^{-1}$.

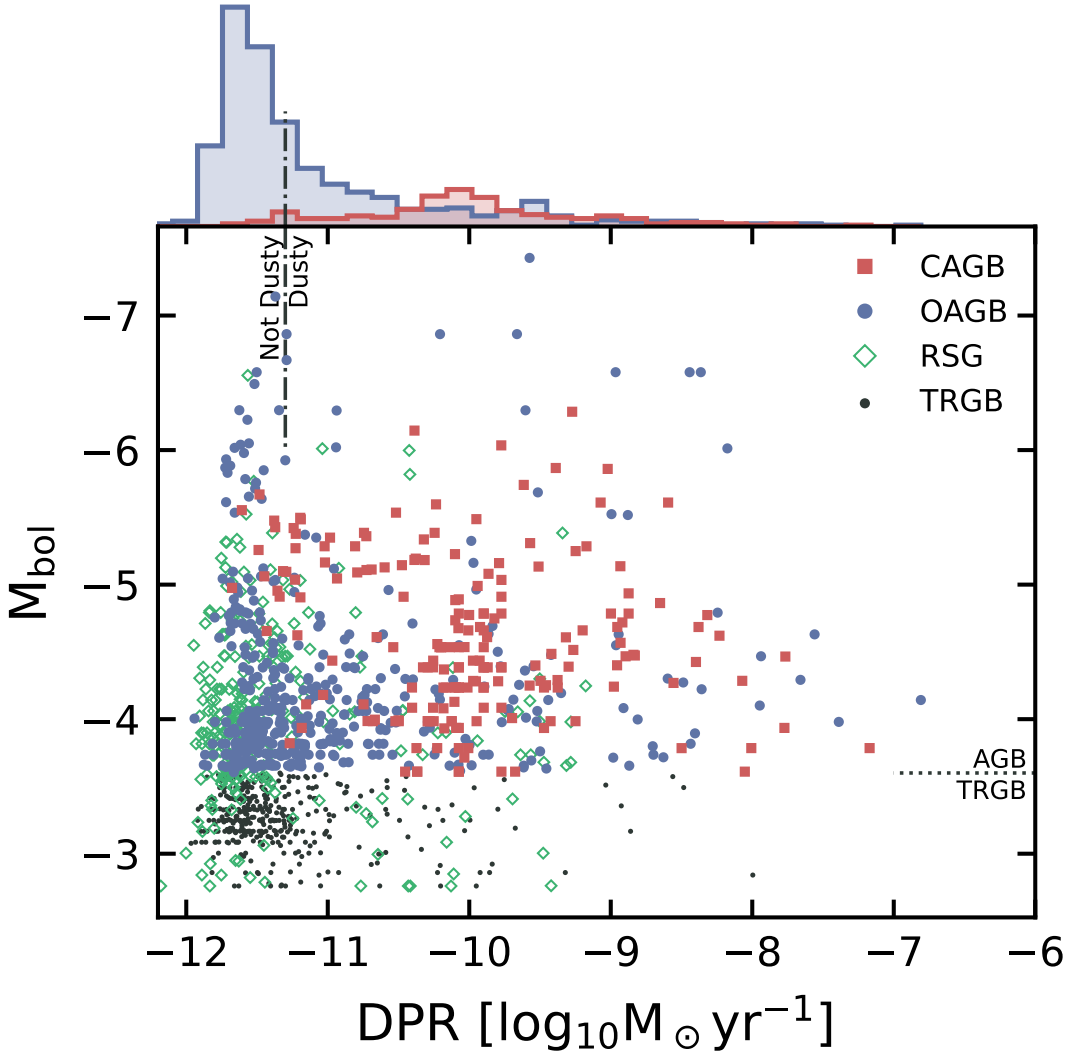

Figure 4.8 Dust production rate (DPR) versus bolometric magnitude (M_{bol}). Oxygen-rich AGB stars are plotted in blue, carbon stars in red, RSG stars in green, and TRGB stars in black. The classical TRGB limit M_{bol}=-3.61 and the boundary between dust-free and dust-producing stars are overlaid. The upper panel shows the distribution of DPR values for the oxygen dust produced by OAGB and RSG stars (blue) and CAGB (red).

OAGBs and RSG stars produce metal oxides and silicate dust. The blue histogram in Figure 4.8 represents the distributions of DPR values across these spectral types. I again split these into two groups: a large, dust-free population centred at -11.5, which drops steeply, giving way to a second dust-producing group that peaks at -9.5. Most OAGBs in the sample have low-to-negligible dust-production rates, with 242/426 stars existing below the boundary of DPR $\leq 10^{-11.3}$. These AGB stars are early in their evolution of the thermally-pulsing stage, and their SEDs are characteristic of dust-free photospheres (Dell'Agli et al., 2016); they may yet evolve into CAGBs after a third dredge-up event (Lattanzio & Wood, 2004).

The total quantity of oxygen dust produced in the sample is $\sum \mathrm{DPR_O} = 3.7 \times 10^{-7}$ $\mathrm{M_\odot yr^{-1}}$, with almost half of this (1.6×10^{-7} $\mathrm{M_\odot yr^{-1}}$) coming from a single source. Of the highest dust-producing (DPR$\geq 10^{-8}$ $\mathrm{M_\odot yr^{-1}}$) stars, 6/9 have an oxygen-rich chemistry. These are likely higher mass (4-8 $\mathrm{M_\odot}$) AGBs undergoing HBB. Depending on the adopted gas-to-dust ratio they may be losing mass at nearly 10^{-5} $\mathrm{M_\odot yr^{-1}}$. Massive OAGBs are proposed to be capable of forming dust in 30 Myr after formation (Boyer et al., 2017) but are observationally rare due to their short lifespan (Justtanont et al., 2013; Whitelock et al., 2018).

RSGs contribute 7.5×10^{-9} $\mathrm{M_\odot yr^{-1}}$ to the dust budget of NGC 6822. This constitutes around 1% of the total DPR, but should be stressed that the sample of RSGs does not include DPR measurements for the brightest stars in the galaxy due to saturation.

Finally, most of the stars below the TRGB are producing very little dust. However, 109/371 are above the DPR threshold and in total contribute $2.4 \times 10^{-8}\mathrm{M_\odot yr^{-1}}$. Modest mass-loss on the RGB typically follows Reimers' law (Reimers, 1975), but this wind is too weak to form these quantities of dust. RGB dust-production has been observed above ~1000$\boldsymbol{L_\odot}$ ($\mathrm{M_{bol}}$=-2.8; McDonald et al., 2011) but this is limited to the very upper tip of the RGB and is small compared to AGB dust-production (Groenewegen, 2014). The highest DPR TRGB source produces $1.0 \times 10^{-8}\mathrm{M_\odot yr^{-1}}$ (42%) and 16 are producing $\geq 10^{-10}$ $\mathrm{M_\odot yr^{-1}}$. The large majority of TRGB sources (98%) exhibit oxygen-rich chemistries. These dust-producing objects may have been misclassified as RGB stars and instead may be early-AGBs or TP-AGBs mid-thermal-pulse. To robustly distinguish these spectral classes, follow-up variability studies or spectroscopy would be required.

The sample of AGB stars in NGC 6822 covers an area of ~29.0 square arcminutes.

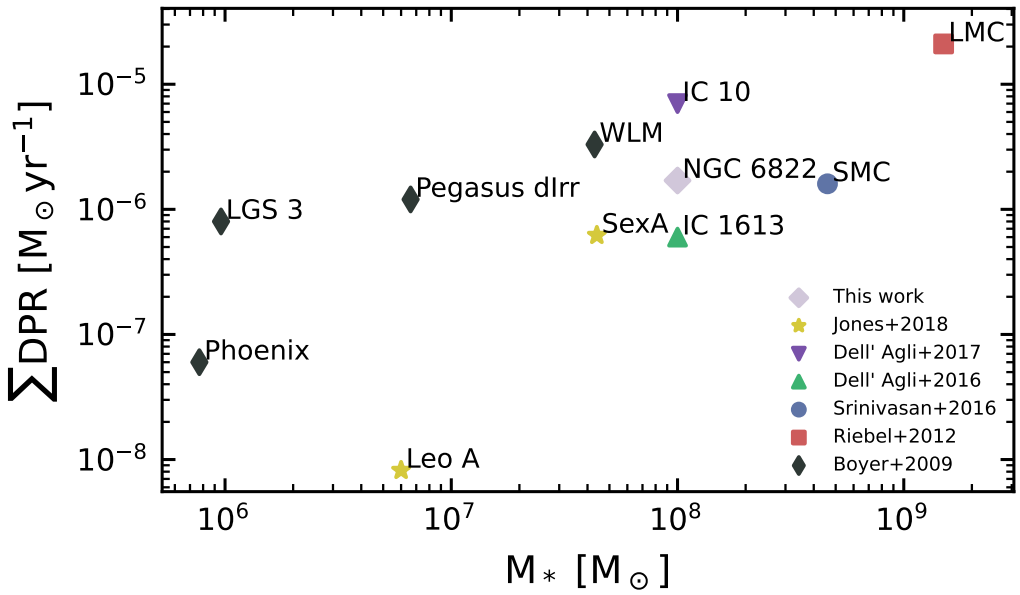

Figure 4.9 The global cumulative DPR for Local Group galaxies versus their stellar mass (M_*). All M_* measurements are taken from McConnachie (2012). The global AGB dust production values are shown for WLM, Pegasus dIrr, LGS 3, Phoenix (Boyer et al., 2009), assuming a gas-to-dust ratio of 200, IC 1613 (Dell'Agli et al., 2016), LMC (Riebel et al., 2012), SMC (Srinivasan et al., 2016), IC 10 (Dell'Agli et al., 2017), Sextans A and Leo A (Jones et al., 2018).

While the stellar component of NGC 6822 extends much further (deprojected radius ~$1-2°$ Battinelli et al., 2006; Zhang et al., 2021), the density of AGB stars drops steeply outside of the central bar (Hirschauer et al., 2020). The catalogue of AGB stars produced by Hirschauer et al. (2020) covers a larger footprint (3 square degrees) than that studied here. Using *UKIRT* and *Spitzer* imaging data, they identified AGB stars with a CMD kernel density technique. They found 1610 AGBs, 1243 of which lie outside the field of view of the NIRCam and MIRI observations. By scaling the total DPR to account for these missing stars in the outskirts of NGC 6822, the lower limit for global dust production by AGB stars can be estimated as 1.69×10^{-6} $M_\odot yr^{-1}$. It should be noted that this conservative estimate does not account for differences in population ages or completeness and blending in the Hirschauer et al. (2020) sample, which also does not cover the full extent of the galaxy.

Figure 4.9 shows the total DPR estimated for Local Group dwarf galaxies, versus their estimated stellar mass (M_*). All M_* values are taken from McConnachie

(2012). It can be seen that the total DPR for NGC 6822 measured in this work is in good agreement with galaxies of similar stellar masses. The three most comparable galaxies in terms of stellar mass and total dust production: SMC (1.6×10^{-6} $M_{\odot}yr^{-1}$ Srinivasan et al., 2016), IC 1613 (6×10^{-7} $M_{\odot}yr^{-1}$ Dell'Agli et al., 2016) and IC 10 (7×10^{-6} $M_{\odot}yr^{-1}$ Dell'Agli et al., 2017). The higher metallicity galaxy ($\sim0.4Z_{\odot}$; Garnett, 1990; Magrini & Gonçalves, 2009) IC 10, is expected to have a higher total DPR despite its comparable stellar mass to NGC 6822, due to the increased efficiency of dust formation at higher Z (Höfner & Olofsson, 2018). Conversely, the lower metallicity ($\sim0.15 - 0.2Z_{\odot}$; Lee et al., 2003; Bresolin et al., 2007) IC 1613, is therefore expected to have a lower total DPR. Finally, the SMC, with a metallicity comparable to NGC 6822 ($\sim0.2Z_{\odot}$; Garnett et al., 1995; Peimbert et al., 2000) exhibits a very similar dust production rate. These predictions are all in agreement with the observed rates.

AGB dust production in metal-poor galaxies, for example, IC 10, IC 1613, SMC, and the slightly more metal-rich LMC (Riebel et al., 2012), has previously been found to be dominated by CAGB stars. Here, however, the results suggest that two-thirds of the dust produced in NGC 6822 originates from OAGBs. The star formation history of NGC 6822 may be the cause of this disparity. It is known that there has been enhanced star formation in the past 100-200 Myr (Gallart et al., 1996b), which at the metallicity of NGC 6822 would produce ~4 $M_{\odot}$ oxygen-rich stars that undergo HBB (Marigo et al., 2008). This could result in the enhanced oxygen-rich DPR that is measured here.

Misclassification of some of the most extreme sources is another potential avenue for increased oxygen-rich dust. The most extreme dust-producing object in the sample, CN123349, seen in the lower right panel of Figure 4.4 has equally good fits to both AGB and YSO SED models (it is just below the boundary in Figure 4.5). With the uncertainties associated with SED fitting, it is not possible to say whether this particular source is producing 1.6×10^{-7} $M_{\odot}yr^{-1}$ of oxygen-rich dust, or instead is a deeply embedded YSO, ultimately removing dust from the system. By excluding this source from the sample, the relative contribution of carbon to oxygen dust is approximately equal. However, the oxygen-rich contribution is still substantially higher than estimates from other metal-poor galaxies. Only follow-up spectroscopy or narrow-band photometry of these sources would give a conclusive answer. The contribution to the total dust production by the other 13 "*ambiguous objects*" is modest in comparison.

Table 4.7 Parametrised hyperbolic functions to estimate dust-production rate of CAGBs, using observable *JWST* NIRCam and MIRI colour combinations x. Listed are the parameters DPR = $p_0/(x + p_1) + p_2$ and residual median absolute deviation (MAD) of each measured combination.

JWST Colour	p_0	p_1	p_2	MAD
F115W–F1500W	-28.20	4.21	-6.21	0.28
F115W–F2100W	-37.84	5.72	-5.81	0.19
F200W–F770W	-12.62	2.46	-6.68	0.23
F200W–F1000W	-5.91	1.26	-7.68	0.09
F200W–F1500W	-15.82	2.89	-6.45	0.19
F200W–F2100W	-16.52	2.98	-6.45	0.13
F356W–F770W	-0.65	0.04	-9.23	0.27

4.4.3 Observable Proxies for Dust Production

Empirical hyperbolic relations between AGB dust production rate and photometric colour have been long established with *IRAS* (Whitelock et al., 1994; Le Bertre, 1997). Particularly, the K – [12μm] vs. DPR is tight as the filters trace the photosphere and the circumstellar envelope, respectively. As such, this combination provides a simple observable proxy to dust production rates. Similarly incorporating *Spitzer* colour combinations, (Matsuura et al., 2009; Gullieuszik et al., 2012; Riebel et al., 2012), DPRs show clear relations with K – [8.0μm] and [3.6μm] – [8.0μm]. It is interesting to explore if such empirical relations hold also for *JWST* filters.

Figure 4.10 shows F200W–F1000W vs. DPR for CAGBs (red) and OAGBs (blue). I fit a hyperbola to the dust production from CAGBs, taking the form DPR = $p_0/(x+p_1)+p_2$, where x is the colour combination and $p_{1,2,3}$ are fitting parameters. I find that this description works well for CAGBs as their distribution of infrared colours is much broader than the comparatively tightly spaced colours of OAGBs. I measure the median absolute deviation of data points from the fit model (MAD) and present colour combinations with MAD $\leq$ 0.3 in Table 4.7. I find that to obtain reasonable relations with MAD $<$ 0.3, wide baseline colour combinations are required, and as such, utilising one NIRCam and one MIRI filter is necessary. This is due to the amplification of the effects of dust on the SED as wavelength increases. By sampling flux in a shorter NIRCam filter, where the predominant flux contribution comes from the photosphere of the star and a dust-tracing MIRI filter, the comparative strength of each component is effectively measured.

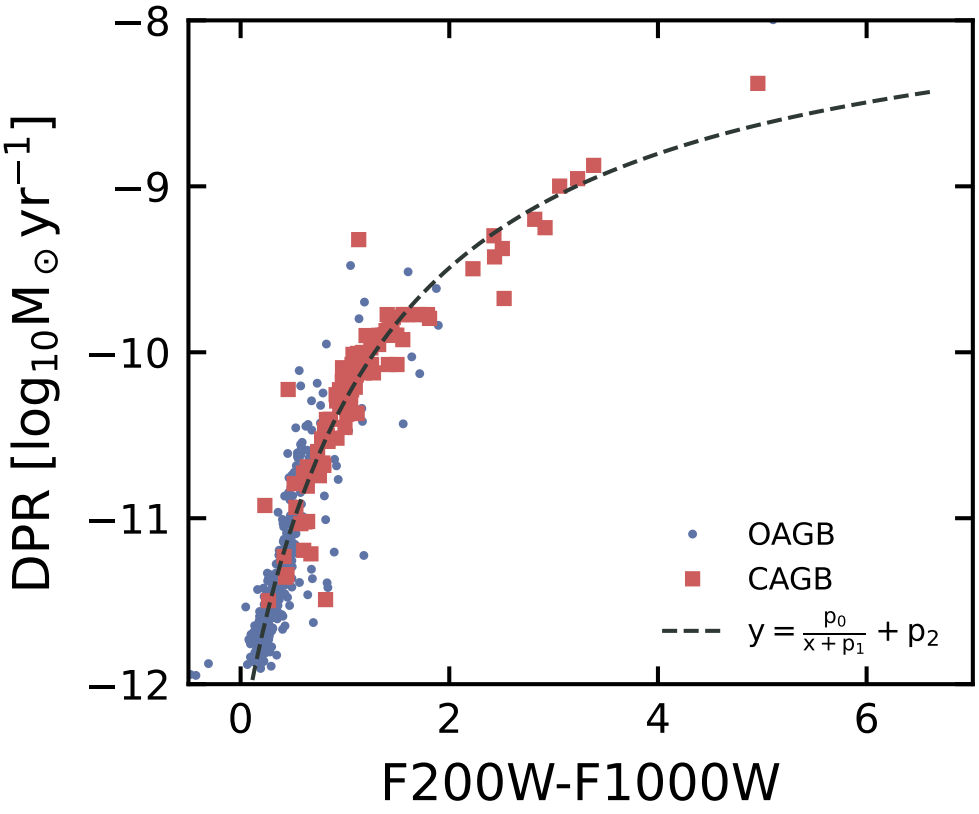

Figure 4.10 DPR vs F200W–F1000W of CAGB (red) and OAGBs (blue). The best-fitting parametrised hyperbolic function DPR = $p_0/(x+p_1)+p_2$ is overlaid as a dashed line.

I find that the F200W NIRCam filter, in combination with any of our MIRI filters, yields the lowest MAD residuals and therefore the tightest relations. This filter, although slightly bluer, is comparable to the K band. In combination with F1000W, which will catch the rising edge of the 11.3 μm SiC feature in the circumstellar shell of carbon stars, can act as a proxy to the previously used K-[12] combination. The strength of the dust emission will increase at longer MIRI wavelengths, with both F200W–F1500W and F200W–F2100W resulting in well-constrained fits. However, the source density drops off rapidly in the F2100W filter, and only 135 AGBs are observed in both of these filters, making the precise form of these relationships more uncertain.

4.4.4 Spatial Distribution of Dust Production

Figure 4.11 shows the spatial distribution of dusty AGB stars. For illustrative purposes, the size of each point scales with the DPR. The underlying contour map shows the distribution of all AGB stars detected by Hirschauer et al. (2020). The 14.5 square arcminute field-of-view of MIRI and the overlapping 29.0 square arcminute field-of-view of NIRCam are shown as dashed bounding boxes.

By eye, the density of dust-producing AGB stars broadly follows the underlying distribution of all AGB stars, with no apparent deviations from this. However, there is a clear distinction in chemical classification across the fields, with the central stellar bar being populated by a much higher proportion of carbon-rich stars and oxygen-rich stars appearing more diffuse. The proportion of OAGBs to CAGBs has been seen to increase as a function of distance from the centre of NGC 6822 by Sibbons et al. (2012) and Hirschauer et al. (2020), but in both cases, the small number of stars limits the accuracy of the results.

Mapping a ratio of CAGBs to OAGBs spatially (known as the C/M ratio) is a long-standing method of describing metallicity trends across a galaxy (Cioni & Habing, 2003). OAGBs are unable to synthesise their own oxygen during nuclear burning; as such, they are harder to form in low metallicity environments, while carbon can be produced in core fusion. This results in CAGBs forming more readily in these galaxies, and OAGBs converting to CAGBs during their evolution (Iben & Renzini, 1983; Battinelli & Demers, 2005), leading to the ratio of the number of CAGBs to OAGBs being a proxy for metallicity.

I create density maps by counting OAGB and CAGB sources in 0.6′ bins of right

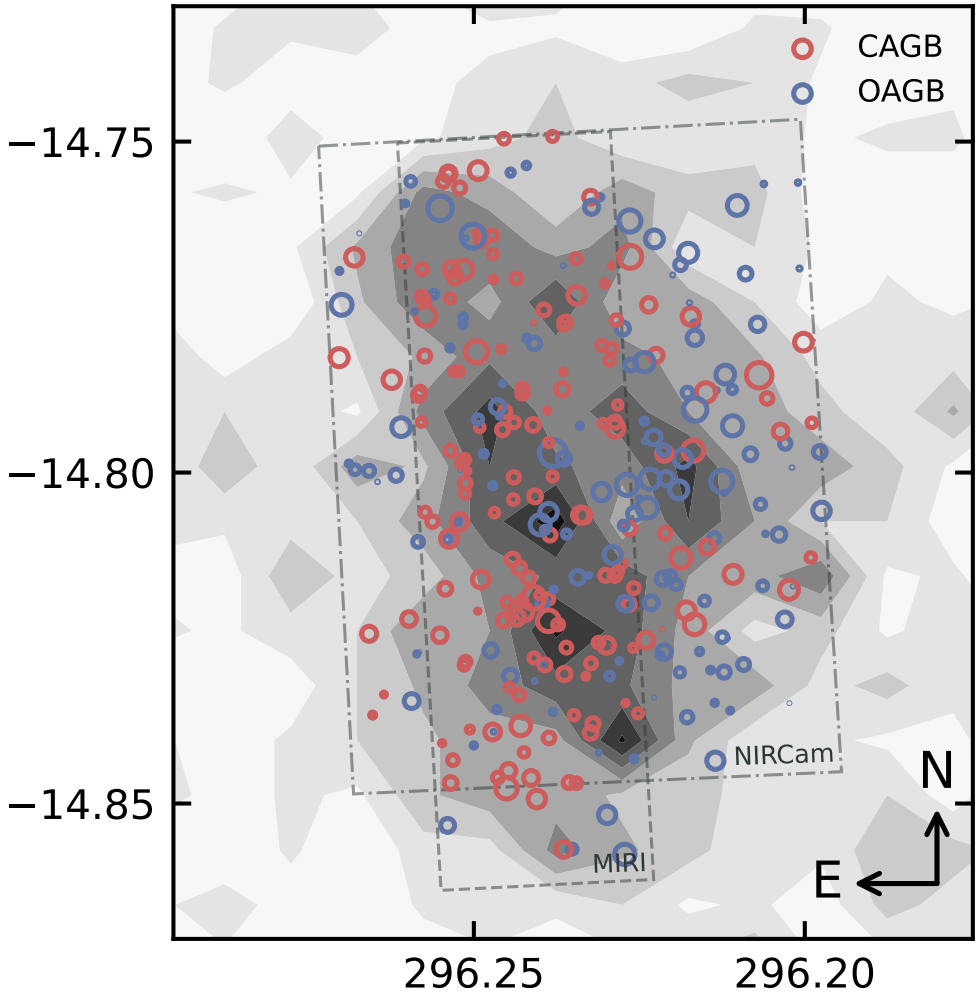

Figure 4.11 Spatial distribution of dusty (DPR≥ $10^{-11.3}$) AGB stars, coloured by chemical subtype (OAGB blue, CAGB red) and point size scaled by individual DPR. The underlying contour plot shows AGB stars detected by Hirschauer et al. (2020), with the NIRCam and MIRI fields of view shown in dashed bounding boxes.

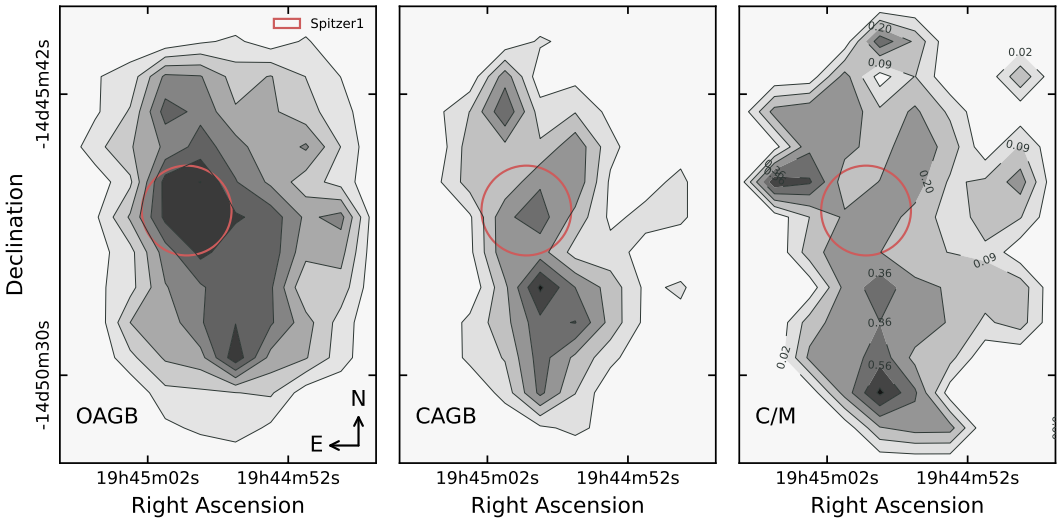

Figure 4.12 Source density contour maps for OAGB (left), CAGB (middle) and C/M ratio (right). Sources are binned in 0.6′ bins and smoothed with a 0.24′ Gaussian kernel. The location of Spitzer I, the forming region, is indicated in red.

ascension and declination. These count maps are smoothed with a Gaussian kernel of width 0.24′ plotted in contour maps in Figure 4.12. The leftmost panel shows the distribution of OAGBs, and the middle panel shows CAGBs. The rightmost panel shows the ratio of the density maps CAGB/OAGB, which is smoothed in the same manner and displayed as a contour plot. The location of Spitzer I (Jones et al., 2019; Lenkić et al., 2024), a massive star-forming region, is shown in red.

The density of both OAGBs is high in the area overlapping with Spitzer I, which may be indicative of remaining YSO contamination. However, the AGB stars in this area are almost entirely dust-free; these have SED shapes closely resembling blackbodies, which is unlikely in YSOs (Jones et al., 2017b). As such, the method outlined in Section 4.3.5 is effective in identifying these dust-free AGBs. The portion of dusty OAGBs (which may be more easily mistaken for YSOs) within this region is not uncharacteristically high compared to other areas of the field. Tight peaks in the C/M ratio map are likely due to small-sample statistics. The small footprint of this sample of AGB stars limits the accuracy of the C/M ratio map as a diagnostic for metallicity for NGC 6822 as a whole. In the future, *Euclid* observations of this galaxy (Hunt et al., 2025) could be combined with these *JWST* results to build an accurate picture of the C/M ratio of the whole galaxy.

4.5 Summary

In this Chapter, I improve upon the MIRI photometry presented in Chapter 3. Using this more accurate catalogue, I produce an H-R diagram of the central stellar bar of NGC 6822 to a photometric depth that encompasses the Red Clump. I identify the evolved stars using colour cuts, and measure their dust production rates by fitting the GRAMS model SEDs. I find the total dust production rate to be 5.6×10^{-7} $M_{\odot}yr^{-1}$ with 60% of this contributed by OAGB stars. I determine observable near-mid-IR colour proxies for dust production rate and map the spatial distribution of dust-producing AGB stars.

5 Conclusions

The majority of this thesis was written in vim :wqa

— Anonymous

This thesis has used state-of-the-art data from *JWST* to conduct an in-depth exploration of the evolved stellar populations in the Local Group dwarf galaxy, NGC 6822. To facilitate this analysis, I have conceived and developed a photometric pipeline that takes a novel approach to deal with sources that lie on top of complex backgrounds. I have conducted multi-band photometry for ~1 million stars in the central bar and studied how different stellar populations appear on a variety of CMDs, reaching into the rarely studied mid-IR regime, Finally I have measured the contribution of evolved stars to the dust budget of the galaxy, and interpreted my results within the broader context of understanding the dust life cycle on galactic scales.

5.1 Summary

In Chapter 2, I introduce the need for dedicated photometry software to analyse *JWST* imaging data, leading to the development of StarBUGII. This suite of photometric routines is designed to produce deep PSF photometry in crowded fields with complex dusty backgrounds. In this Chapter, I discuss the underlying methods for all required routines for producing a complete band-matched catalogue from raw exposures and mosaics. I outline the "three-fold" ensemble of source detection subroutines, which target bright, faint, and embedded sources, respectively. The complete source detection routine in StarBUGII outperforms

the *JWST* photometric pipelines' source detection rate by an order of magnitude. I provide a routine for estimating the flux contribution from the underlying dusty diffuse emission, a step that is vital in obtaining accurate photometry from the point source. Both aperture and PSF photometry are available in the program. While it is possible to empirically define one's own PSF models, in this thesis, I use the WEBBPSF models for all photometry. Several catalogue matching routines were developed, particularly to account for the diversity of *JWST* programs and use cases required. Finally, a method for rapid artificial star testing was developed, allowing the user to quantify both catalogue completeness and the effect of parameter changes at every stage of photometric processing. STARBUGII has been adopted for the photometric processing for several *JWST* GTO programs, of which I am a member, and enabled us to release some of the first stellar population analysis of extra-galactic star-forming regions from the observatory. It is also now being used more widely by other researchers in the stellar populations community.

In Chapter 3, I outline the *JWST* GTO imaging program targeting NGC 6822. Using STARBUGII, I produced a combined near- and mid-IR stellar populations catalogue of the central stellar bar of the metal-poor dwarf galaxy. I present an array of CMDs and demonstrate the complexity of the stellar populations within. I identify the young UMS and YSOs, the old RGB, RC, and associated structures, as well as the evolved AGB and RSG stars. As a testament to the precision of the data, I also reveal the elusive AGB bump embedded within the RGB. Using luminosity functions, I estimate the position of the tip of the RGB in the near- and mid-IR, up to and including the 10 μm filter F1000W. Finally, by comparing the main field with parallel imaging data, I demonstrate that young populations are absent or reduced in number outside the central stellar bar of the galaxy.

In Chapter 4, I revisit the mid-IR photometry with improved calibration files, incorporating MIRI PSF photometry into the band-matched catalogue. I produce an H-R diagram of all the NGC 6822 catalogue stars to a photometric depth ~0.5 magnitudes below the RC. Evolved star candidates are identified through a series of colour cuts, and this selection is refined by removing resolved background objects and YSOs using YSO model SED fitting. The remaining 1250 are classified into four categories: CAGB, OAGB, RSG, and sub-TRGB stars. I fit model SEDs from the GRAMS model grid to determine stellar properties, including effective temperature, bolometric luminosity and dust production rate for the evolved stars. I analyse the carbon-star luminosity function, showing

consistency with expectations and show the potential detection of two OAGB stars brighter than the theoretical limit $M_{bol} = -7.1$. I measure the total dust production rate of the evolved stars to be DPR = 5.6×10^{-7} $M_{\odot}yr^{-1}$. Of this, 60% is contributed by OAGB stars, 35% from CAGBs and 1% from RSGs. The remaining 4% come from objects that are fainter than the TRGB; some of these may be dust-enshrouded AGB stars whose photospheric light has been absorbed by their circumstellar shells. Extrapolating the observed dust production rate to a broader galactic scale, I estimate the lower limit of evolved star dust production in NGC 6822 to be DPR = 1.7×10^{-6} $M_{\odot}yr^{-1}$, consistent with expectations from comparable galaxies in the Local Group. I develop parameterised photometric colour relations as observable proxies for dust production rates, showing that this is most effective when combining one NIRCam and one MIRI filter. Finally, I map the spatial distribution of dust-producing AGB stars and show the spatial C/M ratio for the observed region.

5.2 Future Work

HST Follow-Up

The largest area of uncertainty in the results presented is the classification of the most extreme sources in the evolved star catalogue. Though SED model fitting has proven an effective method of classifying AGB stars with *Spitzer* data in the Magellanic Clouds and beyond (Riebel et al., 2012; Srinivasan et al., 2016; Jones et al., 2018), the underlying broad-band photometry traces only broad features, and finer details of specific dust spectral features may be blended. This problem also exists with the *JWST* analysis presented in this thesis. With this in mind, I successfully proposed an *HST* Cycle-32 Bridge Program (PID:17910) to gain medium-band photometry with WFC3-IR of my *JWST* field.

WFC3-IR medium bands F127M, F139M, and F153M uniquely trace H_2O absorption in OAGBs and CN+C_2 features in CAGBs. Therefore, *HST* medium-band photometry has become the gold standard for segregating TP-AGB subtypes (Boyer et al., 2013, 2017, 2019; Goldman et al., 2019; Jones et al., 2023c). The F139M filter sits entirely within a water absorption band that increases in strength in OAGBs as the effective temperature decreases. In CAGBs, the F127M, F139M , and F153M filters sample around a CN+C_2 feature at > 1.4μm. Models from Aringer et al. (2009, 2016) and *HST* observations mentioned above

definitively show that these molecular features cause a clean separation of C- and OAGBs in a combined colour-colour diagram.

This six-orbit program will observe the full *JWST* coverage (see Figure 3.1), thus providing a perfect overlapping data set. The photometric depth achieved will extend below the TRGB, allowing all 1250 evolved stars to gain data in these filters. By acquiring these data, I will test the performance of the methods outlined in Chapter 4, verifying that the technique is applicable with *JWST* photometry, as it was with *Spitzer*, and refine the chemical separation of dust return in NGC 6822.

A Broader View with Euclid

The results presented in this thesis are limited to a ~29 square arcminute region in the centre of the NGC 6822 (and smaller still if only MIRI is considered). While the stellar density of AGB stars drops significantly outwith this area (Hirschauer et al., 2020), the galaxy extends far further ($\sim 1-2°$; Battinelli et al., 2006; Zhang et al., 2021). This small footprint of these *JWST* observations recovered a large number of AGB stars, more than double the number known to exist outside this region (Sibbons et al., 2012; Hirschauer et al., 2020). Fortunately, NGC 6822 was a target of the *Euclid* Early Release Observations (Hunt et al., 2025). The large FoV ($41' \times 41'$) encompasses the entire central stellar component of the galaxy. The instruments onboard *Euclid* (VIS and NISP) cover a photometric baseline 550-900nm and 940-2000nm, respectively. The VIS instrument operates with a single wide-band filter roughly equivalent to R+I+Z, and NISP uses three equivalent to Y, J and H in Figure 1.12. Notably, the VIS instrument has a pixel scale of 0.1″ per pixel and NISP 0.3″per pixel; therefore, *Euclid* is capable of providing high-resolution images across an enormous FoV.

The uniform coverage, high resolution and wide photometric baseline of *Euclid* will provide accurate identification of AGB stars across the entirety of NGC 6822. This will open avenues of research into mapping the spatial distributions of these stars, shedding light on radial gradients in the SFH and metallicity. Cross-matching between *JWST* and the forthcoming *HST* data will enable validation of *Euclid* stellar classification mechanisms and the extrapolation of physical properties on a galaxy-wide scale. This will provide a unique and comprehensive view of the structure, evolution and dust contribution of the AGB population in NGC 6822.

Mining the *JWST* Catalogue

The point source catalogue produced in this thesis represents the deepest photometric catalogue of NGC 6822 to date. While AGB stars are present, they occupy only the brightest third of the total magnitude range of detected sources, underscoring the catalogue's sensitivity to significantly fainter and lower-mass stellar populations. The depth and quality of the photometry open new avenues for reconstructing the SFH of the galaxy and for testing and validating the predictions of stellar models in this low metallicity regime. With precise measurements across a broad range of evolutionary phases, age dating can be performed through CMDs and isochrone fitting of individual populations (Bortolini et al., 2024). The inclusion of young populations, such as RSGs, UMS and older post-MS populations, such as the RC, VRC, and RGB, ensures sensitivity to recent and intermediate-age stellar populations. Additionally, metallicity effects can be constrained through the observed colour spread and comparison with theoretical stellar evolution models.

Spatially resolved SFHs can be derived across the observed field and compared to known sites of active star formation. One of the two NIRCam parallel imaging fields obtained and reduced in Chapter 3 encompasses the Hubble IV star-forming region and, like the main field, is rich in young stars. In contrast, the second parallel field is centred on a region with no known active star formation, providing a valuable control for comparison. Examining the stellar populations across these contrasting environments may offer insight into how star formation has proceeded over time and how it may vary within different regions of a dwarf irregular galaxy. It is for this reason that we successfully proposed additional *JWST* observations (PID:8525) targeting three further star-forming regions, Hubble I/III, V, and X. With full near- and mid-infrared coverage of these regions, alongside the existing data for Spitzer I and Hubble IV, a detailed, multi-epoch analysis of different stages of star formation and HII region evolution within a single galaxy will be possible, to a level only previously achieved by the SAGE survey in the Magellanic Clouds (Meixner et al., 2006; Gordon et al., 2011).

Starbugii

starbugii has been proven to be an effective tool for measuring photometry in some of the most challenging fields. Future work on this program will include increased generalisation and applicability to other telescopes, improved performance efficiency and continued development on the underlying routines.

5.3 Closing Remarks

This exploration of the infrared populations and focus on dust returned to the ISM from evolved stars is limited to a single galaxy, NGC 6822. The long-anticipated power of *JWST* has opened the door to similar research across and beyond the Local Group. As further datasets begin to accumulate for other galaxies, so too will fresh insights into the lifecycle of baryons in galaxies and the universal processes that govern star formation and feedback across the Universe. NGC 6822 stands here not as an endpoint, but as a stepping stone.

Bibliography

Ahmad A., Freytag B., Höfner S., 2023, A&A, 669, A49

Algera H. S. B., et al., 2023, MNRAS, 518, 6142

Alves D. R., 2000, ApJ, 539, 732

Antoniadis K., et al., 2025, arXiv e-prints, p. arXiv:2503.05876

Aringer B., Girardi L., Nowotny W., Marigo P., Lederer M. T., 2009, A&A, 503, 913

Aringer B., Girardi L., Nowotny W., Marigo P., Bressan A., 2016, MNRAS, 457, 3611

Baldacci L., Clementini G., Held E. V., Rizzi L., 2003, Mem. Soc. Astron. Italiana, 74, 860

Barnard E. E., 1884, Astronomische Nachrichten, 110, 125

Battinelli P., Demers S., 2005, A&A, 434, 657

Battinelli P., Demers S., Kunkel W. E., 2006, A&A, 451, 99

Benjamin R. A., et al., 2003, PASP, 115, 953

Bennet P., et al., 2024, ApJ, 971, 98

Bernard J.-P., et al., 2008, AJ, 136, 919

Bildsten L., Paxton B., Moore K., Macias P. J., 2012, ApJ, 744, L6

Bladh S., Höfner S., 2012, A&A, 546, A76

Bloecker T., 1995, A&A, 297, 727

Blum R. D., et al., 2006, AJ, 132, 2034

Boothroyd A. I., Sackmann I. J., 1992, ApJ, 393, L21

Boothroyd A. I., Sackmann I. J., Ahern S. C., 1993, ApJ, 416, 762

Boothroyd A. I., Sackmann I. J., Wasserburg G. J., 1995, ApJ, 442, L21

Bortolini G., et al., 2024, A&A, 689, A146

Bovy J., et al., 2014, ApJ, 790, 127

Bowen G. H., 1988, ApJ, 329, 299

Bowen G. H., Willson L. A., 1991, ApJ, 375, L53

Boyer M. L., Skillman E. D., van Loon J. T., Gehrz R. D., Woodward C. E., 2009, ApJ, 697, 1993

Boyer M. L., et al., 2011, AJ, 142, 103

Boyer M. L., et al., 2012, ApJ, 748, 40

Boyer M. L., et al., 2013, ApJ, 774, 83

Boyer M. L., et al., 2015a, ApJS, 216, 10

Boyer M. L., et al., 2015b, ApJ, 800, 51

Boyer M. L., et al., 2017, ApJ, 851, 152

Boyer M. L., et al., 2019, ApJ, 879, 109

Bradley L., et al., 2022, astropy/photutils: 1.5.0, doi:10.5281/zenodo.6825092, https://doi.org/10.5281/zenodo.6825092

Bresolin F., Urbaneja M. A., Gieren W., Pietrzyński G., Kudritzki R.-P., 2007, ApJ, 671, 2028

Bressan A., Marigo P., Girardi L., Salasnich B., Dal Cero C., Rubele S., Nanni A., 2012, MNRAS, 427, 127

Bushouse H., et al., 2022, JWST Calibration Pipeline, doi:10.5281/zenodo.7229890, https://doi.org/10.5281/zenodo.7229890

Cannon J. M., et al., 2006, ApJ, 652, 1170

Caputo F., Castellani V., Wood P. R., 1978, MNRAS, 184, 377

Cardelli J. A., Clayton G. C., Mathis J. S., 1989, ApJ, 345, 245

Carrera R., Gallart C., Hardy E., Aparicio A., Zinn R., 2008, AJ, 135, 836

Cerny W., Freedman W. L., Madore B. F., Ashmead F., Hoyt T., Oakes E., Quang Hoang Tran N., Moss B., 2020, arXiv e-prints, p. arXiv:2012.09701

Cherchneff I., Le Teuff Y. H., Williams P. M., Tielens A. G. G. M., 2000, A&A, 357, 572

Chiosi C., Bertelli G., Bressan A., 1992, ARA&A, 30, 235

Cioni M. R. L., 2009, A&A, 506, 1137

Cioni M. R. L., Habing H. J., 2003, A&A, 402, 133

Cioni M. R. L., Habing H. J., 2005, A&A, 429, 837

Cioni M. R. L., van der Marel R. P., Loup C., Habing H. J., 2000, A&A, 359, 601

Cioni M. R. L., Girardi L., Marigo P., Habing H. J., 2006a, A&A, 448, 77

Cioni M. R. L., Girardi L., Marigo P., Habing H. J., 2006b, A&A, 452, 195

Clementini G., Held E. V., Baldacci L., Rizzi L., 2003, ApJ, 588, L85

Dalcanton J. J., et al., 2012, ApJS, 200, 18

Davies B., Beasor E. R., 2018, MNRAS, 474, 2116

De Marchi G., et al., 2024, ApJ, 977, 214

Delgado Mena E., Israelian G., González Hernández J. I., Bond J. C., Santos N. C., Udry S., Mayor M., 2010, ApJ, 725, 2349

Dell'Agli F., Di Criscienzo M., Boyer M. L., García-Hernández D. A., 2016, MNRAS, 460, 4230

Dell'Agli F., Di Criscienzo M., García-Hernández D. A., Ventura P., Limongi M., Marini E., Jones O. C., 2019, MNRAS, 482, 4733

Dell'Agli F., García-Hernández D. A., Schneider R., Ventura P., La Franca F., Valiante R., Marini E., Di Criscienzo M., 2017, Monthly Notices of the Royal Astronomical Society, 467, 4431–4440

Dicken D., et al., 2024, A&A, 689, A5

Dimitrova T., Neugent K., Levesque E., Massey P., 2021, in American Astronomical Society Meeting Abstracts. p. 548.08

Diolaiti E., Bendinelli O., Bonaccini D., Close L., Currie D., Parmeggiani G., 2000, A&AS, 147, 335

Dolphin A. E., 2000, PASP, 112, 1383

Draine B. T., 2011, Physics of the Interstellar and Intergalactic Medium

Dréau G., Lebreton Y., Mosser B., Bossini D., Yu J., 2022, A&A, 668, A115

Dunne L., Eales S., Ivison R., Morgan H., Edmunds M., 2003, Nature, 424, 285

Durbin M. J., Beaton R. L., Dalcanton J. J., Williams B. F., Boyer M. L., 2020, ApJ, 898, 57

Fabricius C., et al., 2021, A&A, 649, A5

Feast M. W., Glass I. S., Whitelock P. A., Catchpole R. M., 1989, MNRAS, 241, 375

Ferraro F. R., 1992, Mem. Soc. Astron. Italiana, 63, 491

Ferraro F. R., Messineo M., Fusi Pecci F., de Palo M. A., Straniero O., Chieffi A., Limongi M., 1999, AJ, 118, 1738

Ferrarotti A. S., Gail H. P., 2006, A&A, 447, 553

Freedman W. L., et al., 2020, ApJ, 891, 57

Fusco F., Buonanno R., Hidalgo S. L., Aparicio A., Pietrinferni A., Bono G., Monelli M., Cassisi S., 2014, A&A, 572, A26

Gaia Collaboration et al., 2021, A&A, 649, A1

Gall C., Hjorth J., Andersen A. C., 2011, A&ARv, 19, 43

Gallart C., Aparicio A., Vilchez J. M., 1996a, AJ, 112, 1928

Gallart C., Aparicio A., Bertelli G., Chiosi C., 1996b, AJ, 112, 1950

Gallart C., Aparicio A., Bertelli G., Chiosi C., 1996c, AJ, 112, 2596

García-Hernández D. A., Zamora O., Yagüe A., Uttenthaler S., Karakas A. I., Lugaro M., Ventura P., Lambert D. L., 2013, A&A, 555, L3

Garnett D. R., 1990, ApJ, 363, 142

Garnett D. R., Skillman E. D., Dufour R. J., Peimbert M., Torres-Peimbert S., Terlevich R., Terlevich E., Shields G. A., 1995, ApJ, 443, 64

Gáspár A., et al., 2021, PASP, 133, 014504

Gehrz R., 1989, in Allamandola L. J., Tielens A. G. G. M., eds, IAU Symposium Vol. 135, Interstellar Dust. p. 445

Girardi L., 1999, MNRAS, 308, 818

Girardi L., 2016, ARA&A, 54, 95

Girardi L., Marigo P., 2007, A&A, 462, 237

Girardi L., Groenewegen M. A. T., Weiss A., Salaris M., 1998, MNRAS, 301, 149

Goldman S. R., et al., 2019, ApJ, 877, 49

Gordon K. D., 2024, Journal of Open Source Software, 9, 7023

Gordon K. D., et al., 2011, AJ, 142, 102

Groenewegen M. A. T., 2006, A&A, 448, 181

Groenewegen M. A. T., 2014, A&A, 561, L11

Gullieuszik M., et al., 2012, A&A, 537, A105

Habel N., et al., 2024, ApJ, 971, 108

Habing H. J., 1996, A&ARv, 7, 97

Habing H. J., Olofsson H., eds, 2003, Asymptotic giant branch stars

Habing H. J., Olofsson H., 2004, in Habing H. J., Olofsson H., eds, , Asymptotic Giant Branch Stars. pp 1–21, doi:10.1007/978-1-4757-3876-6_1

Härm R., Schwarzschild M., 1961, AJ, 66, 45

Harris J., Zaritsky D., 2004, AJ, 127, 1531

Hawkins K., Ting Y.-S., Walter-Rix H., 2018, ApJ, 853, 20

Herwig F., 2005, ARA&A, 43, 435

Hirschauer A. S., Gray L., Meixner M., Jones O. C., Srinivasan S., Boyer M. L., Sargent B. A., 2020, ApJ, 892, 91

Hirschauer A. S., et al., 2024, AJ, 168, 23

Hodge P. W., 1977, ApJS, 33, 69

Hodge P., Lee M. G., Kennicutt Robert C. J., 1989, PASP, 101, 32

Höfner S., Dorfi E. A., 1997, A&A, 319, 648

Höfner S., Olofsson H., 2018, A&ARv, 26, 1

Hopkins P. F., Quataert E., Murray N., 2012, MNRAS, 421, 3522

Hoppe P., Leitner J., Kodolányi J., Borrmann S., Jones A. P., 2022, Nature Astronomy, 6, 1027

Hubble E. P., 1925, ApJ, 62, 409

Humphreys R. M., Davidson K., 1979, ApJ, 232, 409

Hunt L. K., et al., 2025, A&A, 697, A9

Iben Jr. I., 1967, ApJ, 147, 624

Iben Jr. I., 1975, ApJ, 196, 549

Iben Jr. I., Renzini A., 1983, ARA&A, 21, 271

Inami H., et al., 2022, MNRAS, 515, 3126

Javadi A., van Loon J. T., Khosroshahi H., Mirtorabi M. T., 2013, MNRAS, 432, 2824

Jones A. P., Tielens A. G. G. M., Hollenbach D. J., 1996, ApJ, 469, 740

Jones O. C., Kemper F., Srinivasan S., McDonald I., Sloan G. C., Zijlstra A. A., 2014, MNRAS, 440, 631

Jones O. C., McDonald I., Rich R. M., Kemper F., Boyer M. L., Zijlstra A. A., Bendo G. J., 2015a, MNRAS, 446, 1584

Jones O. C., Meixner M., Sargent B. A., Boyer M. L., Sewiło M., Hony S., Roman-Duval J., 2015b, ApJ, 811, 145

Jones O. C., et al., 2017a, MNRAS, 470, 3250

Jones O. C., Meixner M., Justtanont K., Glasse A., 2017b, ApJ, 841, 15

Jones O. C., Maclay M. T., Boyer M. L., Meixner M., McDonald I., Meskhidze H., 2018, ApJ, 854, 117

Jones O. C., Sharp M. J., Reiter M., Hirschauer A. S., Meixner M., Srinivasan S., 2019, MNRAS, 490, 832

Jones O. C., et al., 2023a, Nature Astronomy, 7, 694

Jones O. C., Boyer M. L., McDonald I., Meixner M., van Loon J. T., 2023b, MNRAS, 525, 3693

Jones O. C., Boyer M. L., McDonald I., Meixner M., van Loon J. T., 2023c, MNRAS, 525, 3693

Justtanont K., Teyssier D., Barlow M. J., Matsuura M., Swinyard B., Waters L. B. F. M., Yates J., 2013, A&A, 556, A101

Karakas A. I., 2017a, in Alsabti A. W., Murdin P., eds, , Handbook of Supernovae. p. 461, doi:10.1007/978-3-319-21846-5_117

Karakas A. I., 2017b, in Alsabti A. W., Murdin P., eds, , Handbook of Supernovae. p. 461, doi:10.1007/978-3-319-21846-5_117

Karakas A. I., Lattanzio J. C., 2014, Publ. Astron. Soc. Australia, 31, e030

Karakas A. I., Lattanzio J. C., Pols O. R., 2002, Publ. Astron. Soc. Australia, 19, 515

Kennicutt R. C. J., 1979, ApJ, 228, 394

Kinson D. A., Oliveira J. M., van Loon J. T., 2021, MNRAS, 507, 5106

Kinson D. A., Oliveira J. M., van Loon J. T., 2022, MNRAS, 517, 140

Kippenhahn R., Weigert A., Weiss A., 2012, Evolution Through Helium Burning: Intermediate-Mass Stars. Springer Berlin Heidelberg, Berlin, Heidelberg, pp 367–384, doi:10.1007/978-3-642-30304-3_31, https://doi.org/10.1007/978-3-642-30304-3_31

Kirby E. N., Cohen J. G., Guhathakurta P., Cheng L., Bullock J. S., Gallazzi A., 2013, ApJ, 779, 102

Knuth K. H., 2006, arXiv e-prints, p. physics/0605197

Komiyama Y., et al., 2003, ApJ, 590, L17

Kraemer K. E., Sloan G. C., Price S. D., Walker H. J., 2002, ApJS, 140, 389

Krause O., Birkmann S. M., Rieke G. H., Lemke D., Klaas U., Hines D. C., Gordon K. D., 2004, Nature, 432, 596

Kučinskas A., Hauschildt P. H., Ludwig H. G., Brott I., Vansevičius V., Lindegren L., Tanabé T., Allard F., 2005, A&A, 442, 281

Kučinskas A., Hauschildt P. H., Brott I., Vansevičius V., Lindegren L., Tanabé T., Allard F., 2006, A&A, 452, 1021

Lagadec E., Zijlstra A. A., Matsuura M., Whitelock P. A., van Loon J. T., 2007, in Kerschbaum F., Charbonnel C., Wing R. F., eds, Astronomical Society of the Pacific Conference Series Vol. 378, Why Galaxies Care About AGB Stars: Their Importance as Actors and Probes. p. 268 (arXiv:astro-ph/0611073), doi:10.48550/arXiv.astro-ph/0611073

Laporte N., et al., 2017, ApJ, 837, L21

Lattanzio J. C., Wood P. R., 2004, in Habing H. J., Olofsson H., eds, , Asymptotic Giant Branch Stars. pp 23–104, doi:10.1007/978-1-4757-3876-6_2

Le Bertre T., 1997, A&A, 324, 1059

Lebreuilly U., Commerçon B., Laibe G., 2020, A&A, 641, A112

Lee H., McCall M. L., Kingsburgh R. L., Ross R., Stevenson C. C., 2003, AJ, 125, 146

Lee H., Skillman E. D., Venn K. A., 2006, ApJ, 642, 813

Lenkić L., et al., 2024, ApJ, 967, 110

Levesque E. M., Massey P., 2012, AJ, 144, 2

Li J., Chen B., Jiang B., Gao J., Chen X., 2024, ApJ, 968, L26

Liljegren S., Höfner S., Eriksson K., Nowotny W., 2017, A&A, 606, A6

Madau P., Dickinson M., 2014, ARA&A, 52, 415

Magrini L., Gonçalves D. R., 2009, MNRAS, 398, 280

Maraston C., 2005, MNRAS, 362, 799

Marigo P., Girardi L., 2007, A&A, 469, 239

Marigo P., Girardi L., Bressan A., 1999, A&A, 344, 123

Marigo P., Girardi L., Bressan A., Groenewegen M. A. T., Silva L., Granato G. L., 2008, A&A, 482, 883

Marigo P., Bressan A., Nanni A., Girardi L., Pumo M. L., 2013, MNRAS, 434, 488

Massey P., 1998, ApJ, 501, 153

Massey P., Olsen K. A. G., 2003, AJ, 126, 2867

Mateo M. L., 1998, ARA&A, 36, 435

Matsuura M., et al., 2009, MNRAS, 396, 918

Matsuura M., et al., 2011, Science, 333, 1258

McConnachie A. W., 2012, AJ, 144, 4

McConnachie A. W., Higgs C. R., Thomas G. F., Venn K. A., Côté P., Battaglia G., Lewis G. F., 2021, MNRAS, 501, 2363

McDonald I., van Loon J. T., Dupree A. K., Boyer M. L., 2010, MNRAS, 405, 1711

McDonald I., et al., 2011, ApJS, 193, 23

McDonald I., White J. R., Zijlstra A. A., Guzman Ramirez L., Szyszka C., van Loon J. T., Lagadec E., Jones O. C., 2012, MNRAS, 427, 2647

McQuinn K. B. W., Boyer M., Skillman E. D., Dolphin A. E., 2019, ApJ, 880, 63

Meixner M., et al., 2006, AJ, 132, 2268

Meixner M., et al., 2013, AJ, 146, 62

Mocák M., Müller E., Weiss A., Kifonidis K., 2009, A&A, 501, 659

Molster F. J., Waters L. B. F. M., Tielens A. G. G. M., 2002, A&A, 382, 222

Nally C., 2023, StarbugII: JWST PSF photometry for crowded fields, Astrophysics Source Code Library, record ascl:2309.012 (ascl:2309.012)

Nally C., et al., 2024, MNRAS, 531, 183

Nayak O., et al., 2024a, ApJ, 963, 94

Nayak O., et al., 2024b, ApJ, 975, 262

O'Dell C. R., Hodge P. W., Kennicutt Robert C. J., 1999, PASP, 111, 1382

Olofsson H., 1996, Ap&SS, 245, 169

Olofsson H., Maercker M., Eriksson K., Gustafsson B., Schöier F., 2010, A&A, 515, A27

Ossenkopf V., Henning T., Mathis J. S., 1992, A&A, 261, 567

Paczyński B., 1970, Acta Astron., 20, 47

Paczyński B., 1971, Acta Astron., 21, 417

Patrick L. R., Evans C. J., Davies B., Kudritzki R. P., Gazak J. Z., Bergemann M., Plez B., Ferguson A. M. N., 2015, ApJ, 803, 14

Peimbert M., Peimbert A., Ruiz M. T., 2000, ApJ, 541, 688

Perrin M. D., Soummer R., Elliott E. M., Lallo M. D., Sivaramakrishnan A., 2012, in Clampin M. C., Fazio G. G., MacEwen H. A., Oschmann Jr. J. M., eds, Society of Photo-Optical Instrumentation Engineers (SPIE) Conference Series Vol. 8442, Space Telescopes and Instrumentation 2012: Optical, Infrared, and Millimeter Wave. p. 84423D, doi:10.1117/12.925230

Perrin M. D., Sivaramakrishnan A., Lajoie C.-P., Elliott E., Pueyo L., Ravindranath S., Albert L., 2014, in Oschmann Jr. J. M., Clampin M., Fazio G. G., MacEwen H. A., eds, Society of Photo-Optical Instrumentation Engineers (SPIE) Conference Series Vol. 9143, Space Telescopes and Instrumentation 2014: Optical, Infrared, and Millimeter Wave. p. 91433X, doi:10.1117/12.2056689

Reimers D., 1975, Memoires of the Societe Royale des Sciences de Liege, 8, 369

Ren T., Jiang B., Ren Y., Yang M., 2022, Universe, 8, 465

Rest A., 2023, JWST/HST Alignment Tool, `https://github.com/arminrest/jhat`

Richardson T., Ginsburg A., Indebetouw R., Robitaille T. P., 2024, ApJ, 961, 188

Riebel D., Srinivasan S., Sargent B., Meixner M., 2012, ApJ, 753, 71

Rieke M. J., Kelly D., Horner S., 2005, in Heaney J. B., Burriesci L. G., eds, Society of Photo-Optical Instrumentation Engineers (SPIE) Conference Series Vol. 5904, Cryogenic Optical Systems and Instruments XI. pp 1–8, doi:10.1117/12.615554

Rieke G. H., et al., 2015, PASP, 127, 584

Rieke M. J., et al., 2023, PASP, 135, 028001

Robitaille T. P., 2017, A&A, 600, A11

Robitaille T. P., Whitney B. A., Indebetouw R., Wood K., 2007, ApJS, 169, 328

Robotham A. S. G., et al., 2011, MNRAS, 416, 2640

Ruiz-Dern L., Babusiaux C., Danielski C., Arenou F., Turon C., Lallement R., 2017, in Reylé C., Di Matteo P., Herpin F., Lagadec E., Lançon A., Meliani Z., Royer F., eds, SF2A-2017: Proceedings of the Annual meeting of the French Society of Astronomy and Astrophysics. p. Di

Salaris M., Cassisi S., 2005, Evolution of Stars and Stellar Populations

Salaris M., Girardi L., 2005, Monthly Notices of the Royal Astronomical Society, 357, 669

Sargent B. A., Srinivasan S., Meixner M., 2011, ApJ, 728, 93

Schneider R., Maiolino R., 2024a, A&ARv, 32, 2

Schneider R., Maiolino R., 2024b, A&ARv, 32, 2

Schneider R., Valiante R., Ventura P., dell'Agli F., Di Criscienzo M., Hirashita H., Kemper F., 2014, MNRAS, 442, 1440

Shan S. S., Zhu H., Tian W. W., Zhang M. F., Zhang H. Y., Wu D., Yang A. Y., 2018, ApJS, 238, 35

Sibbons L. F., Ryan S. G., Cioni M. R. L., Irwin M., Napiwotzki R., 2012, A&A, 540, A135

Sibbons L. F., Ryan S. G., Irwin M., Napiwotzki R., 2015, A&A, 573, A84

Siess L., 2006, A&A, 448, 717

Skillman E. D., Terlevich R., Melnick J., 1989, MNRAS, 240, 563

Skrutskie M. F., et al., 2006, AJ, 131, 1163

Sloan G. C., Kraemer K. E., Matsuura M., Wood P. R., Price S. D., Egan M. P., 2006, ApJ, 645, 1118

Sloan G. C., Kraemer K. E., Wood P. R., Zijlstra A. A., Bernard-Salas J., Devost D., Houck J. R., 2008, ApJ, 686, 1056

Speck A. K., Corman A. B., Wakeman K., Wheeler C. H., Thompson G., 2009, ApJ, 691, 1202

Srinivasan S., et al., 2009, AJ, 137, 4810

Srinivasan S., Sargent B. A., Meixner M., 2011, A&A, 532, A54

Srinivasan S., Boyer M. L., Kemper F., Meixner M., Sargent B. A., Riebel D., 2016, MNRAS, 457, 2814

Stetson P. B., 1987, PASP, 99, 191

Sugerman B. E. K., et al., 2006, Science, 313, 196

Sweigart A. V., Gross P. G., 1978, ApJS, 36, 405

Tamura Y., et al., 2019, ApJ, 874, 27

Tantalo M., et al., 2022, ApJ, 933, 197

Tantalo M., et al., 2025, ApJ, 983, 92

Temim T., Dwek E., Tchernyshyov K., Boyer M. L., Meixner M., Gall C., Roman-Duval J., 2015, ApJ, 799, 158

Teyssier M., Johnston K. V., Kuhlen M., 2012, MNRAS, 426, 1808

Ting Y.-S., Hawkins K., Rix H.-W., 2018, ApJ, 858, L7

Tolstoy E., Irwin M. J., Cole A. A., Pasquini L., Gilmozzi R., Gallagher J. S., 2001, MNRAS, 327, 918

Ueta T., Meixner M., 2003, ApJ, 586, 1338

Vassiliadis E., Wood P. R., 1993, ApJ, 413, 641

Ventura P., D'Antona F., 2005, A&A, 431, 279

Ventura P., et al., 2012, MNRAS, 420, 1442

Wagenhuber J., Groenewegen M. A. T., 1998, A&A, 340, 183

Wallerstein G., Knapp G. R., 1998, ARA&A, 36, 369

Walter F., et al., 2011, ApJ, 726, L11

Waters L. B. F. M., et al., 1996, A&A, 315, L361

Weidemann V., 2000, A&A, 363, 647

Whitelock P., Menzies J., Feast M., Marang F., Carter B., Roberts G., Catchpole R., Chapman J., 1994, MNRAS, 267, 711

Whitelock P. A., Feast M. W., Van Leeuwen F., 2008, MNRAS, 386, 313

Whitelock P. A., Menzies J. W., Feast M. W., Nsengiyumva F., Matsunaga N., 2013, MNRAS, 428, 2216

Whitelock P. A., Menzies J. W., Feast M. W., Nsengiyumva F., Matsunaga N., 2014, VizieR Online Data Catalog: JHKs photometry of AGB stars in NGC 6822 (Whitelock+, 2013), VizieR On-line Data Catalog: J/MNRAS/428/2216. Originally published in: 2013MNRAS.428.2216W

Whitelock P. A., Menzies J. W., Feast M. W., Marigo P., 2018, MNRAS, 473, 173

Wood P. R., Bessell M. S., Fox M. W., 1983, ApJ, 272, 99

Wood P. R., et al., 1999, in Le Bertre T., Lebre A., Waelkens C., eds, IAU Symposium Vol. 191, Asymptotic Giant Branch Stars. p. 151

Worthey G., 1999, in Hubeny I., Heap S., Cornett R., eds, Astronomical Society of the Pacific Conference Series Vol. 192, Spectrophotometric Dating of Stars and Galaxies. p. 283

Wright G. S., et al., 2023, PASP, 135, 048003

Wyder T. K., 2001, AJ, 122, 2490

Xilouris E. M., Georgakakis A. E., Misiriotis A., Charmandaris V., 2004, MNRAS, 355, 57

Zeidler P., Sabbi E., Nota A., Manjavacas E., Jones O. C., Pacifici C., 2024, ApJ, 975, 18

Zhang Z., Wang X., 2010, Journal of Thermophysics and Heat Transfer - J THERMOPHYS HEAT TRANSFER, 24, 222

Zhang S., Mackey D., Da Costa G. S., 2021, MNRAS, 508, 2098

Zhukovska S., Henning T., 2013, A&A, 555, A99

Zijlstra A. A., et al., 2006, MNRAS, 370, 1961

de Blok W. J. G., Walter F., 2000, ApJ, 537, L95

de Blok W. J. G., Walter F., 2003, MNRAS, 341, L39

de Blok W. J. G., Walter F., 2006, AJ, 131, 343

van Loon J. T., Groenewegen M. A. T., de Koter A., Trams N. R., Waters L. B. F. M., Zijlstra A. A., Whitelock P. A., Loup C., 1999, A&A, 351, 559

van Loon J. T., Cioni M. R. L., Zijlstra A. A., Loup C., 2005, A&A, 438, 273

van Loon J. T., Cohen M., Oliveira J. M., Matsuura M., McDonald I., Sloan G. C., Wood P. R., Zijlstra A. A., 2008, A&A, 487, 1055

van Loon J. T., Oliveira J. M., Gordon K. D., Sloan G. C., Engelbracht C. W., 2010, AJ, 139, 1553

A | Starbug2 Typical Run

This chapter will provide a basic overview of the STARBUGII core routines. For a complete guide on all routines, options and use cases, see readthedocs.

A.1 Installation and Setup

```
//Installation
$~ pip install starbug2
$~ starbug2 --init
$~ starbug2 --version
                    *          *  __  *  __    - * --   -
STARBUGII                *      / ___ /    \   --  -      -
---------                  *___---.    .___/  -   --   -
JWST photometry in        ./=== \  \.      \      *
complex crowded fields    | (O)  |  |      |           *
                           \._._/ ./    _(\)   *
conor.nally@ed.ac.uk      /   ~--\ ----~   \      *
                        ---       ---       ---
 starbug2-v0.7.7
```

```
//Basic synopsis
$~ starbug2 -vh
usage: starbug2 [-ABDfhMPv] [-b bgdfile] [-d apfile] [-n ncores]   [
   ↪ -o ouput] [-p file.param] [-s opt=val] image.fits ...
   -A  --apphot          : run aperture photometry on a source list
   -B  --background      : run background estimation
   -D  --detect          : run source detection
   -M  --match           : match outputs from all input image files
   -P  --psf             : run psf photometry

   -b  --bgdfile         : load background (-bgd.fits) file
   -d  --apfile  ap.fits : load a source detection (-ap.fits)
   -f  --find            : attempt to find associated -ap -bgd files
   -h  --help            : display uasage information
   -n  --ncores      num : number of CPU cores to multiprocess
   -o  --output      dir : output directory
   -p  --param   a.param : load parameter file
   -s  --set      option : set value in parameter file at runtime
   -v  --verbose         : display verbose outputs
```

A.2 Individual Routines

Outlined here are the core routines required for a photometric catalogue. Routines generate either a *fits* source list or a *fits* image output. The output from one can act as the input for the next. Alternatively, the entire sequence of routines can be executed in a single instance.

```
//Generate a Parameter file
$~ starbug2 --local-param
starbug.param
```

```
//Source Detection
$~ starbug2 -D image.fits
image-ap.fits
```

```
//Background Estimation (using source list)
$~ starbug2 -d image-ap.fits -B image.fits
image-bgd.fits
```

```
//PSF photometry (using source list and optional background estm.)
$~ starbug2 -d image-ap.fits -b image-bgd.fits -P image.fits
image-psf.fits
```

```
//Aperture photometry on multiple exposures
$~ starbug2 -d image.fits -A exp1.fits exp2.fits exp3.fits
exp1-ap.fits
exp2-ap.fits
exp3-ap.fits
```

```
//PSF photometry on multiple exposures
$~ starbug2 -d image.fits -P exp1.fits exp2.fits exp3.fits
exp1-psf.fits
exp2-psf.fits
exp3-psf.fits
```

```
//Match exposures into single catalogue
$~ starbug2-match exp*-psf.fits
exp(123)-psfmatch.fits
```

```
/*Band match multiple PSF catalogues
 *Output to specific filename (-o)
 *Set explicit Separation Thresholds (-s)
 */
$~ starbug2-match -Bo out.fits -sMATCH_THRESH=0.1,0.2,0.3 filter1.
    ↪ fits filter2.fits filter3.fits
out.fits
```

```
//Artificial Star Test
$~ starbug2-ast -N100 -S100 image.fits
image-ast.fits
```

A.3 A Worked Example

Using the following (optional) directory structure. This example demonstrates the execution of STARBUGII on two NIRCam filters, each with one mosaic and four individual exposures. Source detection will be performed on the mosaics, and PSF photometry will be applied to the exposures. The results are combined into a band-matched catalogue.

```
science/
├──────────────────────────F444W/
└── F115W/                  ├── f444w_mosaic.fits
    ├── f115w_mosaic.fits   ├── f444w_01.fits
    ├── f115w_01.fits       ├── f444w_02.fits
    ├── f115w_02.fits       ├── f444w_03.fits
    ├── f115w_03.fits       └── f444w_04.fits
    └── f115w_04.fits
```

```
//Generate the parameter file inside F115W/
$~ starbug2 --local-param
$~ mv starbug.param f115w.param
f115w.param

/*Detect on F115W mosaic (-D)
 *Load the generated parameter file (-p)
 *Override one parameter for testing (-s)
 */
$~ starbug2 -vD -sSHARP_HI=0.8 -pf115w.param f115w_mosaic.fits
f115w_mosaic-ap.fits

/*Run BGD and PSF routines on exposures (-B -P)
 *Multiprocess over 4 cores (-n 4)
 *Match the outputs into a single catalogue (-M)
 */
$~ starbug2 -vd f115w_mosaic-ap.fits -n4 -pf115w.param -BPM f115w_01.
    ↪ fits f115w_02.fits f115w_03.fits f115w_04.fits
f115w_01-psf.fits
f115w_02-psf.fits
f115w_03-psf.fits
f115w_04-psf.fits
f115w_(1234)-psfmatch.fits

$~ starbug2-ast -N30 -S100 -n3 f115w_mosaic.fits
f115w_mosaic-ast.fits
```

```
//Repeat the process inside F444W/
$~ starbug2 --local-param
$~ starbug2 -D f444w_mosaic.fits
$~ starbug2 -d f444w_mosaic.fits -BPMn4 f444w_0*.fits
```

```
//Band match the catalogues together
$~ starbug2-match --band F115W/f115w_(1234)-psfmatch.fits F444W/
    ↪ f444w_(1234)-psfmatch.fits -o catalogue.fits -sMATCH_THRESH=0.1
```

A.4 Description of Major Parameters

VERBOSE [INT 0:1]
Run STARBUGII in verbose mode.

OUTPUT [STR]
Output file or directory name. If using a specific filename, STARBUGII will append the relevant suffixes to the data products, i.e a detection list will go to *OUTPUT-ap.fits*

HDUNAME [INT/STR]
STARBUGII will look for "SCI" "BGD" "RES" *fits* extension names; if these are not present, it will use the first extension in the file (HDUNAME=0). If STARBUGII is being run on a non-standard *fits* image, set the index or extension name with this parameter.

FILTER [STR]
If the keyword "FILTER" is not present in the *fits* image header file, STARBUGII will use "mag" as the filter name. This may have unintended consequences, for example, in the matching. Set the filter name explicitly with this parameter.

FWHM [FLOAT>0]
If STARBUGII can't find the full-width half maximum of the image, set it explicitly here. This is required for many steps in the detection and photometry routines. When running STARBUGII on standard JWST images, it should be able to automatically set the FWHM, if it doesn't, it will warn you. Set the FWHM in pixel units with this parameter.

SIGSKY [FLOAT>0]
Number of sigma below the image median, which pixels get removed as sky. In images with bright diffuse emissions, decrease this value gradually, in steps of 0.1, and observe the number of detected sources increase. However, be cautious of false detections of bright spots.

SIGSRC [FLOAT>0]
Minimum number of sigma above the median that a source must be to be detected. This is often 5 sigma for a robust search or 3 sigma for faint detections. It is usually not encouraged to go below 3 sigma.

DOBGD2D [INT 0:1]
Do the BGD2D detection step. This increases the execution time, but may find new sources.

DOCONVL [INT 0:1]
Do the CONVL detection step. This increases the execution time, but may find new sources.

CLEANSRC [INT 0:1]

Do source cleaning at the end of the detection routine. This removes sources that lie outwith the geometric quality parameters (defined below), to remove bad detections and background galaxies. Turn this off with '0', but expect the catalogue to contain a lot of extra bad sources.

SHARP_LO [FLOAT]
Set the lower bound for how "sharp" a point source is.

SHARP_HI [FLOAT]
Set the upper bound for how "sharp" a point source is.

ROUND1_HI [FLOAT]
ROUNDNESS1 is a measure of symmetry in the source. It is a symmetric distribution centred on zero. Set the magnitude of the outer limit with this parameter.

ROUND2_HI [FLOAT]
ROUNDNESS2 is a measure of the ratio between a 1D Gaussian fit horizontally and vertically to the source. It is a symmetric distribution centred on zero. Set the magnitude of the outer limit with this parameter.

SMOOTH_LO [FLOAT]
Set the lower bound for how "smooth" a source is. This distribution is unbounded, but clean sources usually shouldn't go below 0.

SMOOTH_HI [FLOAT]
Set the upper bound for how "smooth" a source is. This parameter should be tweaked very slowly, and the results investigated in detail. It is very effective at removing spurious detections in dusty regions but may remove "good" sources in crowded areas.

RICKER_R [FLOAT>0]
Set the radius for the wavelet convolved with the image during the CONVL routine. In MIRI images, this will likely need to be increased to limit spurious detections in the dust structures. Set it high and bring it down slowly to see the effect.

APPHOT_R [FLOAT>0]
Aperture radius in pixel units. If left blank or set <0, STARBUGII will use ENCENERGY to calculate the aperture radius.

ENCENERGY [FLOAT 0-1]
Calculate the aperture radius from the "percentage encircled energy". This requires an aperture correction file (APCORR_FILE) to be either explicitly set, or automatically loaded in the case of JWST images. APPHOT_R takes precedence over this parameter, but if it fails, it will use the value for FWHM.

SKY_RIN [FLOAT>0]
Set the inner radius for the sky annulus for aperture photometry in pixel

units. This should be greater than APPHOT_R; if it is not, STARBUGII will automatically set it to APPHOT_R + 1.

SKY_ROUT [FLOAT>0]
Set the outer radius for the sky annulus for aperture photometry in pixel units. This should be greater than SKY_RIN; if it is not, STARBUGII will automatically set it to SKY_RIN + 1.

APCORR_FILE [STR]
Set the filename for an explicit aperture correction file. This file should contain the columns "radius", " apcorr", and optionally "eefraction". This will be used to calculate the aperture correction for a given aperture radius.

BGD_R [FLOAT>0]
Set a aperture source masking radius in pixel units to be used during the diffuse background estimation routine. By default STARBUGII will try to calculate good values for each source, but in cases where this doesnt act appropriately, a uniform radius can be set with this parameter.

PROF_SCALE [FLOAT>0]
The aperture masking in the background estimation steps scales the aperture radii with source flux. This parameter is used to change the scale factor **A** of the profile.

PROF_SLOPE [FLOAT>0]
The aperture masking in the background estimation steps scales the aperture radii with source flux. This parameter is used to change the slope exponent **B** of the profile.

BGD_CHECKFILE [STR]
The scaled aperture masking is done under the hood of STARBUGII. Set this value to a filename to output a DS9 region file containing the calculated aperture radii for each source.

BOX_SIZE [FLOAT>1]
Set the kernel size in pixel units to be used for estimating the background emission. When set small, the resulting model will contain a lot of detail at a high resolution but may be influenced by extraneous bright pixels or undetected sources. When set to a large size, the resulting model will have a lower resolution but will be less influenced by bright pixels.

AP_FILE [STR]
Set the filename for a source list to be explicitly used during any STARBUGII runs. The file must contain columns xcentroid,ycentroid or RA,DEC and the image must contain WCS information to convert that to pixel coordinates.

BGD_FILE [STR]
Set the filename for a background estimation file to be loaded into any STARBUGII runs. This must be a *fits* image with the exact dimensions as the image being

actively worked on.

PSF_FILE [STR]
Set the filename for a psf file to be loaded into any STARBUGII runs. This must be a *fits* image.

USE_WCS [INT 0:1]
If a loaded AP_FILE contains both RADEC and xycentroid columns, do you want STARBUGII to use the RADEC columns true (1) or false (0).

ZP_MAG [FLOAT]
Set a zeropoint to be added to the magnitudes. By default, it is 8.9 for AB magnitudes.

CRIT_SEP [FLOAT>0]
Separation threshold (pixels) between sources to be grouped together in PSF fitting. If this number is too low, the constructed groups may be very large, increasing execution time for PSF fitting.

FORCE_POS [INT 0:1]
Set whether you want the conduct "forced centre" PSF photometry.

MAX_XYDEV [FLOAT>0]
Set the maximum deviation of the central position of a source from its initial guess during PSF photometry. Sources that deviate by more than this value will be refit with forced centres. This value, by default, is in units of pixels, but can be set in other units by appending (p:pixels, s:arcseconds, m:arcminutes, d:degrees) to the end of the value.

PSF_SIZE [INT>0]
Explicitly set the size of the PSF to be used in pixel units. If not set, STARBUGII will use the whole PSF image.

GEN_RESIDUAL [INT 0:1]
Generate a residual image at the end of PSF photometry. This will have the estimated background and the fitted sources subtracted.

MATCH_THRESH [FLOAT>0]
Separation threshold between sources in separate catalogue during matching. Sources closer than this will be matched to a single source.

NEXP_THRESH [INT>0]
Minimum number of individual entries for a source in the final matched catalogue. Sources with NUM<NEXP_THRESH will be removed from the final compiled catalogue.

NTESTS [INT>0]
Number of separate tests to run during artificial star testing.

NSTARS [INT>0]

Number of stars to inject during one test during artificial star testing.

MAX_MAG [FLOAT]
Bright magnitude limit of an injected artificial star.

MIN_MAG [FLOAT]
Faint magnitude limit of an injected artificial star.

PLOTAST [STR]
Plot the results of the artificial star test to this file name.

B | JWST GTO:1234 Observation Properties

Table B.1 Observing Parameters for the NIRCam Prime and Parallel Imaging.

Filter	Field	Readout Pattern	Groups /Int.	Int. /Exp.	Dithers	Total Exp. Time [sec]
F115W	NIRCam Prime	BRIGHT2	7	1	12	1803.777
F200W	NIRCam Prime	BRIGHT2	7	1	12	1803.777
F356W	NIRCam Prime	BRIGHT2	7	1	12	1803.777
F444W	NIRCam Prime	BRIGHT2	7	1	12	1803.777
F140M	NIRCam Parallel	SHALLOW4	8	1	4	1674.936
F335M	NIRCam Parallel	SHALLOW4	8	1	4	1674.936
F115W	NIRCam Parallel	SHALLOW2	3	1	4	515.365
F150W	NIRCam Parallel	SHALLOW2	4	1	4	730.100
F200W	NIRCam Parallel	SHALLOW4	4	1	4	815.995
F277W	NIRCam Parallel	SHALLOW2	4	1	4	730.100
F356W	NIRCam Parallel	SHALLOW2	3	1	4	515.365
F444W	NIRCam Parallel	SHALLOW4	4	1	4	815.995

Table B.2 Observing Parameters for the MIRI Prime and Parallel Imaging.

Filter	Field	Readout Pattern	Groups /Int.	Int. /Exp.	Dithers	Total Exp. Time [sec]
F770W	MIRI Prime	FASTR1	52	1	4	577.208
F1000W	MIRI Prime	FASTR1	36	2	4	810.312
F1500W	MIRI Prime	FASTR1	15	8	4	1409.72
F2100W	MIRI Prime	FASTR1	20	9	4	2086.83
F1000W	MIRI Parallel	SLOWR1	5	1	12	1433.395
F1500W	MIRI Parallel	SLOWR1	5	1	12	1433.395